



UPPSALA  
UNIVERSITET

*Digital Comprehensive Summaries of Uppsala Dissertations  
from the Faculty of Science and Technology 338*

# Electronic Structure and Lattice Dynamics of Elements and Compounds

PETROS SOUVATZIS



ACTA  
UNIVERSITATIS  
UPSALIENSIS  
UPPSALA  
2007

ISSN 1651-6214  
ISBN 978-91-554-6960-3  
urn:nbn:se:uu:diva-8198

Dissertation presented at Uppsala University to be publicly examined in Siegbahnsalen, Ångströmlaboratoriet, Lägerhyddsvägen 1, Box 530, Uppsala University, SE-75121, Uppsala, Friday, October 5, 2007 at 10:15 for the degree of Doctor of Philosophy. The examination will be conducted in English.

### **Abstract**

Souvatzis, P. 2007. Electronic Structure and Lattice Dynamics of Elements and Compounds. Acta Universitatis Upsaliensis. *Digital Comprehensive Summaries of Uppsala Dissertations from the Faculty of Science and Technology* 338. 127 pp. Uppsala. ISBN 978-91-554-6960-3.

The elastic constants of  $Mg_{(1-x)}Al_xB_2$  have been calculated in the regime  $0 < x < 0.25$ . The calculations show that the ratio,  $B/G$ , between the bulk- and the shear-modulus stays well below the empirical ductility limit, 1.75, for all concentrations, indicating that the introduction of Al will not change the brittle behaviour of the material considerably. Furthermore, the tetragonal elastic constant  $C'$  has been calculated for the transition metal alloys Fe-Co, Mo-Tc and W-Re, showing that if a suitable tuning of the alloying is made, these materials have a vanishingly low  $C'$ . Thermal expansion calculations of the 4d transition metals have also been performed, showing good agreement with experiment with the exception of Nb and Mo. The calculated phonon dispersions of the 4d metals all give reasonable agreement with experiment. First principles calculations of the thermal expansion of hcp Ti have been performed, showing that this element has a negative thermal expansion along the c-axis which is linked to the closeness of the Fermi level to an electronic topological transition. Calculations of the EOS of fcc Au give support to the suggestion that the ruby pressure scale might underestimate pressures with  $\sim 10$  GPa at pressures  $\sim 150$  GPa. The high temperature bcc phase of the group IV metals has been calculated with the novel self-consistent ab-initio dynamical (SCAILD) method. The results show good agreement with experiment, and the free energy resolution of  $< 1$  meV suggests that this method might be suitable for calculating free energy differences between different crystallographic phases as a function of temperature.

*Keywords:* electronic structure, lattice dynamics, first-principles theory, self-consistent lattice dynamical calculation, elasticity, super plasticity, electronic topological transition, equation of state

*Petros Souvatzis, Department of Physics, Box 530, Uppsala University, SE-75121 Uppsala, Sweden*

© Petros Souvatzis 2007

ISSN 1651-6214

ISBN 978-91-554-6960-3

urn:nbn:se:uu:diva-8198 (<http://urn.kb.se/resolve?urn=urn:nbn:se:uu:diva-8198>)

*To Lina.*



# List of Papers

This thesis is based on the following papers, which are referred to in the text by their Roman numerals.

- I        **Elastic properties of  $\text{Mg}_{(1-x)}\text{Al}_x\text{B}_2$  from first principles theory.** P. Souvatzis, J. M. Osorio-Guillén, R. Ahuja, A. Grechnev, O. Eriksson, *J.Phys.:Condens. Matter*, **16**, 5241 (2004)
- II       **First-principles prediction of superplastic transition-metal alloys.** P. Souvatzis, M. I. Katsnelson, S. Simak, R. Ahuja, O. Eriksson, P. Mohn, *Phys. Rev. B*, **70**, 012201 (2004)
- III      **Calculation of the equation of state of fcc Au from first principles.** P. Souvatzis, A. Delin, O. Eriksson, *Phys. Rev. B*, **73**, 054110 (2006)
- IV      **Anomalous thermal expansion in  $\alpha$ -titanium.** P. Souvatzis, O. Eriksson, M. I. Katsnelson, *Phys. Rev. Lett.* **99**, 015901 (2007)
- V        **Entropy driven stabilization of energetically unstable crystal structures explained from first principles theory.** P. Souvatzis, O. Eriksson, M. I. Katsnelson, S. P. Rudin, *Submitted to Phys. Rev. Lett.*
- VI      **Ab-initio calculations of the phonon spectrum and the thermal expansion for the 4d metals.** P. Souvatzis, O. Eriksson, *Submitted to Phys. Rev. B*

Reprints were made with permission from the publishers.



# Contents

1	Svensk introduktion	9
2	Introduction	13
3	Density functional theory	17
3.1	The many body problem	17
3.2	The Hohenberg-Kohn theorems	18
3.3	Correlation	20
3.4	The Kohn-Sham equations	22
3.5	The adiabatic connection	24
3.6	The local density approximation	26
4	Methods for calculating band structure	29
4.1	The KKR-ASA method	29
4.1.1	Canonical band theory	32
4.2	The LMTO method	33
4.2.1	The linear muffin tin orbitals	36
4.2.2	The secular equation	38
4.2.3	The FP-LMTO treatment	39
4.3	The LMTO-ASA method	40
4.4	The pseudo potential method	42
4.5	Projector augmented wave method	45
4.6	The self-consistent loop	46
5	Chemical bonding	49
5.0.1	The balanced crystal overlap occupation population (BCOOP)	49
5.0.2	Interpretation of the BCOOP from the LCAO perspective	50
5.0.3	Chemical bonding in $\text{MgB}_2$	53
6	Theory of elasticity	59
6.1	The strain tensor	59
6.2	The elastic constants	61
6.3	Calculations of elastic constants	62
6.3.1	The strain matrices of a hexagonal lattice	63
6.3.2	The strain matrices of a cubic lattice	64
6.4	The elastic properties of $\text{Mg}_{(1-x)}\text{Al}_x\text{B}_2$	65
7	Predictions of superplastic transition metal alloys	69
7.1	Structural stability in connection with lattice and bond topology	69
7.1.1	Theory of moments	69

7.1.2	An example: Structural stability of transition metals with a half full d-band . . . . .	71
7.2	Structural trends of transition metals . . . . .	73
7.3	Super plasticity . . . . .	76
7.3.1	Results . . . . .	77
8	Lattice dynamics . . . . .	79
8.1	The Born Oppenheimer approximation . . . . .	79
8.2	The harmonic lattice . . . . .	80
8.3	The supercell method . . . . .	82
8.4	Some thermodynamics and the quasi harmonic approximation . . . . .	84
8.5	The equation of state and the Hugoniot of fcc Au . . . . .	86
8.6	Thermal expansion . . . . .	90
8.6.1	Thermal expansion of cubic metals . . . . .	90
8.6.2	Thermal expansion of hexagonal metals . . . . .	92
8.7	Electronic topological transitions and thermal contraction . . . . .	95
8.8	The self-consistent ab initio lattice dynamical method . . . . .	101
8.8.1	The anharmonic lattice . . . . .	101
8.8.2	The self-consistent cycle . . . . .	103
8.8.3	Results . . . . .	105
9	Summary and outlook . . . . .	111
	Acknowledgments . . . . .	113
	Appendices . . . . .	114
A	Fermi surfaces of hcp Zr . . . . .	115
B	The mean field Hamiltonian . . . . .	117
C	Embedded atom potentials . . . . .	119
	Bibliography . . . . .	123

# 1. Svensk introduktion

Runt ca 460 fkr. föddes den Grekiske filosofen Demokritos vilken var den man som gav världen idén om materiens minsta gemensamma nämnare, mera kända så som atomer. Emellertid var det inte Demokritos som var först med idén om ett atomistiskt perspektiv utan hans lärare Leukippos. Dock var det Demokritos som utvecklade idén och såg till att den inte föll i glömska under århundradena. Det tog mer än 2000 år innan den atomistiska teorin motbevisades av experiment. Genom upptäckten av den negativ laddade elektronen och den positivt laddade protonen var man tvungen att överge idén om atomens odelbarhet. Nästan samtida med upptäckterna av elektronen och protonen utvecklades kvantmekaniken, och tack vare den numera ökanda Schrödingerekvationen kunde kvantitativa förutsägelser göras för hur dessa partiklar betedde sig.

En av denna avhandlings minsta gemensamma nämnare är Schrödingerekvationen

$$\mathcal{H}\Psi(\mathbf{r}_1, \mathbf{r}_2, \dots, \mathbf{r}_n) = E\Psi(\mathbf{r}_1, \mathbf{r}_2, \dots, \mathbf{r}_n). \quad (1.1)$$

Denna ekvation är definierad av den så kallade Hamiltonianen  $\mathcal{H}$  vilken i sin tur är definierad av systemets olika typer av atomer och deras relativa positioner. Här svarar  $\mathbf{r}_i$ ,  $i = 1, \dots, n$  mot rumskoordinaterna för elektronerna i systemet. Lösningen till Schrödingerekvationen ges av vågfunktionen  $\Psi$  och systemets total energi  $E$ . På grund av elektronernas inbördes växelverkan kan Schrödingerekvationen tyvärr inte lösas exakt, och effekten av denna växelverkan måste behandlas approximativt. I varenda artikel som har skrivits i anslutning till denna avhandling har Schrödingerekvationen lösts approximativt, och det är genom dessa lösningar som förutsägelseerna om olika materialegenskaper har gjorts.

I den första delen av avhandlingen (**kapitel 3,4**) redovisas de metoder och approximationer som används för att lösa denna ekvation. För den läsare som inte är insatt i kvantmekanik kommer följande 3 meningar att sammanfatta vad som har gjorts. Under antagandet att atomkärnorna, dvs protonerna och neutronerna, "upplevs" så som stillastående av elektronerna så ger lösningarna till Schrödingerekvationen den elektron fördelning runt atomkärnorna som minimerar systemets totala energi. Från den beräknade laddningsfördelningen kan systemets totalenergi beräknas, och genom att ändra atomkärnornas positioner i förhållande till varandra är det möjligt att beräkna hur den totala energin beror av atomernas positioner. Det är genom detta beroende som elastiska så väl som vibrationella egenskaper har beräknats.

Ett av målen med denna avhandling har varit att förstå hur elektronstrukturen och mekaniska egenskaper hos material hänger samman. Detta har gjorts med syfte att hitta möjliga tillvägagångssätt att manipulera material till att ha önskvärda mekaniska egenskaper, vilka kan användas både inom industri och vetenskap. Det första materialet som har studerats i denna avhandling i anslutning till detta mål är  $\text{MgB}_2$  (**Kapitel 5,6**). Det upptäcktes nyligen av Nagamatsu [1] att detta material var supraledande, vilket har föranlett stor uppmärksamhet både inom den vetenskapliga så väl som den kommersiella världen. Fram till dags dato så har det praktiska användandet av  $\text{MgB}_2$  begränsats av materialets sprödhet. Man har funnit både från teori [2] och experiment [3, 4] att  $\text{MgB}_2$  är elastiskt anisotropt, med en kvot på  $\sim 1.8$  mellan bulkmodulen i planet  $B_a$  och bulkmodulen ortogonalt mot planet  $B_c$ . Eftersom det har visats, åtminstone empiriskt, att den elastiska anisotropin hos ett material är korrelerat med materialets sprödhet så har arbetet med  $\text{MgB}_2$  i denna avhandling varit riktat mot att minska denna anisotropi. Om man lyckas med att göra  $\text{MgB}_2$  mindre sprött kommer användandet av supraledande teknik att spridas till ett större område av tillämpningar. Detta beror naturligtvis på den låga tillverkningskostnaden hos  $\text{MgB}_2$  jämfört med andra supraledande material så som  $\text{YBa}_2\text{Cu}_3\text{O}_7$ .

Den tredje delen av denna avhandling (**kapitel 7**) inspirerades av den experimentella upptäckten av de superplastiska legeringarna Ti-Ta-Nb-V-Zr-O och Ti-Nb-Ta-Zr-O gjorda av Saito [5]. Dessa legeringar är superplastiska i den mening att de har en försvinnande liten tetragonal elastisk konstant  $C'$ . Med utgångspunkt av dessa upptäckter och med hjälp av kanonisk bandteori så har första princip förutsägelser av möjliga superplastiska legeringar hos 3d, 4d och 5d metallerna gjorts.

I den fjärde och sista delen av denna avhandling (**Kapitel 8**) diskuteras de mest intressanta resultaten av min forskning. I detta kapitel redovisas tillsammans med vanliga gitter dynamiska beräkningar den nya *själv konsistenta från första princip gitter dynamiska* (SKFPGD) metoden. Denna metod tar hänsyn till fonon-fonon växelverkan upp till oändlig ordning genom att kombinera beräkningar av interatomära krafter från första princip med en medelfälts formulering av det gitter dynamiska problemet liknande Hartree-Fock approximationen. SKFPGD metoden har använts till att beräkna fonon dispersionerna för högtemperatur bcc fasen hos grupp IV metallerna Ti, Zr och Hf. Resultaten av dessa beräkningar stämmer bra överens med experimentella data, vilket bekräftar Zeners [6] antagande om att bcc fasen hos grupp IV metallerna stabiliseras av entropin. Vidare visar upplösningen hos den fria energin på  $\lesssim 1$  meV hos dessa beräkningar att SKFPGD metoden kan användas, åtminstone i princip, till att beräkna skillnaden i fri energi mellan olika kristallografiska faser som funktion av temperatur.

Syftet med denna avhandling har, förutom att ge en rapport över vad jag har gjort under de senaste åren, varit att i viss utsträckning ge en pedagogisk sammanfattning av teorin bakom de metoder som har använts. Det är därför

min oppriktiga förhoppning att denna avhandling ska kunna förse den aningen  
oerfarne läsaren med lite användbara insikter.



## 2. Introduction

Approximately 460 BC the Greek philosopher Democritus was born, and through his mission the idea that there should exist a set of smallest common material denominators, more commonly known as atoms, was spread out in the world. However, the atomistic perspective was not first introduced by Democritus, instead it was actually his teacher Leukippos who was the first to formulate the idea. Nevertheless Democritus developed the original idea of his teacher and saw to it that it was not forgotten throughout the centuries. It took more than 2000 years for the indivisible atomistic theory to be discarded by experiments. Through the detection of the negatively charged electron and positively charged proton the idea that the atom could not be disassembled into even smaller parts had to be abandoned. Almost synchronously with the discovery of the electron and proton, quantum mechanics was developed and through the infamous Schrödinger equation it was suddenly possible to make quantitative predictions on the behaviour of these newly discovered particles.

One of the smallest common theoretical denominators of this thesis is the Schrödinger equation.

$$\mathcal{H}\Psi(\mathbf{r}_1, \mathbf{r}_2, \dots, \mathbf{r}_n) = E\Psi(\mathbf{r}_1, \mathbf{r}_2, \dots, \mathbf{r}_n). \quad (2.1)$$

This equation is defined through the so called Hamiltonian  $\mathcal{H}$  which in turn is defined by the different atom types of the system and the relative atomic positions. Here  $\mathbf{r}_i$ ,  $i = 1, \dots, n$  denotes the spatial coordinates of the electrons of the system. The solution of the Schrödinger equation is given by the wave function  $\Psi$  and the total energy  $E$  of the system. Due to the interaction of the electrons with each other the Schrödinger equation can unfortunately not be solved exactly, and the effect of this interaction has to be treated approximately. In each and every paper referred to in this thesis, the Schrödinger equation has been solved using different types of approximations, and it is through these solutions that all the predictions of material properties have been made.

In the first part (**chapter 3,4**) the methods and approximations used to solve the Schrödinger equation are presented in some detail. For the reader that is unexperienced in quantum mechanics the following 3 sentences provide the shorter version of what has been done. Under the assumption that the atomic nuclei, i.e protons and neutrons, can from the perspective of the electrons be regarded as fixed, the solutions of the Schrödinger equation tell us how the electrons are distributed around the atoms in order to minimize the total energy of the system. From the calculated charge distribution the total energy of the

system can be calculated, and by changing the relative positions of the atomic nuclei the dependence of the total energy upon geometry can be obtained. It is by this dependence the elastic- and vibrational- properties presented in this thesis have been calculated.

One of the objectives for the research that is being presented in this thesis, has been to understand how electronic structure and mechanical properties of materials are connected. This has been done in order to find possible ways to manipulate materials into having desirable mechanical properties, applicable both in industry and in pure science. The first of the materials that has been studied in this thesis, in connection with this objective, is  $\text{MgB}_2$  (**chapter 5,6**). This material was recently discovered by Nagamatsu et al [1] to be superconducting, and it has attracted huge attention both from the scientific and commercial community. Up to this date the practical use of  $\text{MgB}_2$  has been limited by the brittle behavior of the material. It has been found both in theory [2] and experiment [3, 4] that  $\text{MgB}_2$  is an elastically anisotropic material with a ratio between the inplane  $B_a$  and out of plane  $B_c$  bulkmoduli of  $\sim 1.8$ . Since the elastic anisotropy has been shown, at least on empirical grounds, to correlate with the brittleness of a material, the focus on  $\text{MgB}_2$  in this thesis has been aimed at finding ways to suppress this anisotropy. If one is successful in finding a remedy to the brittle behavior of  $\text{MgB}_2$ , the use of superconducting technology will be possible in a much wider range of applications than it is today. This of course, is due to the low manufacturing cost of  $\text{MgB}_2$  compared to conventional superconductors such as  $\text{YBa}_2\text{Cu}_3\text{O}_7$ .

The third part of this thesis (**chapter 7**) was inspired by the experimental finding of the superplastic alloys Ti-Ta-Nb-V-Zr-O and Ti-Nb-Ta-Zr-O by Saito et al [5]. These alloys are superplastic in the sense that they have nearly a vanishing tetragonal elastic constant  $C'$ . On the basis of these findings and of canonical band theory, *ab initio* predictions have been made of possible superplastic alloys amongst the 3d,4d and 5d transition metals.

In the fourth and final part of the thesis (**chapter 8**) the most interesting results of my research are presented. Here newly developed *self-consistent ab initio lattice dynamical* (SCAILD) method is presented together with standard lattice dynamical calculations. This is a method that takes into account phonon-phonon interaction up to infinite order by combining first principles calculations of inter atomic forces with a mean field formulation of the lattice dynamical problem similar to the Hartree-Fock approximation. Here the SCAILD method is used to calculate the phonon dispersions of the high temperature bcc phase of the group IV metals Ti, Zr and Hf. The results of these calculations show good agreement with experiment, confirming Zener's [6] old assumption that it is entropy that stabilizes the bcc phase of the IV group metals at elevated temperatures. Furthermore the resolution of the free energy of the calculations  $\lesssim 1$  meV shows that the SCAILD method could, at least in principle, be used to calculate free energy differences between different crystallographic phases.

The purpose of this thesis, apart from making an official record of what I have been doing during the past years, is to offer a pedagogical review of the theory behind the methods that have been used. Therefore I sincerely hope that this thesis will provide the somewhat unexperienced reader with some useful insight.



### 3. Density functional theory

The task of determining the electronic structure of a material is equivalent to finding the solution to the Schrödinger equation.

$$H\psi(\mathbf{r}_1, \mathbf{r}_2, \dots, \mathbf{r}_N) = E\psi(\mathbf{r}_1, \mathbf{r}_2, \dots, \mathbf{r}_N). \quad (3.1)$$

In other words, a partial differential equation of  $N$  interacting particles (electrons) has to be solved, where generally  $N \sim 10^{23}$ . This certainly is a formidable task and it is for this sole purpose that density functional theory (DFT) has been developed. The corner stone of DFT is that the ground state total energy of a many electron system can be expressed as a functional solely on the electron density. But before the main ideas of the theory are presented, some preliminary topics will be reviewed in order to make it possible for the reader to fully appreciate the beauty of the theory. The material in the following chapter is mainly taken from the books of Parr [7] and Martin [8].

#### 3.1 The many body problem

Let us start with taking a closer look at the Hamiltonian appearing in equation (3.1). In the Born Oppenheimer approximation this Hamiltonian has the following form (in atomic units)

$$H = -\frac{1}{2} \sum_{i=1}^N \nabla_i^2 + \frac{1}{2} \sum_{i=1}^N \sum_{j=1, j \neq i}^N V_{ee}(\mathbf{r}_{ij}) + \sum_{i=1}^N V_{el}(\mathbf{r}_i) \quad (3.2)$$

where  $V_{ee}$  and  $V_{el}$  denote the electron-electron and electron-ion interaction terms respectively, given by

$$V_{ee}(\mathbf{r}_{ij}) = \frac{1}{|\mathbf{r}_i - \mathbf{r}_j|} \quad (3.3)$$

$$V_{el}(\mathbf{r}_i) = - \sum_{m=1}^M \frac{Z_m}{|\mathbf{r}_i - \mathbf{R}_m|} \quad (3.4)$$

In order to clarify the road towards a DFT-formulation, it is convenient to calculate the energy estimate of an arbitrary many body wave function  $\psi(\mathbf{r}_1, \mathbf{r}_2, \dots, \mathbf{r}_N)$

$$\begin{aligned}
E &= \langle \psi | H | \psi \rangle = \\
&\quad -\frac{1}{2} \sum_{i=1}^N \int \psi^*(\mathbf{r}_1, \mathbf{r}_2, \dots, \mathbf{r}_N) \nabla_i^2 \psi(\mathbf{r}_1, \mathbf{r}_2, \dots, \mathbf{r}_N) d\mathbf{r}_1 d\mathbf{r}_2 \cdots d\mathbf{r}_N + \\
&+ \frac{1}{2} \sum_{i=1}^N \sum_{j=1, j \neq i}^N \int \psi^*(\mathbf{r}_1, \mathbf{r}_2, \dots, \mathbf{r}_N) \frac{1}{|\mathbf{r}_i - \mathbf{r}_j|} \psi(\mathbf{r}_1, \mathbf{r}_2, \dots, \mathbf{r}_N) d\mathbf{r}_1 d\mathbf{r}_2 \cdots d\mathbf{r}_N + \\
&\quad + \sum_{i=1}^N \int \psi^*(\mathbf{r}_1, \mathbf{r}_2, \dots, \mathbf{r}_N) V_{eI}(\mathbf{r}_i) \psi(\mathbf{r}_1, \mathbf{r}_2, \dots, \mathbf{r}_N) d\mathbf{r}_1 d\mathbf{r}_2 \cdots d\mathbf{r}_N. \quad (3.5)
\end{aligned}$$

Since all the N-electrons are indistinguishable from each other, all the kinetic energy integrals are equal, all electron-electron interaction integrals are equal and all the electron-ion integrals are equal. Hence the expression in (3.5) can be written as

$$\begin{aligned}
E[\rho(\mathbf{r}), \rho_2(\mathbf{r}, \mathbf{r}')] &= \\
&\quad -\frac{1}{2} \int [\nabla^2 \rho_2(\mathbf{r}, \mathbf{r}')]_{\mathbf{r}=\mathbf{r}'} d\mathbf{r} + \frac{1}{2} \int \frac{\rho_2(\mathbf{r}, \mathbf{r}')}{|\mathbf{r} - \mathbf{r}'|} d\mathbf{r} d\mathbf{r}' + \int \rho(\mathbf{r}) V_{eI}(\mathbf{r}) d\mathbf{r} \quad (3.6)
\end{aligned}$$

where  $\rho_2(\mathbf{r}, \mathbf{r}')$  and  $\rho(\mathbf{r})$  are the two particle density matrix and density, respectively given by

$$\begin{aligned}
\rho(\mathbf{r}) &= \binom{N}{1} \int \psi^*(\mathbf{r}, \mathbf{r}_2, \mathbf{r}_3, \dots, \mathbf{r}_N) \psi(\mathbf{r}, \mathbf{r}_2, \mathbf{r}_3, \dots, \mathbf{r}_N) d\mathbf{r}_2 d\mathbf{r}_3 \cdots d\mathbf{r}_N \\
\rho_2(\mathbf{r}, \mathbf{r}') &= \binom{N}{2} \int \psi^*(\mathbf{r}, \mathbf{r}', \mathbf{r}_3, \mathbf{r}_4, \dots, \mathbf{r}_N) \psi(\mathbf{r}, \mathbf{r}', \mathbf{r}_3, \mathbf{r}_4, \dots, \mathbf{r}_N) d\mathbf{r}_3 d\mathbf{r}_4 \cdots d\mathbf{r}_N
\end{aligned} \quad (3.7)$$

It is now obvious that the functional in eq (3.6) is not only a functional of the density, but also a functional of  $\rho_2$ . If an energy functional depending solely on the density is to be found, then a one-one correspondence between the electron density  $\rho$  and the two particle density matrix  $\rho_2$  must be established. In the next section of this chapter it will be shown that such a correspondence exists.

## 3.2 The Hohenberg-Kohn theorems

**Theorem 1** *For any system of interacting particles in an external potential  $V_{eI}$ , the potential  $V_{eI}$  is determined uniquely, except for a constant, by the ground state density  $\rho_0$ .*

**Theorem 2** *For any external potential  $V_{eI}$  a functional for the energy  $E[\rho]$  in terms of the density  $\rho(\mathbf{r})$  can be defined. Where  $E[\rho]$  is such that the global minimum of  $E[\rho]$  equals the ground state energy of the system, and the density at this minimum equals the ground state density  $\rho_0$  of the system.*

These two theorems were first proven by Hohenberg and Kohn [9] in 1964, and they together with Slater are the parents of all modern DFT calculations. Here follows the proofs of these two important theorems.

**Proof 1** *This proof is based on a reductio absurdum. Let us assume that there exists a ground state density  $\rho_0$  corresponding to two different potentials  $V_{el}^{(1)}(\mathbf{r})$  and  $V_{el}^{(2)}(\mathbf{r})$ , such that  $V_{el}^{(1)}(\mathbf{r}) - V_{el}^{(2)}(\mathbf{r}) \neq \text{Constant}$ . Then if  $H[V_{el}^{(1)}]$  and  $H[V_{el}^{(2)}]$  are the Hamiltonians corresponding to the two external potentials, with respective eigen functions  $\psi^{(1)}$  and  $\psi^{(2)}$ , it is obvious that*

$$\begin{aligned} \rho_0(\mathbf{r}) &= N \int \psi^{(1)}(\mathbf{r}, \mathbf{r}_2, \mathbf{r}_3, \dots, \mathbf{r}_N)^* \psi^{(1)}(\mathbf{r}, \mathbf{r}_2, \mathbf{r}_3, \dots, \mathbf{r}_N) d\mathbf{r}_2 d\mathbf{r}_3 \cdots d\mathbf{r}_N = \\ &N \int \psi^{(2)}(\mathbf{r}, \mathbf{r}_2, \mathbf{r}_3, \dots, \mathbf{r}_N)^* \psi^{(2)}(\mathbf{r}, \mathbf{r}_2, \mathbf{r}_3, \dots, \mathbf{r}_N) d\mathbf{r}_2 d\mathbf{r}_3 \cdots d\mathbf{r}_N \end{aligned} \quad (3.8)$$

and that

$$\begin{aligned} E^{(1)} &= \langle \psi^{(1)} | H[V_{el}^{(1)}] | \psi^{(1)} \rangle < \langle \psi^{(2)} | H[V_{el}^{(1)}] | \psi^{(2)} \rangle = \\ &\langle \psi^{(2)} | H[V_{el}^{(2)}] | \psi^{(2)} \rangle + \langle \psi^{(2)} | H[V_{el}^{(1)}] - H[V_{el}^{(2)}] | \psi^{(2)} \rangle = \\ &E^{(2)} + \sum_{i=1}^N \langle \psi^{(2)} | V_{el}^{(1)}(\mathbf{r}_i) - V_{el}^{(2)}(\mathbf{r}_i) | \psi^{(2)} \rangle = \\ &E^{(2)} + \int [V_{el}^{(1)}(\mathbf{r}) - V_{el}^{(2)}(\mathbf{r})] \rho_0(\mathbf{r}) d\mathbf{r} \end{aligned} \quad (3.9)$$

Now if one instead starts with the Hamiltonian  $H[V_{el}^{(2)}]$  in the above derivation the following relation is obtained

$$E^{(2)} < E^{(1)} + \int [V_{el}^{(2)}(\mathbf{r}) - V_{el}^{(1)}(\mathbf{r})] \rho_0(\mathbf{r}) d\mathbf{r} \quad (3.10)$$

Finally adding equation (3.9) with (3.10) the obviously contradictive statement is found

$$E^{(1)} + E^{(2)} < E^{(1)} + E^{(2)} \quad \square$$

Before the second proof is dealt with, it is important to notice that the first theorem only deals with densities that correspond to external potentials. Since there might exist pathological densities that do not correspond to any external potential, it is important to limit the density space to only those densities that can be represented by an external potential. Thus if  $\mathcal{M} : \mathcal{V} \mapsto \rho$  is the mapping described in theorem 1, the one to one correspondence between the space of V-representable densities and the space of potentials can be stated as

**Theorem 3** *Let  $\mathcal{V}$  be the space of external potentials, and  $\rho$  the space of V-representable densities. Then the mapping  $\mathcal{M} : \mathcal{V} \mapsto \rho$  is bijective, i.e the inverse mapping  $\mathcal{M}^{-1} : \rho \mapsto \mathcal{V}$  exists.*

The proof of the above theorem follows directly from theorem 1. Now the time has come to embark on the proof of theorem 2.

**Proof 2** Let  $\Psi$  be the space of solutions to the Schrödinger equations (3.1) corresponding to the different potentials  $V \in \mathcal{V}$ . Let  $\mathcal{H} : \mathcal{V} \mapsto \Psi$  be the mapping that maps a particular external potential to the ground state solution of the corresponding Schrödinger equation. Then the composite mapping

$$\mathcal{M}^{-1} \circ \mathcal{H} : \rho \mapsto \Psi \quad (3.11)$$

is by theorem 3 clearly bijective with inverse

$$\begin{aligned} \rho(\mathbf{r}) &= [\mathcal{M}^{-1} \circ \mathcal{H}]^{-1}[\psi] = \\ N \int \psi^*(\mathbf{r}, \mathbf{r}_2, \mathbf{r}_3, \dots, \mathbf{r}_N) \psi(\mathbf{r}, \mathbf{r}_2, \mathbf{r}_3, \dots, \mathbf{r}_N) d\mathbf{r}_2 d\mathbf{r}_3 \cdots d\mathbf{r}_N \end{aligned} \quad (3.12)$$

Then from the above discussion it is obvious that the functional in (3.6) easily can be transformed to the following functional of the density

$$E_{HK}[\rho] = F_{HK}[\rho] + \int \rho(\mathbf{r}) V_{el}(\mathbf{r}) d\mathbf{r} \quad (3.13)$$

where

$$F_{HK}[\rho] \equiv \min_{\psi \rightarrow \rho} \left[ -\frac{1}{2} \int [\nabla^2 \rho_2(\mathbf{r}, \mathbf{r}')]_{\mathbf{r}=\mathbf{r}'} d\mathbf{r} + \frac{1}{2} \int \frac{\rho_2(\mathbf{r}, \mathbf{r}')}{|\mathbf{r} - \mathbf{r}'|} d\mathbf{r} d\mathbf{r}' \right] \quad (3.14)$$

Now what is left to prove is that the functional in (3.14) has the system's total ground state energy as a global minimum, and that this minimum occurs at the ground state density  $\rho_0$ . Here, for the sake of simplicity, only the non-degenerate case will be studied. Let  $\rho_0$  be the ground state density of the system, then through the mappings (3.12) and  $\mathcal{M}$  this density corresponds uniquely to some wave function  $\psi^{(0)}$  and external potential  $V_{ie}$ . Furthermore let  $H$  be the Hamiltonian corresponding to the external potential  $V_{ie}$ . If  $\rho$  is any other density with a corresponding wave function  $\psi$  chosen in such a way that the expression (3.15) is minimized, then

$$E_{HK}[\rho_0] = \langle \psi^{(0)} | H | \psi^{(0)} \rangle < \langle \psi | H | \psi \rangle = E_{HK}[\rho] \quad \square$$

### 3.3 Correlation

In the last section it was showed that the total energy of a system could be expressed as a functional of solely the density. Furthermore this expression contained a functional  $F_{HK}$  that was universal in the sense that it was independent of the external potential. Unfortunately the discussion in the previous section did not give any hint of how to actually deal with the correlation between the particles. The difficulty of solving an inseparable problem is still

left to be dealt with. Before a description of how the problem of correlation can be dealt with, some of the alternative perspectives of correlation will be discussed.

Apart from viewing correlation as a common name for the difficulties involved in solving the differential equations of  $N$  inseparable coordinates, one can take on the statistical perspective of the problem. This is intuitively clear once it is realized that quantum mechanics is nothing but a set of rules describing how the probability densities of particle states can be calculated. In statistics two variables  $\mathbf{X}$  and  $\mathbf{Y}$  with a composite probability distribution  $F_{\mathbf{X},\mathbf{Y}}(x,y)$  are said to be correlated if

$$F_{\mathbf{X},\mathbf{Y}}(x,y) \neq F_{\mathbf{X}}(x)F_{\mathbf{Y}}(y) \quad (3.15)$$

where

$$F_{\mathbf{X}}(x) = \int F_{\mathbf{X},\mathbf{Y}}(x,y)dy \quad ; \quad F_{\mathbf{Y}}(y) = \int F_{\mathbf{X},\mathbf{Y}}(x,y)dx \quad (3.16)$$

The analogy to the quantum mechanical many body problem is now obvious, with the composite distribution of the above discussion replaced by the two particle density matrix  $\rho_2(\mathbf{r},\mathbf{r}')$ . Thus particles of a many-body system are correlated if

$$\rho_2(\mathbf{r},\mathbf{r}') \neq \rho(\mathbf{r})\rho(\mathbf{r}') \quad (3.17)$$

If the particles of the system do not interact, the above inequality is replaced by an equality and the energy functional (3.14) becomes the functional for the Hartree approximation

$$E_{HARTREE}[\rho] = -\frac{1}{2} \int [\nabla^2 \rho_2(\mathbf{r},\mathbf{r}')]_{\mathbf{r}=\mathbf{r}'} d\mathbf{r} + \frac{1}{2} \int \frac{\rho(\mathbf{r})\rho(\mathbf{r}')}{|\mathbf{r}-\mathbf{r}'|} d\mathbf{r}d\mathbf{r}' + \int \rho(\mathbf{r})V_{el}(\mathbf{r})d\mathbf{r} \quad (3.18)$$

If spin and the Pauli exclusion principle are accounted for, the above Hartree expression would of course be replaced by the Hartree-Fock energy expression.

Now when the concept of correlation has been made a bit clearer, what is left to investigate is how some of the most obvious effects of correlation might be interpreted. In order to do that it is convenient to introduce the correlation function  $h(\mathbf{r},\mathbf{r}')$  defined through the relation

$$\rho_2(\mathbf{r},\mathbf{r}') = \frac{1}{2}\rho(\mathbf{r})\rho(\mathbf{r}')(1+h(\mathbf{r},\mathbf{r}')) \quad (3.19)$$

Furthermore from (3.7) the following relation can easily be derived

$$\int \rho_2(\mathbf{r},\mathbf{r}')d\mathbf{r}' = \frac{N-1}{2}\rho(\mathbf{r}) \quad (3.20)$$

Now (3.20) and (3.21) can be used to derive the so called *sum rule* of the correlation function

$$\begin{aligned} \frac{N-1}{2}\rho(\mathbf{r}) &= \int \rho_2(\mathbf{r},\mathbf{r}')d\mathbf{r}' = \frac{1}{2} \int \rho(\mathbf{r})\rho(\mathbf{r}')(1+h(\mathbf{r},\mathbf{r}'))d\mathbf{r}' \\ &= \frac{1}{2}\rho(\mathbf{r})[N + \int \rho(\mathbf{r}')h(\mathbf{r},\mathbf{r}')d\mathbf{r}'] \Rightarrow \int \rho(\mathbf{r}')h(\mathbf{r},\mathbf{r}')d\mathbf{r}' = -1 \end{aligned} \quad (3.21)$$

Now if we define the so called *exchange correlation hole*

$$\rho_{xc}(\mathbf{r}, \mathbf{r}') = \rho(\mathbf{r}')h(\mathbf{r}, \mathbf{r}') \quad (3.22)$$

the energy functional (3.14) of the many particle system can be written in the form

$$\begin{aligned} E[\rho] = & -\frac{1}{2} \int [\nabla^2 \rho_2(\mathbf{r}, \mathbf{r}')]_{\mathbf{r}=\mathbf{r}'} d\mathbf{r} + \frac{1}{2} \int \frac{\rho(\mathbf{r})\rho(\mathbf{r}')}{|\mathbf{r}-\mathbf{r}'|} d\mathbf{r}d\mathbf{r}' \\ & + \frac{1}{2} \int \frac{\rho(\mathbf{r})\rho_{xc}(\mathbf{r}, \mathbf{r}')}{|\mathbf{r}-\mathbf{r}'|} d\mathbf{r}d\mathbf{r}' + \int \rho(\mathbf{r})V_{el}(\mathbf{r})d\mathbf{r} \end{aligned} \quad (3.23)$$

From (3.22) and (3.24) one interpretation of the effects of correlation becomes clear. Namely, the correlation gives rise to a non-local distribution of holes with net charge 1, reducing the Coulomb repulsion contribution of the system.

### 3.4 The Kohn-Sham equations

In this section the first steps towards a solution of the many body problem within the DFT formalism will be reviewed. These first steps were taken by Kohn and Sham [10] in 1964. They assumed the following conjecture

**Conjecture 1** *The ground state charge density  $\rho_0$  of a many electron system, can be represented with an auxiliary non-interacting system with a non-interacting potential  $V_{KS}^\sigma$ , such that the solutions of*

$$\left[ -\frac{1}{2}\nabla^2 + V_{KS}^\sigma(\mathbf{r}) \right] \psi_i^\sigma(\mathbf{r}) = \varepsilon_i \psi_i^\sigma(\mathbf{r}) \quad (3.24)$$

satisfy

$$\rho_0(\mathbf{r}) = \sum_{\sigma} \sum_{i=1}^{N/2} |\psi_i^\sigma(\mathbf{r})|^2 \quad (3.25)$$

where  $\sigma$  is the spin index.

If the above conjecture is true then also theorem 3 holds, and the following energy functional of the density may be defined

$$E_{KS} = T_s[\rho] + \int V_{el}(\mathbf{r})\rho(\mathbf{r})d\mathbf{r} + J[\rho] + E_{xc}[\rho] \quad (3.26)$$

where

$$T_s \equiv \min_{\psi_i^\sigma \rightarrow \rho} \left[ \frac{1}{2} \sum_{\sigma} \sum_{i=1}^{N/2} \int \psi_i^\sigma(\mathbf{r})^* \nabla^2 \psi_i^\sigma(\mathbf{r}) d\mathbf{r} \right] \quad (3.27)$$

$$J[\rho] \equiv \frac{1}{2} \int \frac{\rho(\mathbf{r})\rho(\mathbf{r}')}{|\mathbf{r}-\mathbf{r}'|} d\mathbf{r}d\mathbf{r}' \quad (3.28)$$

$$E_{xc}[\rho] \text{ is such that : } E_{KS}[\rho] = E_{HK}[\rho] \quad (3.29)$$

Now the step has come to derive the Kohn-Sham equations. This is done with the help of Rayleigh-Ritz variation principle, applied to the functional  $E_{KS}$  with the auxiliary normalization conditions

$$\langle \psi_i^\sigma(\mathbf{r})^* | \psi_j^{\sigma'}(\mathbf{r}) \rangle = \delta_{ij} \delta_{\sigma\sigma'} \quad (3.30)$$

Then from basic variational calculus [11] the following functional has to be minimized with respect to the density

$$\tilde{E}[\rho] = E_{KS}[\rho] + \sum_{\sigma, \sigma'} \sum_{i,j} \varepsilon_{ij}^{\sigma\sigma'} \langle \psi_i^\sigma(\mathbf{r})^* | \psi_j^{\sigma'}(\mathbf{r}) \rangle \quad (3.31)$$

where  $\varepsilon_{ij}^{\sigma\sigma'}$  are Lagrange multipliers. However, due to the one-to-one correspondence between the density and the wave functions (established in the proof of Theorem 2), the variation can equally well be performed with respect to the wave function. Thus if (3.26) is used in (3.32) the following condition is obtained for the ground state

$$\begin{aligned} \frac{\delta T_s[\rho]}{\delta \psi_j^{\sigma'*}} + \left[ \frac{\delta J[\rho]}{\delta \rho} + \frac{\delta}{\delta \rho} \int V_{el}(\mathbf{r}) \rho(\mathbf{r}) d\mathbf{r} + \frac{\delta E_{xc}[\rho]}{\delta \rho} \right] \frac{\delta \rho}{\delta \psi_j^{\sigma'*}} \\ + \frac{\delta}{\delta \psi_j^{\sigma'*}} \sum_{\sigma, \sigma'} \sum_{i,j} \varepsilon_{ij}^{\sigma\sigma'} \langle \psi_i^\sigma(\mathbf{r})^* | \psi_j^{\sigma'}(\mathbf{r}) \rangle = 0 \end{aligned} \quad (3.32)$$

From the above equation and (3.28), (3.29) the Schrödinger like equation is found

$$\begin{aligned} -\frac{1}{2} \nabla^2 \psi_i^\sigma(\mathbf{r}) + \left[ \int \frac{\rho(\mathbf{r}')}{|\mathbf{r}-\mathbf{r}'|} d\mathbf{r}' + V_{el}(\mathbf{r}) + \frac{\delta E_{xc}[\rho]}{\delta \rho} \right] \psi_i^\sigma(\mathbf{r}) = \\ = \sum_i \sum_{\sigma'} \varepsilon_{ij}^{\sigma\sigma'} \psi_i^\sigma(\mathbf{r}) \end{aligned} \quad (3.33)$$

Since it is always possible to find a unitary transformation which transforms the basis  $\psi_i^\sigma(\mathbf{r})$  to a basis in which the Lagrangian matrix  $\varepsilon_{ij}^{\sigma\sigma'}$  is diagonal, it can be assumed that such a convenient basis already has been chosen. With this assumption the above equations are nothing more than the famous Kohn-Sham equations

$$\left[ -\frac{1}{2} \nabla^2 + V_{KS}^\sigma(\mathbf{r}) \right] \psi_i^\sigma(\mathbf{r}) = \varepsilon_i^\sigma \psi_i^\sigma(\mathbf{r}) \quad (3.34)$$

where

$$V_{KS}^\sigma(\mathbf{r}) = \int \frac{\rho(\mathbf{r}')}{|\mathbf{r}-\mathbf{r}'|} d\mathbf{r}' + V_{el}(\mathbf{r}) + \frac{\delta E_{xc}[\rho]}{\delta \rho} \quad (3.35)$$

The total energy of the system expressed in terms of Kohn-Sham eigen values is

$$E_{KS}[\rho] = \sum_{\sigma} \sum_{i=1}^N \varepsilon_i^{\sigma} - J[\rho] - \int V_{xc}(\mathbf{r})\rho(\mathbf{r})d\mathbf{r} + E_{xc}[\rho] \quad (3.36)$$

where

$$V_{xc}(\mathbf{r}) = \frac{\delta E_{xc}[\rho]}{\delta \rho} \quad (3.37)$$

### 3.5 The adiabatic connection

Even though the conjecture of Kohn and Sham might be true, as long as the exchange correlation functional  $E_{xc}$  is unknown the solution of the many body problem is light-years away. Therefore, in order to find at least an approximate expression for  $E_{xc}$ , it is important to know how the auxiliary non-interacting system of Kohn and Sham is connected to the fully interacting system. In this section such a connection will be made, this connection is called the adiabatic connection, and it is achieved by slowly turning on the electron-electron interaction from the non-interacting system to the fully interacting system.

Since  $E_{HK} = E_{KS}$  it is obtained from (3.14) and (3.27) that

$$E_{xc}[\rho] = F_{HK}[\rho] - T_s[\rho] - J[\rho] \quad (3.38)$$

Now the parameterized Hamiltonian is defined

$$H_{\lambda} = -\frac{1}{2} \sum_{i=1}^N \nabla_i^2 + \sum_{i=1}^N V_{\lambda}(\mathbf{r}_i) + \frac{\lambda}{2} \sum_{i,j=1, i \neq j}^N \frac{1}{|\mathbf{r}_i - \mathbf{r}_j|} \quad (3.39)$$

where  $\lambda \in [0, 1]$  and the potentials  $V_{\lambda}$  are defined in such a way that the solutions  $\psi_{\lambda}$  to the Schrödinger equations

$$H_{\lambda} \psi_{\lambda} = E_{\lambda} \psi_{\lambda} \quad (3.40)$$

all correspond to the same charge density  $\rho(\mathbf{r})$ , i.e

$$\int \psi_{\lambda}^*(\mathbf{r}, \mathbf{r}_1, \mathbf{r}_2, \dots, \mathbf{r}_N) \psi_{\lambda}(\mathbf{r}, \mathbf{r}_1, \mathbf{r}_2, \dots, \mathbf{r}_N) d\mathbf{r}_1 d\mathbf{r}_2 \cdots d\mathbf{r}_N = \rho(\mathbf{r}) \quad \forall \quad \lambda \in [0, 1] \quad (3.41)$$

From (3.14) the parameterized Hohenberg-Kohn functional is defined as

$$F_{HK}^{\lambda}[\rho] \equiv T_{\lambda}[\rho] + \frac{\lambda}{2} \min_{\psi_{\lambda} \rightarrow \rho} \left[ \int \frac{\rho_2^{\lambda}(\mathbf{r}, \mathbf{r}')}{|\mathbf{r} - \mathbf{r}'|} d\mathbf{r} d\mathbf{r}' \right] \quad (3.42)$$

where

$$T_{\lambda}[\rho] \equiv \min_{\psi_{\lambda} \rightarrow \rho} \left[ -\frac{1}{2} \int [\nabla \rho_2^{\lambda}(\mathbf{r}, \mathbf{r}')]_{\mathbf{r}=\mathbf{r}'} d\mathbf{r} \right] \quad (3.43)$$

From the above definitions it is then clear that the parameterized Hohenberg-Kohn functional takes on the following extreme values

$$F_{HK}^\lambda[\rho] = \begin{cases} T_s[\rho], & \lambda = 0 \\ F_{HK}[\rho], & \lambda = 1 \end{cases} \quad (3.44)$$

Now the expression (3.38) for the exchange correlation functional can be rewritten as

$$E_{xc}[\rho] = F_{HK}^{\lambda=1}[\rho] - F_{HK}^{\lambda=0}[\rho] - J[\rho] = \int_0^1 \frac{\partial F_{HK}^\lambda[\rho]}{\partial \lambda} d\lambda - J[\rho] \quad (3.45)$$

The energy of the  $\lambda$ -system can be expressed as

$$E_\lambda = \langle \psi_\lambda | H_\lambda | \psi_\lambda \rangle = F_{HK}^\lambda + \int V_\lambda(\mathbf{r}) \rho(\mathbf{r}) d\mathbf{r} \quad (3.46)$$

Derivation of the above expression with respect to  $\lambda$ , together with the application of the Hellman-Feynmann theorem gives

$$\begin{aligned} \frac{\partial E_\lambda}{\partial \lambda} &= \frac{\partial F_{HK}^\lambda}{\partial \lambda} + \int \frac{\partial V_\lambda(\mathbf{r})}{\partial \lambda} \rho(\mathbf{r}) d\mathbf{r} = \\ &= \langle \psi_\lambda | \frac{\partial H_\lambda}{\partial \lambda} | \psi_\lambda \rangle = \frac{1}{2} \int \frac{\rho_2^\lambda(\mathbf{r}, \mathbf{r}')}{|\mathbf{r} - \mathbf{r}'|} d\mathbf{r} d\mathbf{r}' + \int \frac{\partial V_\lambda(\mathbf{r})}{\partial \lambda} \rho(\mathbf{r}) d\mathbf{r} \Rightarrow \\ \frac{\partial F_{HK}^\lambda}{\partial \lambda} &= \frac{1}{2} \int \frac{\rho_2^\lambda(\mathbf{r}, \mathbf{r}')}{|\mathbf{r} - \mathbf{r}'|} d\mathbf{r} d\mathbf{r}' \end{aligned} \quad (3.47)$$

From (3.46) and (3.48) the exchange correlation energy can finally be given the form

$$E_{xc}[\rho] = \frac{1}{2} \int_0^1 \int \frac{\rho_2^\lambda(\mathbf{r}, \mathbf{r}')}{|\mathbf{r} - \mathbf{r}'|} d\mathbf{r} d\mathbf{r}' d\lambda - J[\rho] = \frac{1}{2} \int \frac{\bar{\rho}_2(\mathbf{r}, \mathbf{r}')}{|\mathbf{r} - \mathbf{r}'|} d\mathbf{r} d\mathbf{r}' - J[\rho] \quad (3.48)$$

where

$$\bar{\rho}_2(\mathbf{r}, \mathbf{r}') = \int_0^1 \rho_2^\lambda(\mathbf{r}, \mathbf{r}') d\lambda \quad (3.49)$$

Finally, the mean correlation function and the exchange correlation energy density are defined

$$\bar{\rho}_2(\mathbf{r}, \mathbf{r}') \equiv \frac{1}{2} \rho(\mathbf{r}) \rho(\mathbf{r}') [1 + \bar{h}(\mathbf{r}, \mathbf{r}')] \quad (3.50)$$

$$\varepsilon_{xc}([\rho], \mathbf{r}) = \frac{1}{2} \int \frac{\rho(\mathbf{r}') \bar{h}(\mathbf{r}, \mathbf{r}')}{|\mathbf{r} - \mathbf{r}'|} d\mathbf{r}' \quad (3.51)$$

The two above definitions can then be used to write the exchange correlation energy in the form of an integral over the exchange correlation density and the charge density

$$E_{xc}[\rho] = \int \rho(\mathbf{r}) \varepsilon_{xc}([\rho], \mathbf{r}) d\mathbf{r} \quad (3.52)$$

The recognition that the exchange correlation energy can be written in this integral form, was essential for the development of one of the most common approximations of this energy term; the local density approximation.

## 3.6 The local density approximation

Up to this point nothing has been said about how to actually find or approximate the exchange correlation functional  $E_{xc}$ . In this section however one of the most widely used approximations will be described. This approximation is commonly known as the local density approximation, and the way it is being approached here is loosely inspired by the original paper by Hohenberg and Kohn [9]. But before the actual approximation is derived, or rather made plausible, two different situations regarding the electron density will be discussed.

**Case 1 (The homogeneous electron gas)** *In this rather artificial case the electron density is kept constant by a uniformly distributed positive background charge. For the homogeneous electron gas, the exchange and correlation energy density function has been calculated with quantum Monte Carlo techniques for an extensive number of electron densities. Several different interpolation schemes exist for these simulations. Examples of such interpolation formulae can be found in for example Martin [8] and Thijssen [12]. The most important thing to notice in this case, is that the exchange correlation energy density is independent of the spatial coordinate and only depends on the constant density.*

**Case 2 (The inhomogeneous density)** *Here the exchange and correlation energy density depends strongly on the spatial coordinate, which is the case of almost all realistic situations. In the cases of inhomogeneous realistic systems the exchange correlation functional is up to this date unknown.*

Now lets assume that the charge density is that of the case 2, but that the density is varying slowly. Where the definition of a slowly varying charge density is the following.

A charge density  $\rho(\mathbf{r})$  is defined to be slowly varying if there for every  $\mathbf{r}_0 \in \mathbf{R}^3$  exists a continuously differentiable function  $\phi$  such that in a neighborhood of

$\mathbf{r}_0$  the density is described by

$$\rho(\mathbf{r}) = \phi\left(\frac{\mathbf{r}}{R}\right), \quad R \rightarrow \infty \quad (3.53)$$

Then a reasonable approximation of the exchange correlation energy density  $\varepsilon_{xc}([\rho], \mathbf{r})$  in the neighborhood of an arbitrary point  $\mathbf{r}_0$  would be

$$\varepsilon_{xc}([\rho], \mathbf{r}) \approx \varepsilon_{xc}([\rho(\mathbf{r}_0)], \mathbf{r}) \quad (3.54)$$

Furthermore, since the density is virtually constant in the neighborhood of  $\mathbf{r}_0$  it seems reasonable to approximate the exchange correlation energy function with the corresponding function of the homogeneous electron gas. This together with the arbitrary choice of the point  $\mathbf{r}_0$ , leads to the approximation of the explicit dependence of  $\mathbf{r}$  in  $\varepsilon_{xc}([\rho], \mathbf{r})$ , with an implicit dependence in the corresponding function of the homogeneous electron gas, i.e

$$\varepsilon_{xc}([\rho], \mathbf{r}) \approx \varepsilon_{xc}^{hom}(\rho(\mathbf{r})) \quad (3.55)$$

The above approximation is the famous local density approximation (LDA), and it has provided DFT with many of its successes in predicting correct ground state properties of many of the pure metals and their respective alloys.

One of the most easily derived correlation functions is that of the exchange energy for the homogeneous electron gas

$$E_x^{hom}[\rho] = -\frac{1}{2} \left[ \frac{81}{\pi} \right]^{\frac{1}{3}} (a_0^3 \rho)^{\frac{1}{3}} \quad (3.56)$$

The derivation can be found in Ashcroft [13]. This expression was first used by Slater in an attempt to approximate the Hartree-Fock equations for systems with non-uniform charge densities. This approximation is equivalent to the LDA, with the exception that correlation is not accounted for. It is one of the first steps towards the DFT of today.



## 4. Methods for calculating band structure

In this chapter, some of the methods used to solve the Kohn-Sham equations for a periodic potential will be discussed. These methods constitute the essential ingredients in calculating the electronic structure of materials, and they are often referred to as band structure methods. The methods being reviewed here are the KKR-ASA, LMTO-ASA, FP-LMTO, pseudo potential and the LAPW method. The KKR-ASA method is interesting to study for two reasons. The first reason is that it provides a solid, and physical transparent ground for the canonical band theory. Later on in this thesis this theory will be used to explain the phenomenon of super-plasticity among the transition metal alloys. The second reason is that it provides a good pedagogical background to the FP-LMTO method, which is the method that has been used in many of the calculations of this thesis. The review of the KKR-ASA method will follow the book of Skriver [14], while the discussion of the LMTO and FP-LMTO methods will be based on Wills [15] and Trygg [16].

### 4.1 The KKR-ASA method

First it might be in order to explain what the short notation KKR-ASA stands for. ASA is the short notation for the atomic sphere approximation, where KKR is the short notation for the names Korringa, Kohn and Rostoker. These are the names of the men that first came across the non-linear secular equation that is in the core of this method.

The first step in this method is to divide the crystal into overlapping atomic spheres around each atom of the solid, see Fig.4.1. Each sphere is then considered separately, with the potential of the sphere approximated by

$$V_{asa}(\mathbf{r}) = \begin{cases} V_{KS}(\mathbf{r}), & |\mathbf{r}| \leq S \\ V_{MT}, & |\mathbf{r}| > S \end{cases} \quad (4.1)$$

Observe that the potential  $V_{MT}$  outside the sphere is set so that the kinetic energy of the solutions in this region will be zero. If the Schrödinger equation

$$\left[ -\frac{1}{2}\nabla^2 + V_{asa}(\mathbf{r}) - E \right] \Psi(E, \mathbf{r}) = 0 \quad (4.2)$$

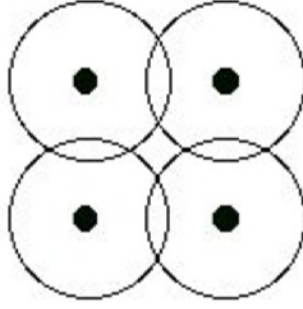


Figure 4.1: Two dimensional picture of the division of a crystal in atomic spheres

for this choice of potential is solved, the following solutions are obtained

$$\Psi_l(E, \mathbf{r}) = Y_l^m(\hat{r}) \begin{cases} \psi_l(E, r), & |\mathbf{r}| \leq S \\ A \left(\frac{s}{r}\right)^{l+1} + B \left(\frac{r}{s}\right)^l, & |\mathbf{r}| > S \end{cases} \quad (4.3)$$

where  $\psi_l(E, \mathbf{r})$  is the solution to the radial Schrödinger equation

$$\left[ -\frac{1}{2} \frac{\partial^2}{\partial r^2} + \frac{l(l+1)}{2r^2} + V_{KS}(r) - E \right] r\psi_l(E, r) = 0. \quad (4.4)$$

Now, it might be tempting to create a trial function as a linear combination of the solutions (4.3), and treat the problem in a tight binding fashion. However, since these functions are energy dependent, the structural information and the potential dependency of the problem would be completely mixed in the resulting secular equation. Thus such an approach would lead forward to a set of non-linear equations with low physical transparency, which are very time consuming to solve. Instead the following, so-called muffin tin orbitals (MTOs), are used

$$\chi_{lm}(E, \mathbf{r}) = i^l Y_l^m(\hat{r}) \begin{cases} \psi_l(E, r) + \mathcal{P}_l(E) \left(\frac{r}{s}\right)^l, & |\mathbf{r}| \leq S \\ \left(\frac{s}{r}\right)^{l+1}, & |\mathbf{r}| > S \end{cases} \quad (4.5)$$

where

$$\mathcal{P}_l(E) = \frac{\mathcal{D}_l(E) + l + 1}{\mathcal{D}_l(E) - l} \quad (4.6)$$

$$\mathcal{D}_l(E) = \left( \frac{S}{\psi_l(E, r)} \frac{\partial \psi_l(E, r)}{\partial r} \right)_{r=S}. \quad (4.7)$$

Here  $\mathcal{P}_l$  is the potential function, defined in such a way that the function  $\chi_{lm}$  is both continuous and differentiable at the sphere boundary. Now, the following function is constructed from the MTOs

$$\Phi_{l\mathbf{k}}(\mathbf{r}) = \sum_{\mathbf{R}} \sum_{l,m} a_{lm}^{\mathbf{k}} \chi_{lm}(\mathbf{r} - \mathbf{R}) e^{i\mathbf{k}\mathbf{R}}. \quad (4.8)$$

Instead of using the above function as a trial function in a variational approach, the following expansion theorem for the tails of (4.8) will be taken advantage of

$$\sum_{\mathbf{R} \neq \mathbf{0}} e^{i\mathbf{k}\mathbf{R}} \left( \frac{S}{|\mathbf{r} - \mathbf{R}|} \right)^{l+1} i^l Y_l^m(\widehat{\mathbf{r} - \mathbf{R}}) = \sum_{l'm'} \frac{-1}{2(2l+1)} \left( \frac{r}{S} \right)^{l'} i^{l'} Y_{l'}^{m'}(\hat{r}) S_{l'm',lm}^{\mathbf{k}} \quad (4.9)$$

where

$$S_{l'm',lm}^{\mathbf{k}} = g_{l'm',lm} \sum_{\mathbf{R} \neq \mathbf{0}} \left( \frac{S}{R} \right)^{l+l'+1} \left[ \sqrt{4\pi} i^{l+l'} Y_{l+l'}^{m+m'}(\hat{\mathbf{R}}) \right]^* \quad (4.10)$$

$$g_{l'm',lm} = 2(-1)^{m+1} \left[ \frac{(2l'+1)(2l+1)(l+l'+m+m')!(l+l'-m-m')!}{(2(l+l')+1)(l'+m')!(l'-m')!(l+m)!(l-m)!} \right]^{\frac{1}{2}} \quad (4.11)$$

The coefficients  $S_{l'm',lm}^{\mathbf{k}}$  are called the canonical structure constants. The coefficients  $g_{l'm',lm}$  are closely related to the standard Gaunt coefficients.

If  $\mathbf{r}$  is inside of an atomic sphere centered at an arbitrary point, say  $\mathbf{R}'$ , defining this point as origo, the above expansion can be used to write the wave function (4.8) as

$$\begin{aligned} \Phi_{l\mathbf{k}}(\mathbf{r}) &= \sum_{l,m} a_{lm} \left[ \chi_{lm}(\mathbf{r}) + \sum_{\mathbf{R} \neq \mathbf{0}} \chi_{lm}(\mathbf{r} - \mathbf{R}) e^{i\mathbf{k}\mathbf{R}} \right] = \\ &= \sum_{l,m} \sum_{l',m'} a_{lm}^{\mathbf{k}} i^{m'} Y_{l'}^{m'}(\hat{r}) \left( \psi_l(E, r) \delta_{ll'} \delta_{mm'} + \right. \\ &\quad \left. \left( \frac{r}{S} \right)^{l'} \left[ \mathcal{P}_{l'}(E) \delta_{ll'} \delta_{mm'} - \frac{S_{l'm',lm}^{\mathbf{k}}}{2(2l'+1)} \right] \right). \end{aligned} \quad (4.12)$$

However if  $\mathbf{r}$  is not inside any of the atomic spheres, the wave function simply becomes a block sum of tails

$$\Phi_{l\mathbf{k}}(\mathbf{r}) = \sum_{\mathbf{R}} \sum_{l,m} a_{lm}^{\mathbf{k}} \left( \frac{S}{|\mathbf{r} - \mathbf{R}|} \right)^{l+1} e^{i\mathbf{k}\mathbf{R}}. \quad (4.13)$$

From the above discussion it is easy to see that the wave function is an exact solution (within ASA), if the term within the square-brackets of (4.12) vanishes, i.e

$$\sum_{l,m} a_{lm}^{\mathbf{k}} \left[ \mathcal{P}_l(E) \delta_{ll'} \delta_{mm'} - \frac{S_{l'm',lm}^{\mathbf{k}}}{2(2l'+1)} \right] = 0. \quad (4.14)$$

These equations are the so-called KKR-ASA equations. From the above expression it becomes obvious that the potential function  $\mathcal{P}_l$  is closely related

to the phase shift that the tail is being subject to when scattered by the surrounding atomic spheres. The non-trivial solutions  $a_{lm}^{\mathbf{k}}$  of (4.14) are obtained for those values  $E = E_{\mathbf{k}j}$  that satisfy

$$\det [2(2l+1) \mathcal{P}_l(E) \delta_{ll'} \delta_{mm'} - S_{l'm',lm}^{\mathbf{k}}] = 0. \quad (4.15)$$

Unfortunately the above equations are non-linear, and can in principle only be solved exactly if the potential function  $\mathcal{P}_l$  is calculated by solving the equation (4.4) for an extensive number of energies. This however is a very time consuming process, and what is done instead is that the potential function is parameterized around the energy of interest. In the next section the simplest of these parameterizations will be presented. However something good has also come out of the above approach; the potential and the structural parts of the problem have been separated.

### 4.1.1 Canonical band theory

In this section a review of the so-called canonical band theory will be presented. This theory was originally developed by Andersen [17], and it is based on the KKR-ASA method discussed previously.

A good starting point for this review, is to look at the structure constants  $S_{lm,l'm'}^{\mathbf{k}}$ . These constants can by means of a unitary transformation  $U$ , formally written as

$$S_{lm,l'm'}^{\mathbf{k}} \xrightarrow{U} S_{li,l'i'}^{\mathbf{k}}, \quad (4.16)$$

be brought to a diagonal form

$$S_{li,l'i'}^{\mathbf{k}} = S_{li,l'i'}^{\mathbf{k}} \delta_{i'i} \equiv S_{li}^{\mathbf{k}} \delta_{i'i} \quad (4.17)$$

Further more, if the off-diagonal hybridized blocks are approximated to be zero, the equation (4.15) reduces to

$$2(2l+1) \mathcal{P}_l(E) = S_{li}^{\mathbf{k}} \quad (4.18)$$

Solving this equation will relate the band-structure to the canonical l-band  $S_{li}^{\mathbf{k}}$ . In order to solve (4.18) in the simplest possible way, a parameterization of the potential function  $\mathcal{P}_l$  is made. One of the simplest parameterizations is given by

$$\mathcal{P}_l(E) \approx \frac{1}{2(2l+1)\gamma_l} \frac{E - C_l}{E - V_l} \quad (4.19)$$

where the parameters  $V_l$ ,  $C_l$  and  $\gamma_l$  are defined by

$$\mathcal{D}_l(V_l) = l \quad (4.20)$$

$$\mathcal{D}_l(C_l) = -l - 1 \quad (4.21)$$

$$\gamma_l = \frac{1}{2(2l+1)} \frac{\mathcal{D}_{\dot{v}} - l}{\mathcal{D}_{\dot{v}} + l + 1} \quad (4.22)$$

$$\mathcal{D}_v \equiv \left( \frac{S}{\psi_l(E_{vl}, r)} \frac{\partial \psi_l(E_{vl}, r)}{\partial r} \right)_{r=S} \quad (4.23)$$

$$\psi_l(E_{vl}, r) \equiv \left( \frac{\partial \psi_l(E, r)}{\partial E} \right)_{E=E_{vl}} \quad (4.24)$$

The details of how this parameterization is derived, and how the energy  $E_{vl}$  is chosen are described in the book of Skriver [14].

If the parameterization (4.19) is used with equation (4.18) the energies of bands can be expressed by means of the canonical bands  $S_{li}^{\mathbf{k}}$  as

$$E_{li}(\mathbf{k}) \approx C_l + \frac{1}{\mu_l S^2} \frac{S_{li}^{\mathbf{k}}}{1 - \gamma_l S_{li}^{\mathbf{k}}} \quad (4.25)$$

where

$$\mu_l \equiv \frac{1}{\gamma_l (C_l - V_l) S^2} \quad (4.26)$$

The remarkably simple formula (4.25) will later be used in chapter 7, where the search for superplastic transition metal alloys is presented.

## 4.2 The LMTO method

The LMTO method is a variational method, where the energy dependence of the basis set is suppressed by a linearization of the basis functions with respect to energy. The starting point of this method is to divide the entire crystal into non-overlapping spheres of radius  $S_{mt}$  around each atomic site. Here only the case of one atom per unit-cell will be considered, for the more general case of many atoms per cell see Trygg [16] or Wills [15]. In the next step the so-called linear muffin tin orbitals (LMTOs) are constructed from the solutions of the Schrödinger equation

$$\left[ -\frac{1}{2} \nabla^2 + V_{MF}(r) \right] \phi(\mathbf{r}) = E \phi(\mathbf{r}) \quad (4.27)$$

where the potential  $V_{mft}(r)$  is the so-called muffin tin potential defined by

$$V_{MF}(r) = \begin{cases} V(r), & r \leq S_{mt} \\ V_{MFT}, & r > S_{mt} \end{cases} \quad (4.28)$$

where  $V(r)$  is the spherically symmetric part of the Kohn-Sham potential centered at one of the atomic sites, and  $V_{MFT} = V(S_{mt})$ . The solutions of (4.27) are given by

$$\phi_{lm}(\mathbf{r}) = i^l Y_l^m(\hat{r}) \begin{cases} \psi_l(E, r), & r \leq S_{mt} \\ \mathcal{X}_l(\kappa r), & r > S_{mt} \end{cases} \quad (4.29)$$

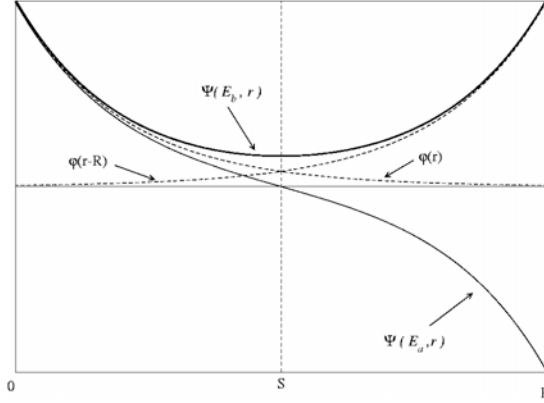


Figure 4.2: Bonding  $\psi(E_b, \mathbf{r})$  and anti-bonding  $\psi(E_a, \mathbf{r})$  LCAO solutions of the hydrogen molecule.

where

$$\mathcal{X}_l(\kappa r) = -\kappa^{l+1} \begin{cases} n_l(\kappa r), & \kappa^2 \geq 0 \\ n_l(\kappa r) - i j_l(\kappa r) = -i h_l(\kappa r), & \kappa^2 < 0 \end{cases} \quad (4.30)$$

$$\kappa^2 = E - V_{MFT} \quad (4.31)$$

Here  $j_l(\kappa r)$ ,  $n_l(\kappa r)$  and  $h_l(\kappa r)$  are spherical Bessel Neumann and Hankel functions, respectively.

Now in order to understand the motive behind the construction of the LMTO variational basis set from the solutions (4.29), we will discuss the LCAO treatment of the hydrogen molecule, and compare it with the case of a solid. In this simple approach the variational basis consists of two atomic s-orbitals  $\psi(\mathbf{r})$  and  $\psi(\mathbf{r} - \mathbf{R})$  centered at  $\mathbf{r}$  and  $\mathbf{R}$ , respectively. The two solutions are given by

$$\psi(E_b, \mathbf{r}) = \frac{1}{\sqrt{2}} [\psi(\mathbf{r}) + \psi(\mathbf{r} - \mathbf{R})] \quad (4.32)$$

$$\psi(E_a, \mathbf{r}) = \frac{1}{\sqrt{2}} [\psi(\mathbf{r}) - \psi(\mathbf{r} - \mathbf{R})] \quad (4.33)$$

where  $\psi(E_b, \mathbf{r})$  and  $\psi(E_a, \mathbf{r})$  are the bonding and anti-bonding states, respectively, corresponding to the energies  $E_b$  and  $E_a$ . In a solid the energies  $E_b$  and  $E_a$  would correspond to the bottom and the top of the energy band. Furthermore it is seen from Figure 4.2 that the tail of the wave function centered at  $\mathbf{R}$  determines the slope and amplitude of the solutions (4.32-4.33) at the boundary  $S$ . Thus if the analogy is extended to the wave functions in a solid, the slope and amplitude of a wave on the muffin tin boundary is determined by the tails coming from the surrounding muffin tins.

Hence the energy dependence of the wave function inside a muffin tin should be supplied by a logarithmic derivative of the tails from the other sites. Let's assume that the basis set is such that the basis functions inside the muffin tin spheres can be written in the following form

$$\phi_{lm}(\mathcal{D}, \mathbf{r}) = \psi_{lm}(E_V, \mathbf{r}) + \omega(\mathcal{D})\psi_{lm}(E_V, \mathbf{r}) \quad (4.34)$$

where

$$\psi_{lm}(E_V, \mathbf{r}) = i^l Y_l^m(\hat{r}) \psi_l(E_V, r) \quad (4.35)$$

$$\omega(\mathcal{D}) = -\frac{\psi_l(E_V, r)}{\dot{\psi}_l(E_V, r)} \frac{\mathcal{D} - \mathcal{D}_V}{\mathcal{D} - \mathcal{D}_l} \quad (4.36)$$

$$\mathcal{D}_V \equiv \left( \frac{S}{\psi_l(E_V, r)} \frac{\partial \psi_l(E_V, r)}{\partial r} \right)_{r=S} \quad (4.37)$$

Here the factor  $\omega(\mathcal{D})$  has been defined to assure that the trial function (4.34) has logarithmic derivative equal to  $\mathcal{D}$ . The wave functions  $\psi_l(E_V, r)$  are defined by (4.29), and are normalized according to

$$\int_0^S \psi_l^*(E_V, r) \psi_l(E_V, r) r^2 dr = 1 \quad (4.38)$$

Furthermore the logarithmic derivative  $\mathcal{D}$  is here assumed to be determined by the tails from the surrounding muffin tins. To make the coupling between the energy dependence and the logarithmic derivative a bit more explicit, we note that (4.34) is equivalent to the first two terms of the Taylor expansion around the energy  $E_V$  of the wave function  $\psi_{lm}(E, \mathbf{r})$  with energy  $E = \omega(\mathcal{D}) + E_V$ .

$$\psi_{lm}(E, \mathbf{r}) = \psi_{lm}(E_V, \mathbf{r}) + \omega(\mathcal{D})\psi_{lm}(E_V, \mathbf{r}) + \mathcal{O}(|E - E_V|^2) \quad (4.39)$$

Now let's calculate the variational estimate of the energy for the trial function (4.34). To do this, the following easily proven relation (see Skriver [14]) will be needed.

$$[H - E] \psi_{lm}(E, \mathbf{r}) = \psi_{lm}(E, \mathbf{r}) \quad (4.40)$$

where  $H$  is the Hamiltonian corresponding to the Schrödinger equation (4.27). With above relation the following is obtained

$$\langle \phi_{l'm'}(\mathcal{D}, \mathbf{r}) | H - E_V | \phi_{lm}(\mathcal{D}, \mathbf{r}) \rangle = \omega(\mathcal{D}) \delta_{l'l'} \delta_{mm'} \quad (4.41)$$

$$\langle \phi_{l'm'}(\mathcal{D}, \mathbf{r}) | \phi_{lm}(\mathcal{D}, \mathbf{r}) \rangle = \delta_{l'l'} \delta_{mm'} (1 + \omega^2(\mathcal{D}) \langle \dot{\psi}_{lm} | \dot{\psi}_{lm} \rangle) \quad (4.42)$$

Finally, with the help of (4.41) and (4.42) the variational estimate of the energy is calculated

$$\begin{aligned}
E &= \frac{\langle \psi_{lm}(E, \mathbf{r}) | H | \psi_{lm}(E, \mathbf{r}) \rangle}{\langle \psi_{lm}(E, \mathbf{r}) | \psi_{lm}(E, \mathbf{r}) \rangle} = \\
&= \frac{\langle \phi_{lm}(\mathcal{D}, \mathbf{r}) | H | \phi_{lm}(\mathcal{D}, \mathbf{r}) \rangle}{\langle \phi_{lm}(\mathcal{D}, \mathbf{r}) | \phi_{lm}(\mathcal{D}, \mathbf{r}) \rangle} + \mathcal{O}(|E - E_v|^3) = \\
&= E_v + \frac{\langle \phi_{lm}(\mathcal{D}, \mathbf{r}) | H - E_v | \phi_{lm}(\mathcal{D}, \mathbf{r}) \rangle}{\langle \phi_{lm}(\mathcal{D}, \mathbf{r}) | \phi_{lm}(\mathcal{D}, \mathbf{r}) \rangle} + \mathcal{O}(|E - E_v|^3) = \\
&= E_v + \frac{\omega(\mathcal{D})}{1 + \omega^2(\mathcal{D}) \langle \psi_{lm} | \psi_{lm} \rangle} + \mathcal{O}(|E - E_v|^3) \tag{4.43}
\end{aligned}$$

From the above discussion we see that the energy estimate is correct to 3:rd order and the function (4.34) to 2:nd order. Thus if a basis set is constructed in such a way that the energy dependence of the basis functions inside the muffin tins is supplied by the tails, energy bands of arbitrarily good accuracy (within the approximation of  $E_{xc}$ ) can be obtained provided the linearization energies  $E_v$  and tail energies  $\kappa^2$  are wisely chosen.

#### 4.2.1 The linear muffin tin orbitals

In the previous section the basic principle for constructing a so-called LMTO basis set was discussed. The main idea was first to linearize the basis functions inside the muffin tin spheres with respect to energy. Then letting the resulting linear energy dependence be determined by the logarithmic derivative (on the muffin tin sphere) of the tails from the surrounding spheres. In this section it will be discussed in detail how this construction is performed.

In the interstitial region the basis set is already defined by the Bloch-sum of the tail functions  $\mathcal{H}_{lm}(\boldsymbol{\kappa}, \mathbf{r}) = i^l Y_l^m(\hat{r}) \mathcal{H}_l(\boldsymbol{\kappa} r)$

$$\chi_{lm}^{\mathbf{k}}(\boldsymbol{\kappa}, \mathbf{r})|_{\mathbf{r} \in \mathcal{I}} = \sum_{\mathbf{R}} \mathcal{H}_{lm}(\boldsymbol{\kappa}, \mathbf{r} - \mathbf{R}) e^{i\mathbf{k}\mathbf{R}}, \tag{4.44}$$

where

$$\mathbf{r} \in \mathcal{I} \Leftrightarrow |\mathbf{r} - \mathbf{R}| > S_{mt}, \quad \forall \mathbf{R}. \tag{4.45}$$

In the following we will make use of an expansion theorem for the functions  $\mathcal{H}$ , that allows these functions to be expanded in spherical Bessel functions around any point except the point at which the function  $\mathcal{H}$  is centered. This theorem can be stated explicitly as

$$\begin{aligned}
\mathcal{H}_L(\boldsymbol{\kappa}, \mathbf{r} - \mathbf{R}) &= \sum_{L'} \mathcal{J}_{L'}(\boldsymbol{\kappa}, \mathbf{r} - \mathbf{R}') \mathcal{B}_{L',L}(\boldsymbol{\kappa}, \mathbf{R} - \mathbf{R}') \\
&|\mathbf{r} - \mathbf{R}| < S_{mt} \quad \forall \mathbf{R}' \neq \mathbf{R} \tag{4.46}
\end{aligned}$$

where

$$L \equiv (l, m) \quad ; \quad \mathcal{H}_L \equiv \mathcal{H}_{lm} \quad ; \quad \mathcal{J}_{L'} = i^l Y_l^m j_l / \kappa^l \tag{4.47}$$

The structure constants  $\mathcal{B}_{L,L}$  are equivalent to the KKR structure constants for the general case of  $\kappa \neq 0$ <sup>1</sup>.

Now if the argument  $\mathbf{r}$  in (4.44) is on the boundary of a muffin tin, centered at say  $\mathbf{R}' \equiv \mathbf{0}$ , then we can use the expansion (4.46) and rewrite the Bloch-sum (4.44) as a sum of functions centered at  $\mathbf{0}$ , i.e.

$$\begin{aligned} \chi_L^{\mathbf{k}}(\kappa, \mathbf{r})|_{r=S_{mt}} &= \mathcal{K}_L(\kappa, \mathbf{r}) + \sum_{\mathbf{R} \neq \mathbf{0}} \mathcal{K}_{l_m}(\kappa, \mathbf{r} - \mathbf{R}) e^{i\mathbf{k}\mathbf{R}} = \\ \sum_L \left[ \mathcal{K}_{L'}(\kappa, \mathbf{r}) \delta_{LL'} + \mathcal{J}_{L'}(\kappa, \mathbf{r}) \sum_{\mathbf{R} \neq \mathbf{0}} \mathcal{B}_{L',L}(\kappa, \mathbf{R}) e^{i\mathbf{k}\mathbf{R}} \right] &= \\ = \sum_L \left[ \mathcal{K}_{L'}(\kappa, \mathbf{r}) \delta_{LL'} + \mathcal{J}_{L'}(\kappa, \mathbf{r}) \mathcal{B}_{L',L}(\kappa, \mathbf{k}) \right], \end{aligned} \quad (4.48)$$

where

$$\mathcal{B}_{L',L}(\kappa, \mathbf{k}) \equiv \sum_{\mathbf{R} \neq \mathbf{0}} \mathcal{B}_{L',L}(\kappa, \mathbf{R}) e^{i\mathbf{k}\mathbf{R}} \quad (4.49)$$

With the help of (4.48) it is now easy to see how the linearized functions (4.34) can be used to define the basis set inside the muffin tin. By requiring that the basis functions are continuous and differentiable on the muffin tin boundary, the tails of the wave function stipulate the following basis set inside the muffin tin

$$\begin{aligned} \chi_L^{\mathbf{k}}(E, \kappa, \mathbf{r})|_{r \leq S_{mt}} &= \\ \sum_L \left[ \delta_{LL'} \frac{\mathcal{K}_l(\kappa S_{mt})}{\phi_L(\mathcal{D}(\mathcal{K}_l), S_{mt})} \phi_L(\mathcal{D}(\mathcal{K}_l), \mathbf{r}) + \right. \\ \left. + \mathcal{B}_{L',L}(\kappa, \mathbf{k}) \frac{\mathcal{J}_l(\kappa S_{mt})}{\phi_L(\mathcal{D}(\mathcal{J}_l), S_{mt})} \phi_L(\mathcal{D}(\mathcal{J}_l), \mathbf{r}) \right], \end{aligned} \quad (4.50)$$

where

$$\mathcal{D}(\mathcal{K}_l) \equiv \left( \frac{S_{mt}}{\mathcal{K}_l(\kappa r)} \frac{\partial \mathcal{K}_l(\kappa r)}{\partial r} \right)_{r=S_{mt}} \quad (4.51)$$

$$\mathcal{D}(\mathcal{J}_l) \equiv \left( \frac{S_{mt}}{\mathcal{J}_l(\kappa r)} \frac{\partial \mathcal{J}_l(\kappa r)}{\partial r} \right)_{r=S_{mt}} \quad (4.52)$$

<sup>1</sup>See Reference, [16] page 82

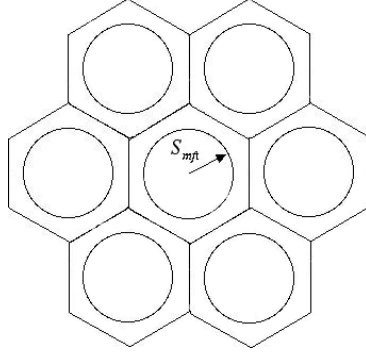


Figure 4.3: Two dimensional picture of the division of a crystal into atomic polyhedra

By introducing the matrices

$$\Omega_l(E, \kappa) = \begin{pmatrix} \frac{\mathcal{K}_l(\kappa S_{mt})}{\phi_L(\mathcal{D}(\mathcal{K}_l), S_{mt})} & \frac{\mathcal{J}_l(\kappa S_{mt})}{\phi_L(\mathcal{D}(\mathcal{J}_l), S_{mt})} \\ \frac{\mathcal{K}_l(\kappa S_{mt})}{\phi_L(\mathcal{D}(\mathcal{K}_l), S_{mt})} \omega(\mathcal{D}(\mathcal{K}_l)) & \frac{\mathcal{J}_l(\kappa S_{mt})}{\phi_L(\mathcal{D}(\mathcal{J}_l), S_{mt})} \omega(\mathcal{D}(\mathcal{J}_l)) \end{pmatrix} \quad (4.53)$$

$$\mathcal{U}_L(E, \mathbf{r}) = (\psi_L(E, \mathbf{r}), \psi_L(E, \mathbf{r})) \quad ; \quad \mathcal{S}_{L',L}(\kappa, \mathbf{k}) = \begin{pmatrix} \delta_{LL} \\ \mathcal{B}_{L',L}(\kappa, \mathbf{k}) \end{pmatrix} \quad (4.54)$$

the basis functions inside the muffin tins (4.50) can be written in the more compact form

$$\chi_L^{\mathbf{k}}(E, \kappa, \mathbf{r})|_{r \leq S_{mt}} = \sum_{L'} \mathcal{U}_{L'}(E, \mathbf{r}) \Omega_{L'}(E, \kappa) \mathcal{S}_{L',L}(\kappa, \mathbf{k}) \quad (4.55)$$

## 4.2.2 The secular equation

With the LMTO basis functions defined by (4.50) and (4.44) the following trial function

$$\phi_{\mathbf{k}}(\mathbf{r}) = \sum_i \mathcal{A}_i^{\mathbf{k}} \chi_{L_i}^{\mathbf{k}}(E_i, \kappa_i, \mathbf{r}) \quad (4.56)$$

can now be defined. With the help of this trial function a variational estimate of the solutions to the Kohn-Sham equations can now be calculated. This is done by minimizing the the energy estimate

$$E = \frac{\langle \phi_{\mathbf{k}}(\mathbf{r}) | H | \phi_{\mathbf{k}}(\mathbf{r}) \rangle}{\langle \phi_{\mathbf{k}}(\mathbf{r}) | \phi_{\mathbf{k}}(\mathbf{r}) \rangle} = \frac{\sum_{j,i} \mathcal{A}_i^{\mathbf{k}*} \mathcal{A}_j^{\mathbf{k}} \langle \chi_{L_i}^{\mathbf{k}}(E_i, \kappa_i, \mathbf{r}) | H | \chi_{L_j}^{\mathbf{k}}(E_j, \kappa_j, \mathbf{r}) \rangle}{\sum_{j,i} \mathcal{A}_i^{\mathbf{k}*} \mathcal{A}_j^{\mathbf{k}} \langle \chi_{L_i}^{\mathbf{k}}(E_i, \kappa_i, \mathbf{r}) | \chi_{L_j}^{\mathbf{k}}(E_j, \kappa_j, \mathbf{r}) \rangle} \quad (4.57)$$

with respect to the coefficients  $\mathcal{A}_i^{\mathbf{K}^*}$ . This produces the following linear equations

$$\frac{\partial E}{\partial \mathcal{A}_i^{\mathbf{K}^*}} = 0 \quad \Rightarrow \quad \sum_j [\mathcal{H}_{ij}^{\mathbf{k}} - E \mathcal{O}_{ij}^{\mathbf{k}}] \mathcal{A}_j^{\mathbf{k}} = 0 \quad (4.58)$$

where

$$\mathcal{H}_{ij}^{\mathbf{k}} = \langle \chi_{L_i}^{\mathbf{k}}(E_i, \kappa_i, \mathbf{r}) | H | \chi_{L_j}^{\mathbf{k}}(E_j, \kappa_j, \mathbf{r}) \rangle \quad (4.59)$$

$$\mathcal{O}_{ij}^{\mathbf{k}} = \langle \chi_{L_i}^{\mathbf{k}}(E_i, \kappa_i, \mathbf{r}) | \chi_{L_j}^{\mathbf{k}}(E_j, \kappa_j, \mathbf{r}) \rangle \quad (4.60)$$

To find the non-trivial solutions to the above linear equations the corresponding secular equation

$$\det [\mathcal{H}_{ij}^{\mathbf{k}} - E \mathcal{O}_{ij}^{\mathbf{k}}] = 0 \quad (4.61)$$

has to be solved.

### 4.2.3 The FP-LMTO treatment

The calculation of the matrix elements (4.59) and (4.60) are simplified by dividing the lattice into polyhedra (Fig. 4.3), and making use of the fact that the LMTO basis functions can be centered around any lattice point. If  $\mathcal{V}_{\mathbf{R}}$  is the volume of such an polyhedron centered at  $\mathbf{R}$  then

$$\mathcal{H}_{ij}^{\mathbf{k}} = \sum_{\mathbf{R}} \langle \chi_{L_i}^{\mathbf{k}}(E_i, \kappa_i, \mathbf{r}) | H | \chi_{L_j}^{\mathbf{k}}(E_j, \kappa_j, \mathbf{r}) \rangle_{\mathcal{V}_{\mathbf{R}}} = N \langle \chi_{L_i}^{\mathbf{k}}(E_i, \kappa_i, \mathbf{r}) | H | \chi_{L_j}^{\mathbf{k}}(E_j, \kappa_j, \mathbf{r}) \rangle_{\mathcal{V}_0} \quad (4.62)$$

$$\mathcal{O}_{ij}^{\mathbf{k}} = \sum_{\mathbf{R}} \langle \chi_{L_i}^{\mathbf{k}}(E_i, \kappa_i, \mathbf{r}) | \chi_{L_j}^{\mathbf{k}}(E_j, \kappa_j, \mathbf{r}) \rangle_{\mathcal{V}_{\mathbf{R}}} = N \langle \chi_{L_i}^{\mathbf{k}}(E_i, \kappa_i, \mathbf{r}) | \chi_{L_j}^{\mathbf{k}}(E_j, \kappa_j, \mathbf{r}) \rangle_{\mathcal{V}_0} \quad (4.63)$$

where  $N$  is the number of unit cells.

In the above summation over polyhedra we have assumed that in this treatment there is only one atom per unit cell, thus all the polyhedral integrals are equal and the only integrals that have to be calculated are those centered at  $\mathbf{R} = \mathbf{0}$ .

When calculating the Hamiltonian matrix (4.62) the Hamiltonian is divided in the following way

$$H = H_0 + V_{NMF} + V_{\mathcal{J}} \quad (4.64)$$

By letting  $V(r)$  be the spherical symmetric part of the Kohn-Sham potential centered at an atomic site, the terms appearing above are defined as follows

$$H_0 = \begin{cases} -\frac{1}{2} \nabla^2 + V(r), & r \leq S_{mt} \\ -\frac{1}{2} \nabla^2, & r > S_{mt} \end{cases} \quad (4.65)$$

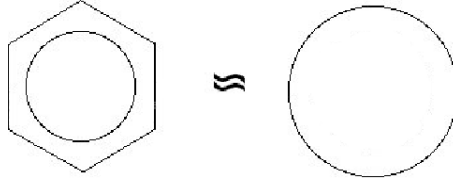


Figure 4.4: Two dimensional picture of the approximation of the polyhedra with atomic spheres

$$V_{NMF} = \begin{cases} V_{KS}(\mathbf{r}) - V(r), & r \leq S_{mt} \\ 0, & r > S_{mt} \end{cases} \quad (4.66)$$

$$V_{\mathcal{J}} = \begin{cases} 0, & r \leq S_{mt} \\ V_{KS}(\mathbf{r}), & r > S_{mt} \end{cases} \quad (4.67)$$

How the integrals in (4.62) and (4.63) are calculated with the above division of the Hamiltonian, and how the general case of several atoms per unit cell is treated, will not be discussed here. Those interested can turn to Ref. [16, 15].

### 4.3 The LMTO-ASA method

In the LMTO-ASA method only the spherically symmetric part of the Kohn-Sham potential is used in the Hamiltonian. (Hence the exclusion of the prefix FP in the name of the method). Otherwise the LMTO-ASA and the FP-LMTO method are very similar, in that they use essentially the same basis sets and are both variational methods.

In this section we will see that two extra approximations, apart from the one described above, will greatly simplify the calculations of the Hamiltonian and overlap matrix elements. This section is based on Ref. [14].

The first approximation is that the polyhedra in which the lattice has been divided are approximated by spheres (Fig. 4.4). The spherical symmetry of the potential then permits the angular part of the integrals in (4.62) and (4.63) to be performed separately. The second approximation is that the muffin tin spheres are set equal to the atomic spheres (the approximated polyhedra). This means that the integration involved in the calculation of the matrix elements above will always stay within the muffin tin. Thus the LMTO basis functions are completely defined by (4.50), and the LMTO-ASA matrix elements are given by

$$\mathcal{H}_{ij}^{\mathbf{k}} = \left[ \langle \widetilde{\mathcal{H}}_{i_j} | H - E_V | \widetilde{\mathcal{H}}_{i_j} \rangle + E_V \langle \widetilde{\mathcal{H}}_{i_j} | \widetilde{\mathcal{H}}_{i_j} \rangle \right] \delta_{L_i L_j} +$$

$$\begin{aligned}
& + \left[ \langle \widetilde{\mathcal{K}}_i | H - E_V | \widetilde{\mathcal{J}}_i \rangle + \langle \widetilde{\mathcal{J}}_i | H - E_V | \widetilde{\mathcal{K}}_i \rangle + \right. \\
& + E_V \left( \langle \widetilde{\mathcal{K}}_i | \widetilde{\mathcal{J}}_i \rangle + \langle \widetilde{\mathcal{K}}_i | \widetilde{\mathcal{J}}_i \rangle \right) \left. \right] \mathcal{B}_{L_i L_j}^{\mathbf{k}} + \\
& \sum_L \mathcal{B}_{L L_i}^{\mathbf{k}} \left[ \langle \widetilde{\mathcal{J}}_i | H - E_V | \widetilde{\mathcal{J}}_i \rangle + E_V \langle \widetilde{\mathcal{J}}_i | \widetilde{\mathcal{J}}_i \rangle \right] \mathcal{B}_{L L_j}^{\mathbf{k}} \quad (4.68)
\end{aligned}$$

$$\begin{aligned}
\mathcal{O}_{ij}^{\mathbf{k}} & = \langle \widetilde{\mathcal{K}}_i | \widetilde{\mathcal{K}}_i \rangle \delta_{L_i L_j} + \left( \langle \widetilde{\mathcal{K}}_i | \widetilde{\mathcal{J}}_i \rangle + \langle \widetilde{\mathcal{K}}_j | \widetilde{\mathcal{J}}_j \rangle \right) \mathcal{B}_{L_i L_j}^{\mathbf{k}} + \\
& \sum_L \mathcal{B}_{L L_i}^{\mathbf{k}} \langle \widetilde{\mathcal{J}}_i | \widetilde{\mathcal{J}}_i \rangle \mathcal{B}_{L L_j}^{\mathbf{k}} \quad (4.69)
\end{aligned}$$

where

$$\widetilde{\mathcal{K}}_i(\mathbf{r}) = \frac{\mathcal{K}_i(\kappa S_{mt})}{\phi_{l_i}(\mathcal{D}(\mathcal{K}_i), S_{mt})} \phi_{l_i}(\mathcal{D}(\mathcal{K}_i), \mathbf{r}) \quad (4.70)$$

$$\widetilde{\mathcal{J}}_i(\kappa \mathbf{r}) = \frac{\mathcal{J}_i(\kappa S_{mt})}{\phi_{l_i}(\mathcal{D}(\mathcal{J}_i), S_{mt})} \phi_{l_i}(\mathcal{D}(\mathcal{J}_i), \mathbf{r}) \quad (4.71)$$

Now if the results of (4.41) and (4.42) are used together with the above approximations, the Hamiltonian and overlap matrix elements can be expressed as

$$\langle \widetilde{\mathcal{K}}_i | H - E_V | \widetilde{\mathcal{K}}_i \rangle = \left( \frac{\mathcal{K}_i(\kappa S_{mt})}{\phi_{l_i}(\mathcal{D}(\mathcal{K}_i), S_{mt})} \right)^2 \omega(\mathcal{D}(\mathcal{K}_i)) \quad (4.72)$$

$$\langle \widetilde{\mathcal{K}}_i | H - E_V | \widetilde{\mathcal{J}}_i \rangle = \frac{\mathcal{K}_i(\kappa S_{mt}) \mathcal{J}_i(\kappa S_{mt})}{\phi_{l_i}(\mathcal{D}(\mathcal{K}_i), S_{mt}) \phi_{l_i}(\mathcal{D}(\mathcal{J}_i), S_{mt})} \omega(\mathcal{D}(\mathcal{J}_i)) \quad (4.73)$$

$$\langle \widetilde{\mathcal{J}}_i | H - E_V | \widetilde{\mathcal{K}}_i \rangle = \frac{\mathcal{K}_i(\kappa S_{mt}) \mathcal{J}_i(\kappa S_{mt})}{\phi_{l_i}(\mathcal{D}(\mathcal{K}_i), S_{mt}) \phi_{l_i}(\mathcal{D}(\mathcal{J}_i), S_{mt})} \omega(\mathcal{D}(\mathcal{K}_i)) \quad (4.74)$$

$$\langle \widetilde{\mathcal{J}}_i | H - E_V | \widetilde{\mathcal{J}}_i \rangle = \left( \frac{\mathcal{J}_i(\kappa S_{mt})}{\phi_{l_i}(\mathcal{D}(\mathcal{J}_i), S_{mt})} \right)^2 \omega(\mathcal{D}(\mathcal{J}_i)) \quad (4.75)$$

$$\langle \widetilde{\mathcal{K}}_i | \widetilde{\mathcal{K}}_i \rangle = \left( \frac{\mathcal{K}_i(\kappa S_{mt})}{\phi_{l_i}(\mathcal{D}(\mathcal{K}_i), S_{mt})} \right)^2 (1 + \omega^2(\mathcal{D}(\mathcal{K}_i)) \langle \psi_{l_i} | \psi_{l_i} \rangle) \quad (4.76)$$

$$\begin{aligned}
\langle \widetilde{\mathcal{K}}_i | \widetilde{\mathcal{J}}_i \rangle & = \\
& \frac{\mathcal{K}_i(\kappa S_{mt}) \mathcal{J}_i(\kappa S_{mt})}{\phi_{l_i}(\mathcal{D}(\mathcal{K}_i), S_{mt}) \phi_{l_i}(\mathcal{D}(\mathcal{J}_i), S_{mt})} (1 + \omega(\mathcal{D}(\mathcal{K}_i)) \omega(\mathcal{D}(\mathcal{J}_i)) \langle \psi_{l_i} | \psi_{l_i} \rangle) \quad (4.77)
\end{aligned}$$

$$\langle \widetilde{\mathcal{J}}_i | \widetilde{\mathcal{J}}_i \rangle = \left( \frac{\mathcal{J}_i(\kappa S_{mt})}{\phi_{l_i}(\mathcal{D}(\mathcal{J}_i), S_{mt})} \right)^2 (1 + \omega^2(\mathcal{D}(\mathcal{J}_i)) \langle \psi_{l_i} | \psi_{l_i} \rangle) \quad (4.78)$$

From the above expressions, we see that the matrix elements of the LMTO-ASA secular equation are very easy to calculate. Apart from solving the secular equation (4.61) and calculating the density, the only parts of the problem

that cannot be done by hand are the calculations of the functions  $\psi_l$ ,  $\tilde{\psi}_l$  and the Hartree part of the potential, which demand numerical solutions of the radial Schrödinger equation and Poisons equation, respectively.

## 4.4 The pseudo potential method

Many material properties such as elasticity, lattice structure and phonons depend mainly on the chemical bonds between the atoms of the solid. The chemical bonding, on the other hand, is mainly described by the valence electrons of the material, whereas the core electron are more or less chemically inert and do not participate in the chemical bonding. Thus, when calculating material properties closely connected to chemical bonding, a natural approximation is to freeze the core states and solve the Kohn-Sham equations only for the valence, which is one of the main principles of the pseudo potential method.

To illustrate the basic principles of the pseudo potential method an outline of the Phillips-Kleinman method [18] is presented here. Let  $\psi_v$  and  $\psi_c$  be exact valence and core wave functions respectively. Then  $\psi_v$  and  $\psi_c$  are solutions to the Schrödinger equation

$$\mathcal{H} \psi_v = \varepsilon_v \psi_v, \quad \mathcal{H} \psi_c = \varepsilon_c \psi_c \quad (4.79)$$

where  $\varepsilon_v$  and  $\varepsilon_c$  are the respective eigenvalues of the valence and core wave-functions. Furthermore, let  $\tilde{\psi}_v$  be a wavefunction, for the moment undefined, such that the valence wavefunction can be expressed as

$$\psi_v = \tilde{\psi}_v + \sum_c a_c \psi_c \quad (4.80)$$

where  $a_c$  expansion coefficients are soon to be defined. Since the valence wavefunctions have to be orthogonal to the core states, i.e  $\langle \psi_v | \psi_c \rangle = 0$ , the expansion coefficients are determined by

$$a_c = -\langle \psi_c | \tilde{\psi}_v \rangle \quad (4.81)$$

and (4.80) can be rewritten as

$$\psi_v = \tilde{\psi}_v - \sum_c \langle \psi_c | \tilde{\psi}_v \rangle \psi_c. \quad (4.82)$$

This simply means that the valence wavefunction has been expressed as an auxiliary wave  $\tilde{\psi}_v$  minus the projection of  $\tilde{\psi}_v$  onto the core states.

Now inserting the expression (4.82) into the Schrödinger equation for the valence states gives

$$\begin{aligned} \mathcal{H} \tilde{\psi}_v - \sum_c \langle \psi_c | \tilde{\psi}_v \rangle \psi_c \varepsilon_c &= \varepsilon_v (\tilde{\psi}_v - \sum_c \langle \psi_c | \tilde{\psi}_v \rangle \psi_c) \Rightarrow \\ \left[ \mathcal{H} + \sum_c (\varepsilon_v - \varepsilon_c) |\psi_c\rangle \langle \psi_c| \right] \tilde{\psi}_v &= \varepsilon_v \tilde{\psi}_v \end{aligned} \quad (4.83)$$

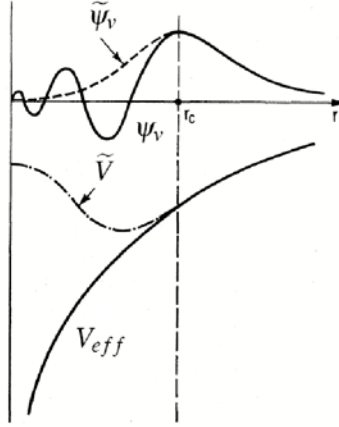


Figure 4.5: Schematic illustration of the pseudo potential  $\tilde{V}$  and the pseudo wavefunction  $\tilde{\psi}_v$ , shown in reference to the original all electron potential  $V_{eff}$  and corresponding wavefunction  $\psi_v$ [19].

Furthermore, if the original Hamiltonian is expressed as  $\mathcal{H} = -\frac{1}{2}\nabla^2 + V_{eff}$ , then the above equation can be recast into

$$\left[ -\frac{1}{2}\nabla^2 + \tilde{V} \right] \tilde{\psi}_v = \epsilon_v \tilde{\psi}_v \quad (4.84)$$

where

$$\tilde{V} = V_{eff} + \sum_c (\epsilon_v - \epsilon_c) |\psi_c\rangle \langle \psi_c| \quad (4.85)$$

The new auxiliary potential  $\tilde{V}$  is what is called a pseudo potential, and the solutions  $\tilde{\psi}_v$  of the corresponding Schrödinger equation (4.84) are called pseudo wavefunctions.

Since the pseudo potential  $\tilde{V}$  is much softer (not as deep) than the original potential  $V_{eff}$ , close to the atomic nuclei the pseudo wave functions will not oscillate as rapidly as the true valence wavefunctions. This smoother behaviour of the pseudo waves makes it possible to expand  $\tilde{\psi}_v$  with only a few wavefunctions of some suitable basis, preferable plane waves, making the pseudo potential method much less computationally demanding than other electronic structure methods.

In Fig. 4.5 a schematic illustration of the pseudo potential and the pseudo wavefunction are given in reference to the original all electron potential and corresponding wavefunction. Here inside some core radius  $r_c$  the pseudo potential  $\tilde{V}$  is much softer than the original potential  $V_{eff}$ . Outside the core region ( $r > r_c$ ), as the core wavefunctions  $\psi_c$  vanish, the pseudo potential coincides with the potential  $V_{eff}$  ensuring that a correct valence charge density is obtained. Furthermore, inside the core region the rapid oscillations of the

true valence wavefunction are absent in the pseudo wavefunction  $\tilde{\psi}_v$ , whereas  $\tilde{\psi}_v = \psi_v$  outside the core region.

In practice the Phillips-Kleinman pseudo potential method is not used due to numerical difficulties. Nevertheless the main ideas and principles of practically used pseudo potentials, such as the Vanderbilt's approach [20], are the same. To emphasize the desired properties of a pseudo potential, the potential should be as soft as possible, transferable and produce pseudo wave functions with valence charge density as close as possible to the true valence charge density.

## 4.5 Projector augmented wave method

The projector augmented wave method [21] (PAW), similarly to the pseudo potential method, is based on a transformation of the Schrödinger equation into a much less computationally demanding problem. However the PAW method is not a traditional pseudo potential method in which only the valence wavefunctions are mapped onto a more manageable set of wavefunctions. The PAW method also maps the core states onto more manageable wavefunctions, making it an all electron method.

The central ingredient of the PAW method is a linear transformation  $\tau$  which relates the exact  $\Psi_n$  valence wavefunctions to an auxiliary wavefunction  $\tilde{\Psi}_n$  much like the pseudo wavefunctions of the pseudo potential method

$$|\Psi_n\rangle = \tau|\tilde{\Psi}_n\rangle. \quad (4.86)$$

Here  $n$  is a composite quantum number for the band, k-point and spin. From the above transformation the Schrödinger equation of the auxiliary waves becomes

$$\tau^\dagger \mathcal{H} \tau |\tilde{\Psi}_n\rangle = \varepsilon_n \tau^\dagger \tau |\tilde{\Psi}_n\rangle \quad (4.87)$$

The linear transformation  $\tau$  differs only from unity by a sum of local, atom centered contributions  $\tau_{\mathbf{R}}$ , i.e

$$\tau = 1 + \sum_{\mathbf{R}} \tau_{\mathbf{R}}, \quad (4.88)$$

where each contribution  $\tau_{\mathbf{R}}$  acts only within some augmentation region  $\Omega_{\mathbf{R}}$  surrounding an atom centered at  $\mathbf{R}$ .

In order to define the operator  $\tau_{\mathbf{R}}$  let  $\phi_i$  be a solution of the Schrödinger equation of an isolated atom centered at  $\mathbf{R}$ . Furthermore let  $\tilde{\phi}_i$  be the solution of the Schrödinger equation with the effective one atom potential replaced by a pseudo potential. The pseudo potential is such that  $\tilde{\phi}_i$  is much smoother than  $\phi_i$  inside the augmentation region  $\Omega_{\mathbf{R}}$ , but outside this region  $\tilde{\phi}_i = \phi_i$ . Now the operator  $\tau_{\mathbf{R}}$  is defined in such a way that

$$|\phi_i\rangle = (1 + \tau_{\mathbf{R}})|\tilde{\phi}_i\rangle, \quad \mathbf{r} \in \Omega_{\mathbf{R}}, \quad (4.89)$$

where  $\mathbf{r}$  is the spatial argument of the waves  $\phi_i$  and  $\tilde{\phi}_i$ . Inside the augmentation region the auxiliary waves  $\tilde{\Psi}_n$  are expanded in terms of the wavefunctions  $\tilde{\phi}_i$

$$|\tilde{\Psi}_n\rangle = \sum_i b_i |\tilde{\phi}_i\rangle, \quad \mathbf{r} \in \Omega_{\mathbf{R}}. \quad (4.90)$$

Furthermore, since  $|\phi_i\rangle = \tau|\tilde{\phi}_i\rangle$  the following relation

$$|\Psi_n\rangle = \tau|\tilde{\Psi}_n\rangle = \sum_i b_i |\phi_i\rangle, \quad \mathbf{r} \in \Omega_{\mathbf{R}} \quad (4.91)$$

is also valid. Hence from Eq. (4.90,4.91) it is evident that

$$|\Psi_n\rangle = |\tilde{\Psi}_n\rangle + \sum_i b_i(|\phi_i\rangle - |\tilde{\phi}_i\rangle) \quad (4.92)$$

Since the transformation  $\tau$  is required to be linear the expansion coefficients  $b_i$  must be scalar products

$$b_i = \langle \tilde{p}_i | \tilde{\Psi}_n \rangle \quad (4.93)$$

of the auxiliary wavefunction and some projection operator  $\langle \tilde{p}_i |$ . These projection operators must fulfill the completeness condition

$$\sum_i |\tilde{\phi}_i\rangle \langle \tilde{p}_i| = 1, \quad \mathbf{r} \in \Omega_{\mathbf{R}} \quad (4.94)$$

and the orthonormality condition

$$\langle \tilde{p}_i | \tilde{\phi}_j \rangle = \delta_{ij} \quad (4.95)$$

to ensure that the expansion (4.90) is possible. Finally, from (4.92) and (4.93) the linear relation between the true wavefunction and the auxiliary wavefunction becomes

$$|\Psi_n\rangle = \left[ 1 + \sum_i [|\phi_i\rangle - |\tilde{\phi}_i\rangle] \langle \tilde{p}_i| \right] |\tilde{\Psi}_n\rangle, \quad (4.96)$$

from which the linear transformation operator  $\tau$  can be identified

$$\tau = 1 + \sum_i [|\phi_i\rangle - |\tilde{\phi}_i\rangle] \langle \tilde{p}_i|. \quad (4.97)$$

The decomposition of the core states  $\Psi^c$  and their connection to auxiliary core states  $\tilde{\Psi}^c$  is similar to the decomposition of the valence states and it is given by

$$|\Psi^c\rangle = |\tilde{\Psi}^c\rangle + |\phi^c\rangle - |\tilde{\phi}^c\rangle. \quad (4.98)$$

Here  $\phi^c$  are the core solutions of the Schrödinger equation of an isolated atom centered at  $\mathbf{R}$ , and  $\tilde{\phi}^c$  the solutions of the Schrödinger equation with the effective potential replaced by the same pseudo potential as was used in the calculation of  $\tilde{\phi}_i$ .

The details involved in how the operators  $\langle \tilde{p}_i |$  are constructed and how the pseudo potential used for calculating  $\tilde{\phi}_i$  and  $\tilde{\phi}_i^c$  is chosen, will not be discussed here, the interested reader can turn to the original paper by Blöchl [21].

## 4.6 The self-consistent loop

Since the Kohn-Sham potential depends on the charge density of the solutions that is sought for, the Kohn-Sham equations have to be solved in a self-consistent manner. In this section we will discuss the typical steps that a DFT calculation has to go through before the solution of the Kohn-Sham equations can be obtained.

1. The first step of the calculation is to create a start guess for the charge density. This density is typically taken from an atomic calculation.
2. From the density the Kohn-Sham potential is calculated. This involves solving the Poisson equation to obtain the Hartree part of the potential and calculating the exchange and correlation part of the potential. To obtain the Kohn-Sham potential these two contributions are then added to the external ionic potential.
3. With the new potential the Kohn-Sham equations are solved with some band structure method (KKR-ASA, LMTO-ASA, FP-LMTO,...) for every k-point in the irreducible Brillouin zone.
4. A new charge density is obtained by summing up the charge density contributions from all the k-points up to the Fermi energy, i.e.

$$\rho(\mathbf{r}) = V_0 \sum_{\sigma} \sum_n \int \frac{d\mathbf{k}}{(2\pi)^3} \Theta(\varepsilon_f - \varepsilon_n^{\sigma}(\mathbf{k})) |\psi_{\mathbf{k}n}^{\sigma}(\mathbf{r})|^2 \quad (4.99)$$

Where  $\sigma$  and  $n$  are the spin and the band index respectively.

5. If the difference between the total energies of two consecutive solutions of the Kohn-Sham equations are smaller than the required energy resolution the calculation is terminated, and the last solution is regarded as the ground state solution. Otherwise the calculation continues using the last calculated density in step 2.



## 5. Chemical bonding

In this chapter one of the methods used in analyzing the chemical bonding in  $\text{MgB}_2$  will be briefly discussed together with some of the results obtained with this method.

### 5.0.1 The balanced crystal overlap occupation population (BCOOP)

In this section the tool used to analyse the chemical bonding character in  $\text{MgB}_2$  (Paper I) will be briefly discussed. This tool goes under the name of the balanced crystal overlap occupation population, and it has been developed by Grechnev et al [22] to determine the character of the chemical bonding in a solid. Basically the BCOOP is an overlap weighted density of states, and it is defined by

$$BCOOP_{ij} = \sum_n \int_{BZ} \frac{d\mathbf{k}}{(2\pi)^3} \delta(\varepsilon - \varepsilon_n(\mathbf{k})) \frac{\mathcal{A}_i(\mathbf{k}) \mathcal{A}_j(\mathbf{k}) \mathcal{O}_{i,j}(\boldsymbol{\kappa}, \mathbf{k})}{\sum_{\alpha} \sum_{i',j' \in B(\alpha)} \mathcal{A}_{i'}(\mathbf{k}) \mathcal{A}_{j'}(\mathbf{k}) \mathcal{O}_{i',j'}(\boldsymbol{\kappa}, \mathbf{k})}, \quad (5.1)$$

where

$$\mathcal{O}_{i,j}(\boldsymbol{\kappa}, \mathbf{k}) = \langle \chi_i^{\mathbf{k}}(E_v, \boldsymbol{\kappa}, \mathbf{r}) | \chi_j^{\mathbf{k}}(E_v, \boldsymbol{\kappa}, \mathbf{r}) \rangle \quad (5.2)$$

is the overlap matrix between the basis functions  $\chi_i^{\mathbf{k}}(E_v, \boldsymbol{\kappa}, \mathbf{r})$  used to expand the eigenfunction

$$\phi_{\mathbf{k}n}(\mathbf{r}) = \sum_i \mathcal{A}_i(\mathbf{k}) \chi_i^{\mathbf{k}}(E_v, \boldsymbol{\kappa}, \mathbf{r}) \quad (5.3)$$

corresponding to the eigenvalue  $\varepsilon_n(\mathbf{k})$ . Since the BCOOP has been implemented within the FP-LMTO formalism the basis functions  $\chi_i^{\mathbf{k}}(E_v, \boldsymbol{\kappa}, \mathbf{r})$  are equivalent to Bloch sums of LMTOs. Furthermore the indexes appearing in (5.1) are defined by

$$\begin{aligned} i &\equiv (t, L, \boldsymbol{\kappa}, e) = (t, l, m, \boldsymbol{\kappa}, e) \\ \alpha &\equiv (t, l) \\ B(\alpha) &= B(t, l) \equiv \{i \mid l_i = l, \quad t_i = t\}, \end{aligned} \quad (5.4)$$

where  $t, e$  denote atom type and energy basis set, respectively. It should be stressed that since the overlap integral  $\mathcal{O}_{ij}(\mathbf{k})$  is that of Bloch functions the BCOOP only defines bonding between types of atoms and not between individual atoms.

## 5.0.2 Interpretation of the BCOOP from the LCAO perspective

To understand how the measure of BCOOP distinguishes between different bonding types one may turn to the LCAO description of a s-valent dimer. Let the two atoms of the dimer be denoted 1 and 2, and let their corresponding atomic orbitals be defined as the solutions to the Schrödinger equations

$$\left[ -\frac{1}{2}\nabla^2 + V_1 \right] \psi_1 = E_1 \psi_1 \quad (5.5)$$

$$\left[ -\frac{1}{2}\nabla^2 + V_2 \right] \psi_2 = E_2 \psi_2 \quad (5.6)$$

The LCAO trial function thus becomes

$$\phi = \mathcal{A}_1 \psi_1 + \mathcal{A}_2 \psi_2 \quad (5.7)$$

Using the above trial function in a standard variational procedure, ignoring the crystal field terms, leads to the linear equations

$$\begin{pmatrix} -\frac{1}{2}\Delta E - (E - \bar{E}) & h - (E - \bar{E})\mathcal{O} \\ h - (E - \bar{E})\mathcal{O} & \frac{1}{2}\Delta E - (E - \bar{E}) \end{pmatrix} \begin{pmatrix} \mathcal{A}_1 \\ \mathcal{A}_2 \end{pmatrix} = 0 \quad (5.8)$$

where

$$\mathcal{O} = \langle \psi_1 | \psi_2 \rangle \quad (5.9)$$

$$h = \langle \psi_1 | \frac{V_1 + V_2}{2} | \psi_2 \rangle \quad (5.10)$$

$$\bar{E} = \frac{1}{2}(E_1 + E_2) \quad (5.11)$$

$$\Delta E = E_1 - E_2 \quad (5.12)$$

By demanding that the determinant of the matrix in (5.8) is equal to zero, the non-trivial solutions to (5.8) are found to be

$$\mathcal{A}_b = \begin{pmatrix} \mathcal{A}_1 \\ \mathcal{A}_2 \end{pmatrix} = \frac{1}{\sqrt{2(1 - \mathcal{O}^2)}} \left( \begin{pmatrix} \left[ 1 - \frac{\mathcal{O} - \delta(1 - \mathcal{O}^2)}{\sqrt{1 + (1 - \mathcal{O}^2)\delta^2}} \right]^{\frac{1}{2}} \\ \left[ 1 - \frac{\mathcal{O} + \delta}{\sqrt{1 + (1 - \mathcal{O}^2)\delta^2}} \right]^{\frac{1}{2}} \end{pmatrix} \right)$$

$$E_b = \frac{1}{1 - \mathcal{O}^2} \left[ h\mathcal{O} - \sqrt{h^2 + (1 - \mathcal{O}^2) \left( \frac{\Delta E}{2} \right)^2} \right] \quad (5.13)$$

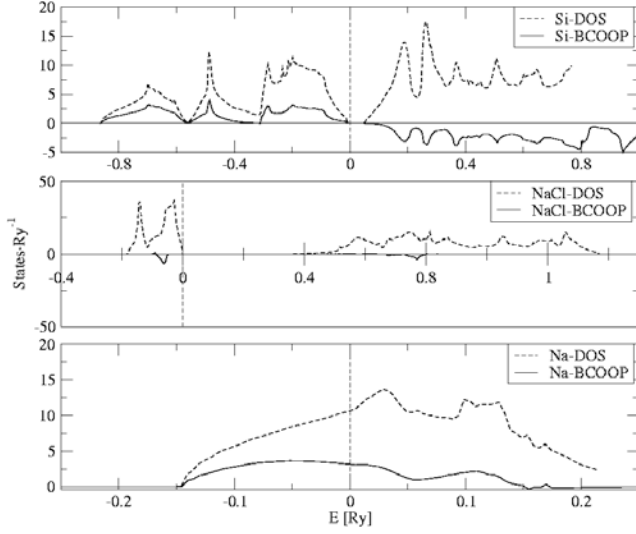


Figure 5.1: Three typical BCOOPs. Top panel BCOOP of Si-Si covalent bond, middle panel BCOOP of ionic Na-Cl bond and low panel BCOOP of Na-Na metallic bond.

$$\mathcal{A}_a = \begin{pmatrix} \mathcal{A}_1 \\ \mathcal{A}_2 \end{pmatrix} = \frac{1}{\sqrt{2(1-\varrho^2)}} \begin{pmatrix} - \left[ 1 + \frac{\varrho - \delta(1-\varrho^2)}{\sqrt{1+(1-\varrho^2)\delta^2}} \right]^{\frac{1}{2}} \\ \left[ 1 + \frac{\varrho + \delta}{\sqrt{1+(1-\varrho^2)\delta^2}} \right]^{\frac{1}{2}} \end{pmatrix}$$

$$E_a = \frac{1}{1-\varrho^2} \left[ h\varrho + \sqrt{h^2 + (1-\varrho^2) \left( \frac{\Delta E}{2} \right)^2} \right] \quad (5.14)$$

where

$$\delta = \frac{\Delta E}{2|h|} \quad (5.15)$$

Now the above solutions can be used to predict the features that the BCOOP will display when the bonding between the atom types in the solid are covalent or ionic.

1. The typical case of a covalent bond is that of a homo nuclear dimer. In this case  $\delta = 0$  and from (5.13) we have that in the bonding case

$$\varrho \mathcal{A}_1 \mathcal{A}_2 = \frac{\varrho}{2(1+\varrho)} \quad (5.16)$$

and in the anti-bonding case (5.14) gives that

$$\varrho \mathcal{A}_1 \mathcal{A}_2 = -\frac{\varrho}{2(1-\varrho)} \quad (5.17)$$

Furthermore we have both for the bonding and anti-bonding case that

$$|\mathcal{A}_1|^2 + |\mathcal{A}_2|^2 + \mathcal{A}_1^* \mathcal{A}_2 + \mathcal{A}_2^* \mathcal{A}_1 = 1 \quad (5.18)$$

If we compare (5.16), (5.17) and (5.18) with (5.1) we see that the BCOOP will be positive for bonding states and negative for anti-bonding states. Furthermore bonding the strength of the state will correlate with the amplitude of the BCOOP. In the top panel of (Fig. 5.1) the BCOOP of Si displays the typical features of a covalent bond.

2. The typical example of an ionic bond is that of a hetro nuclear dimer, having the property  $\delta \gg 1 > \mathcal{O}$ . From (5.13) we have that for the bonding case

$$\mathcal{A}_1 \approx \frac{1}{\sqrt{2}} \left[ 1 + \frac{\delta}{\sqrt{1+\delta^2}} \right]^{\frac{1}{2}} \approx 1 ; \quad \mathcal{A}_2 \approx \frac{1}{\sqrt{2}} \left[ 1 - \frac{\delta}{\sqrt{1+\delta^2}} \right]^{\frac{1}{2}} \approx 0 \quad (5.19)$$

and similarly for the anti-bonding case

$$\mathcal{A}_1 \approx -\frac{1}{\sqrt{2}} \left[ 1 - \frac{\delta}{\sqrt{1+\delta^2}} \right]^{\frac{1}{2}} \approx 0 ; \quad \mathcal{A}_2 \approx \frac{1}{\sqrt{2}} \left[ 1 + \frac{\delta}{\sqrt{1+\delta^2}} \right]^{\frac{1}{2}} \approx 1 \quad (5.20)$$

Thus in the case of ionic bonding we have that

$$\mathcal{O} \mathcal{A}_1 \mathcal{A}_2 \approx 0 \quad (5.21)$$

Comparing (5.21) with (5.1) it becomes obvious that the pure ionic bond will have zero BCOOP amplitude. However, in practice there is no such thing as pure ionic bonds in the sense that is discussed above. Therefore the ionic bond will be characterized by both zero and non-zero BCOOP amplitudes [23]. In the middle panel of (Fig. 5.1) the BCOOP of NaCl displays the typical features of an ionic bond between Na and Cl.

3. The typical sp-metallic bond can not be investigated from the LCAO perspective. However the typical sp-metal is characterized by almost free electron behavior. Thus the wave functions (5.3) are described by plane waves. Now if we replace the expression (5.3), with an expansion of localized orbitals, we have for the typical sp-valent metal

$$\frac{1}{\sqrt{V}} e^{i\mathbf{k}\mathbf{r}} = \sum_n \mathcal{A}_n(\mathbf{k}) \chi_n(\mathbf{r}), \quad (5.22)$$

where  $V$  is the volume of the crystal, and

$$\chi_n(\mathbf{r}) \equiv \chi(\mathbf{r} - \mathbf{R}_n). \quad (5.23)$$

Multiplying equation (5.22) by its complex conjugate one obtains

$$\frac{1}{V} = \sum_n \sum_m \mathcal{A}_n(\mathbf{k}) \mathcal{A}_m^*(\mathbf{k}) \chi_n(\mathbf{r}) \chi_m^*(\mathbf{r}). \quad (5.24)$$

Evaluating the right hand side of (5.24) for two different  $\mathbf{k}$ -vectors,  $\mathbf{k}$  and  $\mathbf{k}'$ , and subtracting the results with each other, the following relation is revealed

$$0 = \sum_n \sum_m \chi_n(\mathbf{r}) \chi_m^*(\mathbf{r}) [\mathcal{A}_n(\mathbf{k}) \mathcal{A}_m^*(\mathbf{k}) - \mathcal{A}_n(\mathbf{k}') \mathcal{A}_m^*(\mathbf{k}')]. \quad (5.25)$$

Since the above relation must be valid for all possible  $\mathbf{r}$ , relation (5.25) implies

$$\mathcal{A}_n(\mathbf{k}) \mathcal{A}_m^*(\mathbf{k}) = \text{Constant}, \quad (5.26)$$

and that

$$\mathcal{A}_n^*(\mathbf{k}) \mathcal{A}_m(\mathbf{k}) \mathcal{O}_{m,n} = \text{Const}, \quad (5.27)$$

where

$$\mathcal{O}_{m,n} = \langle \chi_m(\mathbf{r}) | \chi_n(\mathbf{r}) \rangle. \quad (5.28)$$

Thus, the BCOOP in the case of sp-metallic bonding will be more or less proportional to the density of states. In the lower panel of (Fig. 5.1) the BCOOP of Na displays the typical features of a sp-metallic bond.

### 5.0.3 Chemical bonding in $\text{MgB}_2$

In this section the results of analyzing the chemical bond in  $\text{MgB}_2$  with the help of the charge density, the electronic structure and the BCOOP will be discussed. The charge density and the BCOOP between nearest neighbours have been calculated in three different planes (Fig. 5.2) of the  $\text{MgB}_2$  crystal.

In the middle panel of Figure 5.3 the BCOOP between the boron atoms has been calculated, displaying the typical features of a covalent bond. The BCOOP between Mg and B, displayed in the upper panel of Figure 5.3, with its predominantly negative amplitude and small positive amplitude suggests that the bonding between these atoms has a strong ionic character. This conclusion has been quantified by calculating the difference between the number of electrons inside the Mg muffin tins of pure magnesium and of  $\text{MgB}_2$ . This estimate shows that around 0.5 electrons leave the vicinity of the Mg atoms when we go from metallic Mg to the compound  $\text{MgB}_2$ .

Finally, since the BCOOP between the Mg atoms, displayed in the lower panel of Figure 5.3, does not exactly correlate with the corresponding partial density of states in Fig. 5.4 we can not conclude that the Mg-Mg bond is purely metallic. Due to the anti-bonding character of the states above 0.4 Ry (Fig. 5.3), this bond is better classified as being a mixture between metallic and covalent.

In Figure 5.5 the charge density in the boron plane is displayed. Here the high concentration of charge between the atoms, indicates a bond of strong

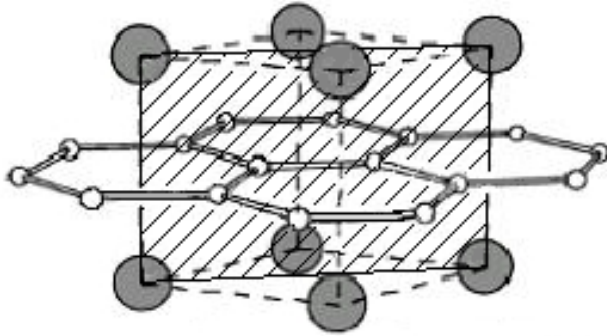


*Figure 5.2:* The crystal structure of MgB<sub>2</sub>. The shaded plane, orthogonal to both the magnesium layer (grey circles) and the boron layer (white circles), corresponds to the section in which the charge density of Figure 5.6 has been calculated.

covalent character, thus supporting the conclusions made by the BCOOP analysis.

The charge density in the magnesium boron plane (Figure 5.6) indicates a strong covalent bond between the B atoms, but no such features are shown between the Mg and B atoms, ruling out a covalent bond between Mg and B.

Finally, the charge density of MgB<sub>2</sub> in the Mg layer, displayed in Figure 5.7, show a more or less featureless charge distribution, suggesting a bonding of metallic character between these atoms.

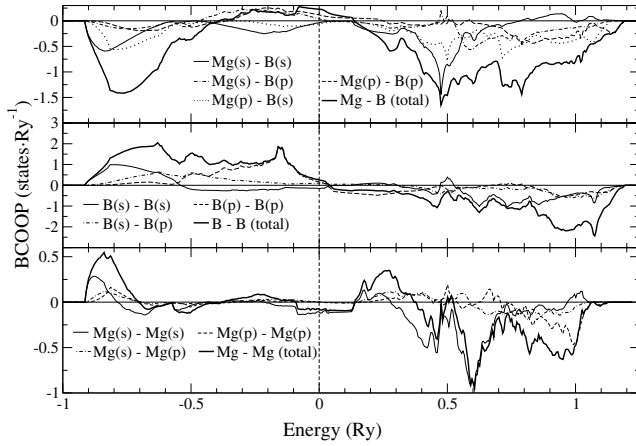


Figure 5.3: The BCOOP between magnesium and boron, the BCOOP between boron and boron and the BCOOP between magnesium and magnesium, in  $\text{MgB}_2$ . The Fermi level is at zero energy.

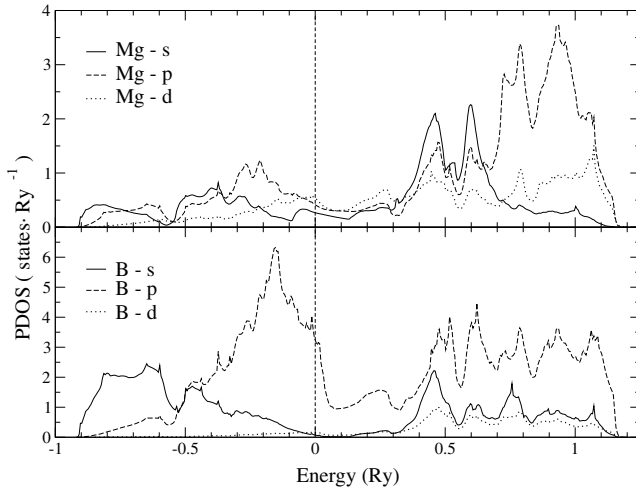


Figure 5.4: The partial density of states for magnesium and boron, in  $\text{MgB}_2$ . The Fermi level is at zero energy.

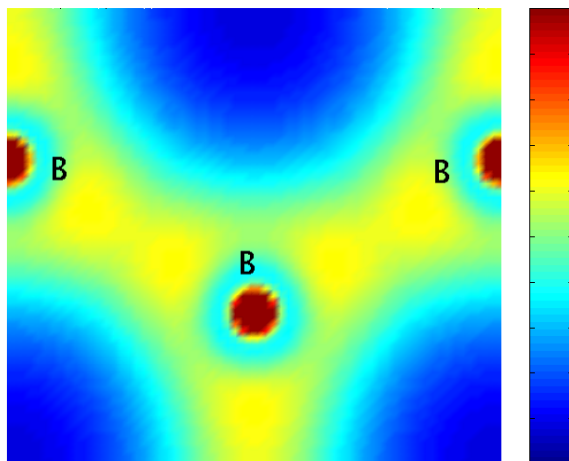


Figure 5.5: The charge density for the boron layer, in  $\text{MgB}_2$ . The charge density scale goes from dark blue (low density) to dark red (high density).

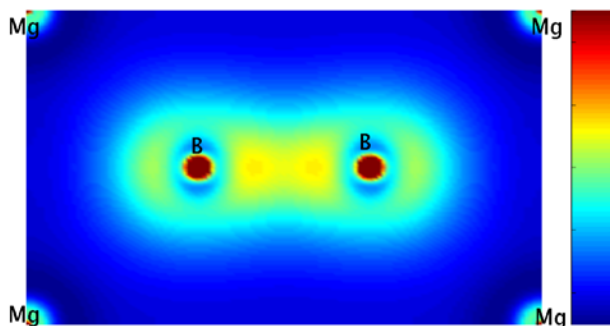
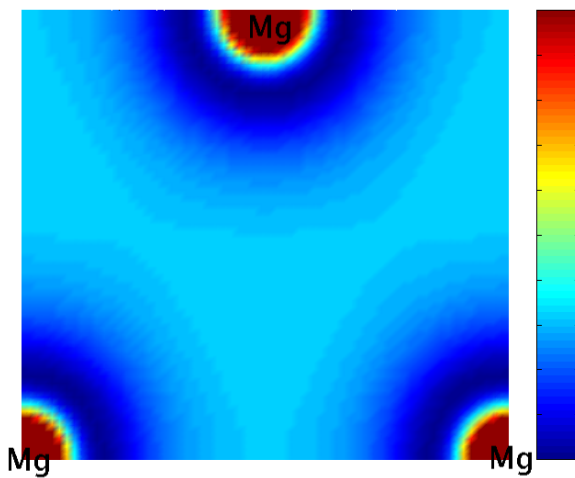


Figure 5.6: The charge density for the section through both magnesium and boron atoms (the shaded plane of Fig. 5.2), in  $\text{MgB}_2$ . The charge density scale goes from dark blue (low density) to dark red (high density).



*Figure 5.7:* The charge density for the magnesium layer, in  $\text{MgB}_2$ . The charge density scale goes from dark blue (low density) to dark red (high density).



## 6. Theory of elasticity

### 6.1 The strain tensor

Since the theory of elasticity describes how deviations from the equilibrium shape of a body effects the stress and energy of the body, the first step in developing this theory is to find a way to describe such deviations. To do this let  $\mathbf{X}$  be the coordinates describing the equilibrium positions of the particles of the body. Furthermore let  $\mathbf{x}$  be the coordinates of the particles after a distortion has been applied to the body. Now the displacement field  $\mathbf{U}$  is defined as the mapping that relates the equilibrium coordinates with the corresponding coordinates of the distorted body

$$\mathbf{x} = \mathbf{X} + \mathbf{U}(\mathbf{X}) = (X_1 + U_1(\mathbf{X}), X_2 + U_2(\mathbf{X}), X_3 + U_3(\mathbf{X})) \quad (6.1)$$

Now let  $d\mathbf{X}$  and  $d\mathbf{x}$  be length elements of the equilibrium and the distorted body, respectively. In figure 6.1 the geometric interpretation of the effect the displacement field has on the length segment  $dX$  has been depicted. From this figure it is easy to find that the distorted length segment  $d\mathbf{x}$  is related to the undistorted segment  $d\mathbf{X}$  in the following way

$$\begin{aligned} d\mathbf{x} &= \mathbf{X} + d\mathbf{X} + \mathbf{U}(\mathbf{X} + d\mathbf{X}) - \mathbf{X} - \mathbf{U}(\mathbf{X}) = \\ &= \mathbf{U}(\mathbf{X} + d\mathbf{X}) - \mathbf{U}(\mathbf{X}) + d\mathbf{X} = [\nabla\mathbf{U} + \mathbf{1}] d\mathbf{X} + \mathcal{O}(|d\mathbf{X}|^2) \end{aligned} \quad (6.2)$$

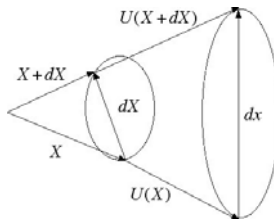


Figure 6.1: The effect of a distortion field  $U(\mathbf{X})$  has on a length element  $d\mathbf{X}$

where

$$\nabla\mathbf{U} = \begin{pmatrix} \frac{\partial U_1}{\partial X_1} & \frac{\partial U_1}{\partial X_2} & \frac{\partial U_1}{\partial X_3} \\ \frac{\partial U_2}{\partial X_1} & \frac{\partial U_2}{\partial X_2} & \frac{\partial U_2}{\partial X_3} \\ \frac{\partial U_3}{\partial X_1} & \frac{\partial U_3}{\partial X_2} & \frac{\partial U_3}{\partial X_3} \end{pmatrix} \quad (6.3)$$

Now if the displacements are assumed to be small  $\|\nabla\mathbf{U}\| \ll 1$ , the relation (6.2) implies that

$$d\mathbf{x} \approx \bar{\bar{F}} d\mathbf{X} \quad (6.4)$$

where

$$\bar{\bar{F}} \equiv 1 + \nabla\mathbf{U} \quad (6.5)$$

is the strain tensor. Furthermore if we define the distortion matrix

$$\bar{\bar{\epsilon}} \equiv \frac{1}{2} [\nabla\mathbf{U} + \nabla\mathbf{U}^T] \quad (6.6)$$

we have for small distortions

$$\bar{\bar{F}}^T \bar{\bar{F}} = 1 + 2\bar{\bar{\epsilon}} + \mathcal{O}(\|\nabla\mathbf{U}\|^2) \approx 1 + 2\bar{\bar{\epsilon}} \quad (6.7)$$

$$(1 + \bar{\bar{\epsilon}}^T)(1 + \bar{\bar{\epsilon}}) = 1 + 2\bar{\bar{\epsilon}} + \mathcal{O}(\|\bar{\bar{\epsilon}}\|^2) \approx 1 + 2\bar{\bar{\epsilon}} \quad (6.8)$$

Thus, in the case of small distortions it is evident from the above relations that when the strain tensor appears to second order

$$\bar{\bar{F}} \approx 1 + \bar{\bar{\epsilon}}. \quad (6.9)$$

From now on when we speak of the strain tensor it will always be assumed that the distortions are small, and that the approximation stated in (6.9) defines the strain tensor. This will turn out to be a good approximation, since later on it will be shown that the effects that the distortion matrix has on the total energy of a system are second order.

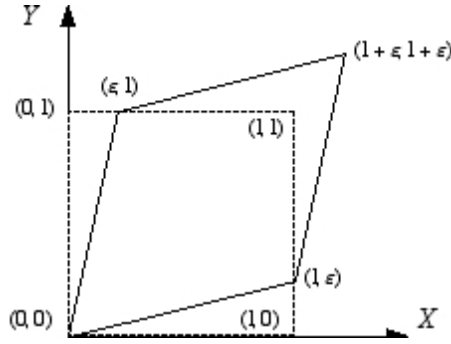


Figure 6.2: The two dimensional square lattice, before (dashed line) and after (full drawn line) the strain (6.10) has been applied

An example of the effect a distortion has on a lattice is the typical shear strain

$$\bar{\mathbf{F}} = \begin{pmatrix} 1 & \varepsilon & 0 \\ \varepsilon & 1 & 0 \\ 0 & 0 & 1 \end{pmatrix} \quad (6.10)$$

applied to the two dimensional square lattice depicted in figure 6.2. Using the transformation (6.4) on the corner coordinates of the square, it becomes obvious that the distorted square takes on the form of the parallelogram shown in figure 6.2

## 6.2 The elastic constants

Let us start this section by Taylor expanding the potential energy of a unit cell around  $\bar{\varepsilon} = 0$

$$E[\bar{\varepsilon}, V] = E[0, V_0] + \sum_{i,j} \left( \frac{\partial E}{\partial \varepsilon_{ij}} \right)_{\bar{\varepsilon}=0} \varepsilon_{ij} + \frac{1}{2} \sum_{i,j,k,k} \left( \frac{\partial^2 E}{\partial \varepsilon_{ij} \varepsilon_{kl}} \right)_{\bar{\varepsilon}=0} \varepsilon_{ij} \varepsilon_{kl} + \mathcal{O}(\|\bar{\varepsilon}\|^3) \quad (6.11)$$

Now in analogy with Hooke's law, the second order partial derivative in (6.11) is used to define the elastic constants

$$C_{ijkl} \equiv \frac{1}{V_0} \left( \frac{\partial^2 E}{\partial \varepsilon_{ij} \varepsilon_{kl}} \right)_{\bar{\varepsilon}=0} \quad (6.12)$$

and the first order partial derivative in (6.11) is used to define the stress tensor

$$T_{ij} \equiv \frac{1}{V_0} \left( \frac{\partial E}{\partial \varepsilon_{ij}} \right)_{\bar{\varepsilon}=0} \quad (6.13)$$

Furthermore if the so-called voigt notation for the indexes defined by

$$\begin{aligned} xx &\leftrightarrow 1 & ; & \quad yy \leftrightarrow 2 & \quad ; & \quad zz \leftrightarrow 3 \\ yz &\leftrightarrow 4 & ; & \quad xz \leftrightarrow 5 & \quad ; & \quad xy \leftrightarrow 6 \end{aligned} \quad (6.14)$$

is introduced, the elastic tensor (6.12), stress tensor (6.13) and distortion matrix (6.6) are reduced to 6x6, 6x1 and 6x1 matrices respectively, and the Taylor expansion (6.11) can be rewritten as

$$E[\bar{\boldsymbol{\varepsilon}}, V] = E[0, V_0] + V_0 \sum_i T_i \delta_i \varepsilon_i + \frac{V_0}{2} \sum_{i,j} C_{ij} \delta_i \delta_j \varepsilon_i \varepsilon_j + \mathcal{O}(|\boldsymbol{\varepsilon}|^3) \quad (6.15)$$

where

$$\delta_i = \begin{cases} 1, & i \leq 3 \\ 2, & i > 3 \end{cases} \quad (6.16)$$

### 6.3 Calculations of elastic constants

As was seen in the previous section the elastic behavior of a solid is to a great extent determined by the elastic constants (6.12). At first glance there seems to exist a maximum of 6x6=36 linearly independent constants, but due to the symmetry

$$C_{ijkl} = C_{klij} \quad (6.17)$$

induced by the symmetry of the second order derivative in the definition of these constants, the maximum number of independent constants reduce to 21. This number however is further reduced by the point group symmetry of the structure [24]. For instance the cubic lattices with their 48 point group symmetry operations only have 3 independent elastic constants, whereas the hexagonal structures with their 24 point group symmetry operations have 5 independent constants.

To calculate the elastic constants from first principles, one first has to select a set of linearly independent distortions. Then for each of these distortions the total energy is calculated for a number of different distortion amplitudes, producing an energy parabola for each distortion. Since the potential energy (6.15) for each distortion can be expressed as a linear combination of elastic constants multiplied with the square of the distortion amplitude, the curvatures of the different energy parabola together with their corresponding linear combination of elastic constants produce a set of linear equations. In solving these equations the elastic constants are finally extracted. Furthermore since the distortions often are applied around the equilibrium of the lattice the first summation in (6.15) is equal to zero.

### 6.3.1 The strain matrices of a hexagonal lattice

In this subsection the strain matrices used in extracting the hexagonal elastic constants will be presented together with their respective energy expressions. The 5 linearly independent constants are

$$C_{11} \ ; \ C_{12} \ ; \ C_{13} \ ; \ C_{33} \ ; \ C_{55}. \quad (6.18)$$

The first strain is symmetry conserving but not volume conserving and it is given by

$$\bar{\bar{F}} = \begin{pmatrix} 1 + \varepsilon & 0 & 0 \\ 0 & 1 + \varepsilon & 0 \\ 0 & 0 & 1 + \varepsilon \end{pmatrix}, \quad (6.19)$$

where the corresponding energy expression is

$$E[\varepsilon, V] = E[0, V_0] + \frac{V_0}{2} [2(C_{11} + C_{12}) + 4C_{13} + C_{33}] \varepsilon^2. \quad (6.20)$$

The second strain is both symmetry and volume conserving and it is given by

$$\bar{\bar{F}} = \begin{pmatrix} (1 + \varepsilon)^{-\frac{1}{3}} & 0 & 0 \\ 0 & (1 + \varepsilon)^{-\frac{1}{3}} & 0 \\ 0 & 0 & (1 + \varepsilon)^{\frac{2}{3}} \end{pmatrix}, \quad (6.21)$$

where the corresponding energy expression is

$$E[\varepsilon, V] = E[0, V_0] + \frac{V_0}{9} [C_{11} + C_{12} - 4C_{13} + 2C_{33}] \varepsilon^2. \quad (6.22)$$

The third strain is volume conserving but not symmetry conserving and it is given by

$$\bar{\bar{F}} = \begin{pmatrix} \frac{1 + \varepsilon}{(1 - \varepsilon^2)^{\frac{1}{3}}} & 0 & 0 \\ 0 & \frac{1 - \varepsilon}{(1 - \varepsilon^2)^{\frac{1}{3}}} & 0 \\ 0 & 0 & \frac{1}{(1 - \varepsilon^2)^{\frac{1}{3}}} \end{pmatrix}, \quad (6.23)$$

where the corresponding energy expression is

$$E[\varepsilon, V] = E[0, V_0] + V_0 [C_{11} - C_{12}] \varepsilon^2. \quad (6.24)$$

The fourth strain is volume conserving but not symmetry conserving and it is given by

$$\bar{\bar{F}} = \begin{pmatrix} \frac{1}{(1 - \varepsilon^2)^{\frac{1}{3}}} & 0 & \frac{\varepsilon}{(1 - \varepsilon^2)^{\frac{1}{3}}} \\ 0 & \frac{1}{(1 - \varepsilon^2)^{\frac{1}{3}}} & 0 \\ \frac{\varepsilon}{(1 - \varepsilon^2)^{\frac{1}{3}}} & 0 & \frac{1}{(1 - \varepsilon^2)^{\frac{1}{3}}} \end{pmatrix}, \quad (6.25)$$

where the corresponding energy expression is

$$E[\varepsilon, V] = E[0, V_0] + 2V_0C_{55}\varepsilon^2. \quad (6.26)$$

The fifth and final strain is symmetry conserving but not volume conserving and it is given by

$$\bar{\bar{F}} = \begin{pmatrix} 1 & 0 & 0 \\ 0 & 1 & 0 \\ 0 & 0 & 1 + \varepsilon \end{pmatrix}, \quad (6.27)$$

the corresponding energy expression is

$$E[\varepsilon, V] = E[0, V_0] + \frac{V_0}{2}C_{33}\varepsilon^2. \quad (6.28)$$

Furthermore, the bulk moduli and shear modulus for the hexagonal lattice are given by

$$B = \frac{2}{9} \left[ C_{11} + C_{12} + 2C_{13} + \frac{C_{33}}{2} \right] \quad (6.29)$$

$$B_a = \frac{\Lambda}{2 + \beta} \quad (6.30)$$

$$B_c = \frac{B_a}{\beta} \quad (6.31)$$

$$G = \frac{1}{15} [2C_{11} + C_{33} - C_{12} - 2C_{13}] + \frac{3}{5}C_{55}, \quad (6.32)$$

where

$$\beta = \frac{C_{11} + C_{12} - 2C_{13}}{C_{33} - C_{13}} \quad (6.33)$$

$$\Lambda = 2(C_{11} + C_{12} + 2C_{13}\beta) + C_{33}\beta^2. \quad (6.34)$$

Here  $B_a$  and  $B_c$  are the directional bulk moduli along the a and c directions of the hexagonal lattice. These two quantities will be used when we later on discuss the brittleness of MgB<sub>2</sub>.

### 6.3.2 The strain matrices of a cubic lattice

In this subsection the strain matrices used in extracting the cubic elastic constants will be presented together with their respective energy expressions. The 3 linearly independent constants are

$$C_{11} \quad ; \quad C_{12} \quad ; \quad C_{44}. \quad (6.35)$$

The first strain equals the first hexagonal strain (6.19). The corresponding energy expression in the cubic case is

$$E[\varepsilon, V] = E[0, V_0] + \frac{3V_0}{2} [C_{11} + 2C_{12}] \varepsilon^2. \quad (6.36)$$

The second strain is non symmetry conserving but volume conserving and it is given by

$$\bar{\bar{F}} = \begin{pmatrix} 1 + \varepsilon & 0 & 0 \\ 0 & 1 + \varepsilon & 0 \\ 0 & 0 & \frac{1}{(1 + \varepsilon)^2} \end{pmatrix} \quad (6.37)$$

the corresponding energy expression is

$$E[\varepsilon, V] = E[0, V_0] + 3V_0 [C_{11} - C_{12}] \varepsilon^2 = E[0, V_0] + 6V_0 C' \varepsilon^2, \quad (6.38)$$

where

$$C' = \frac{1}{2} (C_{11} - C_{12}). \quad (6.39)$$

This strain deserves a little extra attention, since it has the useful property of turning the bcc lattice into fcc when  $\varepsilon = 2^{-\frac{1}{6}} - 1$ . This tetragonal strain is referred to as the Bains transformation path, and it will be used later on when the search of superplastic transition metal alloys is discussed in chapter 6.

The third and final strain is also volume preserving but not symmetry conserving and it is given by

$$\bar{\bar{F}} = \begin{pmatrix} 1 & \varepsilon & 0 \\ \varepsilon & 1 & 0 \\ 0 & 0 & \frac{1}{1 - \varepsilon^2} \end{pmatrix} \quad (6.40)$$

The corresponding energy expression is given by

$$E[\varepsilon, V] = E[0, V_0] + 2V_0 C_{44} \varepsilon^2. \quad (6.41)$$

## 6.4 The elastic properties of $\text{Mg}_{(1-x)}\text{Al}_x\text{B}_2$

It is well documented, both experimentally [3, 4] and theoretically [25, 2], that  $\text{MgB}_2$  is an elastically anisotropic material, with a ratio between the inplane  $B_a$  and out of plane  $B_c$  compressibility of  $\sim 1.8$ . Since the elastic anisotropy is known, at least on empirical grounds, to correlate with the brittleness of a material [26], one of the remedies to the brittleness of  $\text{MgB}_2$  would obviously be to suppress this anisotropy. This is in fact the path that has been chosen in paper I of this thesis, and it was attempted by means of Al doping. To understand why aluminum was chosen as a dopant in the attempt to suppress the elastic anisotropy of  $\text{MgB}_2$ , it is instructive to study the previously discussed BCOOP (Fig. 5.3). Here the BCOOP between the boron atoms shows that about 0.1 Ry above the Fermi level the states have marked anti-bonding character. Thus if the electronic structure of  $\text{MgB}_2$  is assumed to be more or less static with respect to electron doping, the

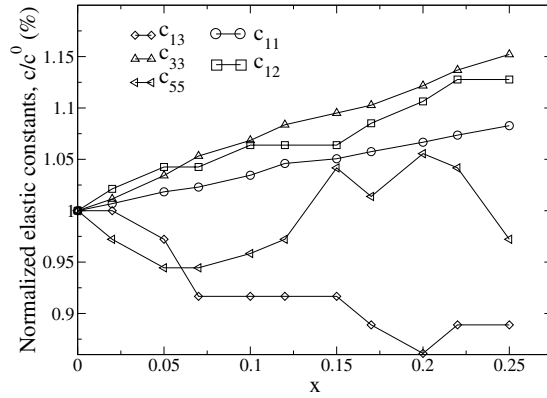


Figure 6.3: The elastic constants (normalized with their respective values at zero concentration of Al) for different dopings of aluminum.

introduction of additional electrons into the system could lead to occupation of these anti-bonding states, resulting in a weakening of the B-B bond. Hence the extra electrons introduced by means of Al doping into the Mg sites could be expected to decrease the inplane bulk modulus  $B_a$  and consequently also decrease the ratio  $B_a/B_c$ .

In Figure 6.3 and Figure 6.4 the results of the FP-LMTO calculations within the virtual crystal approximation (VCA) are displayed. In Figure 6.4 the plot of the ratio  $B_a/B_c$  confirms that Al doping actually decreases the elastic anisotropy. In the same Figure the ratio  $B/G$  is predicted to increase for Al concentrations  $< 5\%$ . The ratio between these particular material constants is important, since it has been argued, at least on empirical grounds, to provide a quantitative measure of the brittleness of a material. The general consensus is that if the ratio  $B/G$  is larger than 1.75 the material is ductile, and if it is less than 1.75 it is brittle [26]. Thus the predictions made by these calculations are that the elastic anisotropy is in fact decreased by Al doping, and the brittleness is decreased for Al concentrations  $< 5\%$ . However since the ratio  $B/G$  stays well below the empirical ductility limit of 1.75, the brittleness of  $MgB_2$  can not be expected to be remedied by forming  $Mg_{(1-x)}Al_xB_2$ .

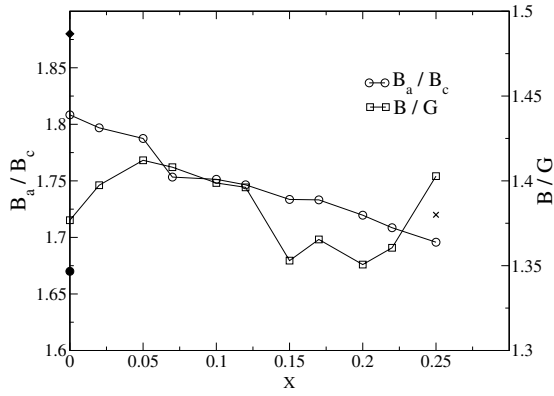


Figure 6.4: Calculated ratios between the two directional bulk moduli  $B_a/B_c$ , together with the ratios between the bulk and shear modulus, for different aluminum dopings. The cross corresponds to a supercell calculation of  $B_a/B_c$ . The filled circle and the diamond correspond to the experimental values of  $B_a/B_c$  found in [3] and [4].



# 7. Predictions of superplastic transition metal alloys

## 7.1 Structural stability in connection with lattice and bond topology

In this section lattice and bond topology will be connected to the structural stability of a solid. This connection will be performed with the help of the theory of moments, which was developed by Cyrot-Lackmann [27] in 1967. The motive for this presentation is to provide the reader with an intuitive understanding of some of the mechanisms behind the concept of structural stability.

### 7.1.1 Theory of moments

The definition of the  $p$ :th moment of an eigenspectrum  $\{E_{\mathbf{k}n}\}$  is defined by

$$\mathcal{M}_p \equiv \sum_{i=1} \sum_{\mathbf{k}} E_{\mathbf{k}i}^p. \quad (7.1)$$

Furthermore if  $H$  is the Hamiltonian corresponding to the eigenspectrum and  $\{\phi_{\mathbf{k}n}\}$  is the basis of eigenfunctions of the Hamiltonian, then

$$H_{ij}(\mathbf{k}, \mathbf{k}') \equiv \langle \phi_{\mathbf{k}i} | H | \phi_{\mathbf{k}'j} \rangle = H_{ij}(\mathbf{k}, \mathbf{k}) \delta_{ij} \delta_{\mathbf{k}\mathbf{k}'} = E_{i\mathbf{k}} \delta_{ij} \delta_{\mathbf{k}\mathbf{k}'}. \quad (7.2)$$

Thus with the aid of (7.2) the  $p$ :th moment can be written as

$$\mathcal{M}_p = \sum_{i=1} \sum_{\mathbf{k}} H_{ii}(\mathbf{k}, \mathbf{k})^p = \sum_{i=1} \text{tr}(H_{ii}^p), \quad (7.3)$$

where  $H_{ii}$  is the  $i$ :th band " $\mathbf{k} \times \mathbf{k}$ " matrix. Bloch's theorem can now be used to express the eigenfunctions  $\{\phi_{\mathbf{k}n}\}$  as a sum of localized wave functions

$$\phi_{\mathbf{k}n}(\mathbf{r}) = \frac{1}{\sqrt{V}} \sum_{\mathbf{R}} \psi_n(\mathbf{r} - \mathbf{R}) e^{i\mathbf{k}\mathbf{R}} \quad (7.4)$$

Now, the above expansion is nothing more than a change of basis from the basis  $\{\psi_n(\mathbf{r} - \mathbf{R})\}$  to the basis  $\{\phi_{\mathbf{k}n}(\mathbf{r})\}$ , with transformation matrix  $U$  defined by

$$U_{ij} \equiv \frac{e^{i\mathbf{k}_i \mathbf{R}_j}}{\sqrt{V}} \quad (7.5)$$

Furthermore this transformation satisfies

$$[U^\dagger U]_{nm} = \frac{1}{V} \sum_i e^{i\mathbf{k}_i(\mathbf{R}_m - \mathbf{R}_n)} = \frac{1}{(2\pi)^3} \int_{\text{BZ}} e^{i\mathbf{k}(\mathbf{R}_m - \mathbf{R}_n)} d\mathbf{k} = \delta_{mn}. \quad (7.6)$$

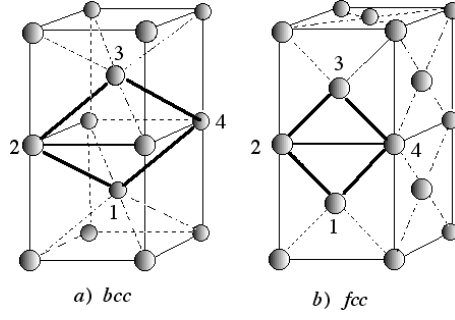


Figure 7.1: The shortest 4 atom paths (thick full drawn lines) of a bcc lattice with corner angles  $70.5^\circ$ ,  $109.5^\circ$  and of a fcc lattice with corner angle  $90^\circ$

Thus, the transformation is unitary, and since the trace is invariant under any unitary transformation we can rewrite (7.3) as

$$\mathcal{M}_p = \sum_i \sum_{\mathbf{R}} H_{ii}^p(\mathbf{R}, \mathbf{R}) = \sum_i \sum_{n_1, n_2, \dots, n_p} H_{ii}(\mathbf{R}_{n_1}, \mathbf{R}_{n_2}) H_{ii}(\mathbf{R}_{n_2}, \mathbf{R}_{n_3}) \cdots H_{ii}(\mathbf{R}_{n_p}, \mathbf{R}_{n_1}) \quad (7.7)$$

where

$$H_{ij}(\mathbf{R}_n, \mathbf{R}_m) = \langle \psi_i(\mathbf{r} - \mathbf{R}_n) | H | \psi_j(\mathbf{r} - \mathbf{R}_m) \rangle. \quad (7.8)$$

Equation (7.7) now provides us with a topological interpretation of the  $p$ :th moment. Namely,  $i$ :th band contribution to the  $p$ :th moment is given by the sum over all bonding paths of length  $p$ . In Figure 7.1 four atom bonding paths of length 4 are displayed for the bcc and fcc lattice. Now if the eigenspectrum is measured relative to the center of the band, it becomes evident from (7.1) that

$$\mathcal{M}_0 = N \quad (\text{The number of eigenvalues of the spectrum}) \quad (7.9)$$

$$\mathcal{M}_1 = \bar{E} = 0 \quad (\text{The weight of the spectrum}) \quad (7.10)$$

$$\frac{1}{N} \mathcal{M}_2 = w^2 \quad (\text{The bandwidth squared of the spectrum}) \quad (7.11)$$

Furthermore the third moment measures the skewness of the spectrum. If  $\mathcal{M}_3 < 0$  the spectrum is skewed downward, if  $\mathcal{M}_3 = 0$  the spectrum is symmetric and if  $\mathcal{M}_3 > 0$  the spectrum is skewed upward. The more  $\mathcal{M}_3$  deviates from zero the more it is skewed. Finally the fourth moment  $\mathcal{M}_4$  measures whether the spectrum has unimodal or bimodal behaviour through the shape parameter

$$s = \frac{\hat{\mathcal{M}}_4}{\hat{\mathcal{M}}_2^2} - \frac{\hat{\mathcal{M}}_3^2}{\hat{\mathcal{M}}_2^3} - 1 \quad (7.12)$$

where

$$\hat{\mathcal{M}}_p \equiv \frac{\mathcal{M}_p}{\mathcal{M}_0} \quad (7.13)$$

If  $s < 1$  the spectrum has bimodal behaviour and if  $s > 1$  it has unimodal behaviour. If a Gaussian modulated fourth order polynomial  $N(E)$  is fitted through the conditions [28]

$$\int_{-\infty}^{\infty} N(E)E^p dE = \mathcal{M}_p \quad ; \quad p = 0, 1, 2, 3, 4 \quad (7.14)$$

the result is

$$N(E) = \frac{e^{-\frac{E^2}{2\hat{\mathcal{M}}_2}}}{\sqrt{2\pi\hat{\mathcal{M}}_2}} \left[ 1 + \frac{\hat{\mathcal{M}}_3}{\hat{\mathcal{M}}_2^2} \left( \frac{E^3}{6\hat{\mathcal{M}}_2} - \frac{E}{2} \right) + \frac{\hat{\mathcal{M}}_4 - 3\hat{\mathcal{M}}_2^2}{24} \left( \frac{3}{\hat{\mathcal{M}}_2^2} - \frac{6E^2}{\hat{\mathcal{M}}_2^3} + \frac{E^4}{\hat{\mathcal{M}}_2^4} \right) \right] \quad (7.15)$$

In Figure 7.2 the above fit has been used on four different sets of the first four moments. From this Figure and the expression (7.7), the effect of the structural topology on the spectrum becomes evident. For instance a monoatomic single cubic structure has no bonding paths of length 3 between nearest neighbour atoms, thus the third moment is very small for such a structure and the corresponding spectrum is symmetric, which is exemplified by Figure 7.2c. Furthermore the fourth moment can be used to determine which structure is the most stable for a half full band. For instance if the competing structures of a half full band are those corresponding to the spectra in Figure 7.2. It is evident that the more bimodal structure (d) is the more stable, since it has, compared to the other structures (a) – (c), more weight concentrated at lower energies.

### 7.1.2 An example: Structural stability of transition metals with a half full d-band

Here we will apply the theory of moments to a simple and illuminating example on the relative stability between the fcc and bcc structure of a transition metal for a half full d-band. This discussion will follow that of Pettifor [29].

First of all it is commonly known that in determining the relative stability of a transition metal in the middle of the period, one can to a good approximation neglect the hybridization of the d-band with the sp-band, and only study the pure d-band contribution to the cohesive energy [30]. Since we have already seen that it is the fourth moment that determines which structure is the more stable in the case of a half full band, we only have to compare the fourth moments of the fcc and bcc d-band. The first thing we must do to compare the two structures is to apply the structural energy difference theorem and set the nearest neighbour distances of the structures equal. This will result in making the contributions from all the nearest neighbour two atom bonding paths

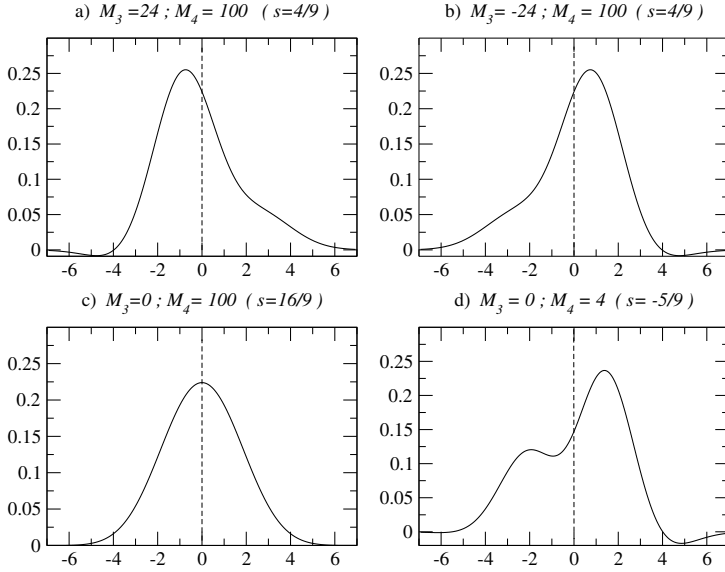


Figure 7.2: Examples of spectra with different third and fourth moment. All spectra have equal zeroth and second moment ( $\mathcal{M}_0 = 4$ ,  $\mathcal{M}_2 = 12$ ). The curves have been obtained through the fit of (7.15).

equal, i.e.

$$(\mathcal{M}_{2p}^{(2)})_{fcc} = (\mathcal{M}_{2p}^{(2)})_{bcc} \quad (7.16)$$

where the number in the super script denotes the number of atoms involved in the bond path. Thus if all paths but the ones going through the nearest neighbour atoms are neglected, the only paths contributing to the difference between fourth moments of the fcc and bcc structures, are the 3 and 4 atom bonding paths of bond length 4. Furthermore, Figure 7.1 reveals that the contributions from the 3 and 4 nearest neighbour atom paths within one structure are equal, i.e.

$$1 \rightarrow 2 \rightarrow 3 \rightarrow 4 \rightarrow 1 \quad \Leftrightarrow \quad 1 \rightarrow 2 \rightarrow 3 \rightarrow 2 \rightarrow 1 \quad (7.17)$$

Thus within the nearest neighbour approximation it is enough to compare the 4 atom path contributions to the fourth moment in order to determine which of the structures that is more stable. From (7.7) we see that this contribution is given by

$$\mathcal{M}_4^{(4)} = \text{Tr}[H_{12}H_{23}H_{34}H_{41}] \quad (7.18)$$

where  $H_{ij}$  are the  $5 \times 5$  tight binding bond matrices, defined by (7.8), between the atoms in Figure 7.1. The 4 atom path contribution (7.18) has been calculated by Moriarty [31] with the result

$$\mathcal{M}_4^{(4)} = \frac{5h^4}{5792} [1757 - 60460x^2 + 327870x^4 - 563500x^6 + 300125x^8] \quad (7.19)$$

where  $x = \cos(\theta)$  and  $h = \frac{1}{5}(dd\sigma^4 + 2dd\pi^4 + 2dd\delta^4)$ . Here  $\theta$  is the bond angle between the atoms in the 4 atom path (see Figure 7.1 ), and  $dd\sigma$ ,  $dd\pi$  and  $dd\delta$  the standard tight binding hopping integrals, see for example Harrison [32]. Now, if the bond angles of the bcc ( $\theta = 70.5^\circ(109.5^\circ)$ ) and the fcc ( $90^\circ$ ) lattice are used in (7.19) the result is

$$(\mathcal{M}_4^{(4)})_{bcc} = -1.42h^4 \quad (7.20)$$

$$(\mathcal{M}_4^{(4)})_{fcc} = 1.52h^4 \quad (7.21)$$

From the above difference in  $\mathcal{M}_4^{(4)}$  it becomes evident that the bcc structure has the more bimodal spectrum, and thus is more stable than fcc.

## 7.2 Structural trends of transition metals

In this section canonical band theory will be used to explain the structural trend  $hcp \rightarrow bcc \rightarrow hcp$  for the transition metals of d-band occupation  $N_d \leq 6$ . This discussion is based on the original theory developed by Andersen [33, 34].

Since in a transition metal one may, to a good approximation, neglect all but the d-bands [30], then the KKR-ASA energy band estimate (4.25)

$$E_{li}(\mathbf{k}) = C_l + \frac{1}{\mu_l S^2} \frac{S_{li}^{\mathbf{k}}}{1 - \gamma_l S_{li}^{\mathbf{k}}} \quad (7.22)$$

may be used. Here the potential parameter  $C_l$  can be interpreted with the help of the following relations

$$\sum_{i=1}^{2l+1} S_{li}^{\mathbf{k}} = 0 \quad (7.23)$$

$$|\gamma_l| \ll 1 \quad (7.24)$$

which implies that

$$\sum_{i=1}^{2l+1} \int_{BZ} (E(\mathbf{k}) - C_l) = \sum_{i=1}^{2l+1} \int_{BZ} \frac{1}{\mu_l S^2} \frac{S_{li}^{\mathbf{k}}}{1 - \gamma_l S_{li}^{\mathbf{k}}} \approx \sum_{i=1}^{2l+1} \int_{BZ} \frac{1}{\mu_l S^2} S_{li}^{\mathbf{k}} = 0 \quad (7.25)$$

Thus the potential parameter  $C_l$  may be interpreted as the center of the band. Similarly the parameter  $\mu_l$  can be shown to be inversely proportional to the bandwidth.

Now the relative stability of two different structures  $n$  and  $m$  is determined by the equation

$$\Delta E_{nm} = \int^{E_F} E D_d^n(E) dE - \int^{E_F} E D_d^m(E) dE, \quad (7.26)$$

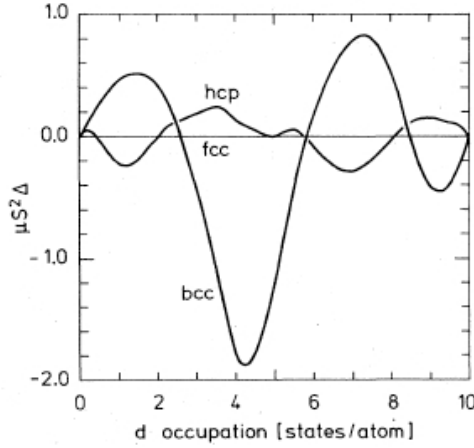


Figure 7.3: Structural energy differences obtained from canonical  $d$  bands, by means of equation 7.28, as a function of  $d$  occupation [30].

derived from the force theorem [35], where  $D_d^n$  and  $D_d^m$  are the partial  $d$  density of states of the competing structures. Since the structure constant  $S_{li}^{\mathbf{k}}$  is independent of the potential, we have, due to (7.24), that the following quantity

$$(E_{di}(\mathbf{k}) - C_d)S^2\mu_d = \frac{S_{di}^{\mathbf{k}}}{1 - \gamma S_{di}^{\mathbf{k}}} \approx S_{di}^{\mathbf{k}} \quad (7.27)$$

is potential, i.e., atomic number independent. From (7.26) and (7.27) we can now create the following atomic number independent estimate of the structural energy difference for a transition metal

$$\Delta E_{nm} \approx \int S_{di}^{\mathbf{k}} D_d^n(S_{di}^{\mathbf{k}}) dS_{di}^{\mathbf{k}} - \int S_{di}^{\mathbf{k}} D_d^m(S_{di}^{\mathbf{k}}) dS_{di}^{\mathbf{k}} \quad (7.28)$$

Since the above estimate only depends on the difference between the two structures, and not on the potential, the structural energy difference is completely determined by the  $d$ -band occupancy. In Figure 7.3 the structural energy difference has been calculated as a function of  $d$ -band occupancy by means of canonical band theory. Here the previously mentioned trend  $hcp \rightarrow bcc \rightarrow hcp$  is reproduced for integer occupational numbers  $\leq 6$ . Here the exception is the 3d element Fe, where magnetic effects are responsible for the actual bcc structure. Furthermore for elements with  $d$ -band occupancy  $> 6$ , the canonical band estimate for the structural trend fails, since hybridization effects, together with magnetic effects for Ni, are too important to be neglected.

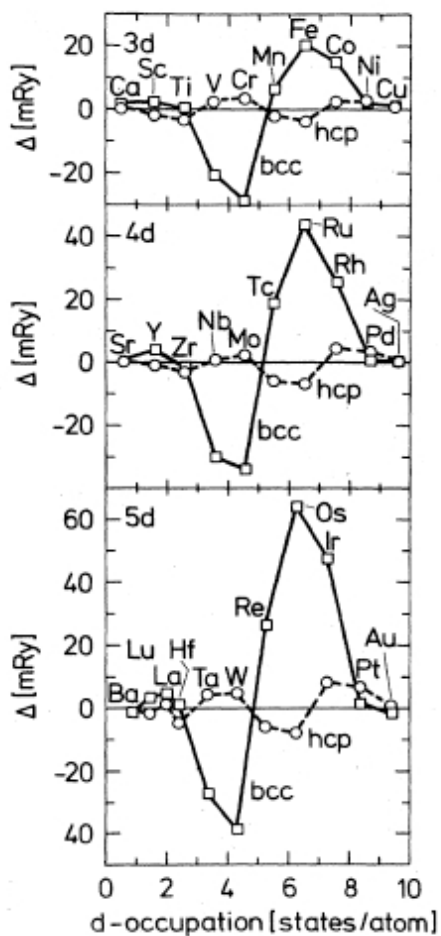


Figure 7.4: Structural energy differences obtained from LMTO-ASA calculations [30].

### 7.3 Super plasticity

Novel materials with improved, tailor made properties are being proposed and synthesized at an impressive rate. Among many examples of materials that have been synthesized to meet one or several specific demands put on them by the application they are intended for, we mention the carbon nano-tubes that have a vast range of mechanical and electrical properties [36], multilayers that are designed to block dislocation movement so that the hardness is improved [37], thin film materials which exhibit the super modulus effect [38], ultra hard oxides [39] and materials for use in fuel cell technology [40]. In many of the studies of advanced material properties, theoretical modeling has been an important tool to help in the understanding of the materials properties and in some cases theory has been used to predict the properties of materials (e.g. the  $C_3N_4$  based materials [41]). It is in particular theoretical modeling based on first principles theory [42] that has been demonstrated to be a very important tool for studies of materials and their properties (e.g. hardness, elasticity, magnetism, and reactivity).

The recent discovery [5] of alloys with 'super properties' (super plasticity, super elasticity, invar and elinvar behaviour and ultra high strength) is no exception to this trend. By combining theory and experiment several alloys were identified that had these extreme properties. The theoretical work suggested one electronic parameter, the average valence electron number (electron/atom ratio), as one of the most critical parameters for these unique alloy properties. The observed dislocation free plastic deformation of the Ti-Ta-Nb-V-Zr-O and Ti-Nb-Ta-Zr-O alloys in Ref. [5] was concluded to be the result of a nearly vanishing shear modulus along the  $\langle 111 \rangle$  direction on the  $\{011\}$ ,  $\{112\}$  and  $\{123\}$  planes, which is closely related to two particular elastic constants  $C'$  and  $C_{44}$ . The mathematical relationship reads

$$G_{111} = \frac{3C_{44}C'}{C' + 2C_{44}}, \quad (7.29)$$

where  $C_{44}$  is the shear modulus along the  $\langle 001 \rangle$  direction along the  $\{011\}$  plane. From first principles calculations it was found that for the super plastic alloys studied one obtained a vanishing tetragonal shear constant, i.e.  $C'$  approached zero. This means that  $G_{111}$  became very low, and superplasticity was argued to follow since the  $\langle 111 \rangle$  direction on the  $\{011\}$ ,  $\{112\}$  and  $\{123\}$  planes are the typical slip systems for the bcc crystals [5]. Thus using the same arguments as in Ref. [5], the vanishing of the elastic constant  $C'$ , predicted for the transition metal alloys W-Re, Mo-Tc and Fe-Co in paper II of this thesis, are suggested to be possible candidates for having superplastic properties.

### 7.3.1 Results

In this section the results of the calculations made in paper II will be presented in the context of the previously reviewed canonical band theory and theory of elasticity.

We begin by returning to the tetragonal distortion (6.37) of amplitude  $\varepsilon = 2^{-\frac{1}{6}} - 1 \approx -0.11$  which took the bcc structure to the fcc structure. Using this amplitude in the corresponding energy expression of the distortion (6.38) the result is

$$\Delta E_{\text{bcc-fcc}} \approx 6C'(2^{-\frac{1}{6}} - 1)^2. \quad (7.30)$$

The above relation is approximate since the relation between energy and distortion amplitude is only correct to second order. Nevertheless it tells us that if a material has a structural instability between the fcc and bcc structure, the material surely would have a very small tetragonal elastic constant.

From the canonical structural energy difference curve in Figure 7.3 it becomes evident that such instabilities might be expected to be found in transition metal alloys with d-band occupation just below 3, 6 and 8.5 electrons. However, these canonical estimates are a bit crude since they do not take correlation effects and hybridization with the sp-band into account. The same structural energy differences calculated with the LMTO-ASA method, displayed in Figure 7.4, show that the previously mentioned structural instabilities might be expected to be found in the W-Re and Mo-Tc alloys. Since the structural energy differences in Figure 7.4 are the results of a non spin-polarized calculation, the predicted structural stability of the magnetic 3d elements Fe and Co are incorrect. A spin polarized calculation for these elements would, similarly to the 4d and 5d elements, show a bcc to fcc instability between Fe and Co.

The above observations inspired the calculations of the tetragonal elastic constant  $C'$  for the alloys  $Fe_{1-x}Co_x$ ,  $Mo_{1-x}Tc_x$  and  $W_{1-x}Re_x$ . These calculations were performed by the FP-LMTO code within the VCA approximation with  $0 < x < 1$ . The results of these calculations are presented in Figure 7.5.

These results show that the tetragonal elastic constant indeed becomes vanishingly small for dopings around 0.9, 0.6 and 0.95. However it is also evident that the bcc structure becomes unstable relative to both the fcc and hcp structures before the superplastic transition has occurred. Hence, in order to observe superplasticity in the alloys under consideration, one has to find ways to stabilize the bcc crystal structure. One of the possible ways to do just that might be to add small amounts of other elements in the same way as was done by Saito et al [5]. They used the fcc-bcc instability for d-band occupations  $\sim 2.2$  (see Figure 7.4), by hole doping of the elements V, Nb and Ta, with Zr, La, and Ti. The bcc structure was stabilized by the formation of Ti-Ta-Nb-V-Zr-O and Ti-Nb-Ta-Zr-O alloys.

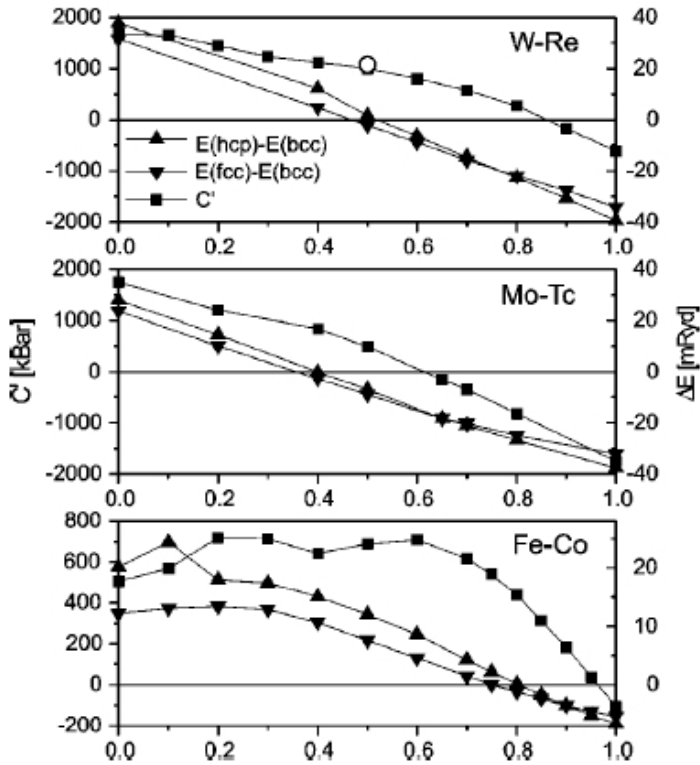


Figure 7.5: The calculated tetragonal elastic constants of Fe-Co, Mo-Tc and W-Re alloys (filled squares). The calculated energy differences among-bcc, fcc and hcp crystal structures are also shown (filled triangles and filled upside down triangles). For W-Re alloys the elastic constant from the VCA was compared to a supercell calculation (open circle).

## 8. Lattice dynamics

In this the final chapter of the thesis perhaps the most interesting results will be presented. Here we will start with a short review of harmonic lattice theory together with a brief discussion of how lattice dynamics can be calculated from ab-initio theory. Here special focus will be on the so-called supercell method, since this is the method that has been used through out this thesis to calculate phonons from ab-initio theory. After this brief introduction the results obtained within the harmonic, or rather quasi harmonic, approximation will be presented (see papers III, IV and VI). The chapter is ends with a discussion of the anharmonic lattice and a presentation of the self-consistent ab-initio lattice dynamical (SCAILD) approach, and the results obtained with this novel approach (see paper V) will also be discussed.

### 8.1 The Born Oppenheimer approximation

Before discussing the theory of lattice dynamics and the associated calculational methods, it is important to take a closer look at one of the fundamental approximations used in calculating phonons from first principles. This approximation is commonly known as the Born Oppenheimer approximation, and it assumes that the electronic response to an atomic displacement is instantaneous, making it possible to separate the electronic and the ionic subsystems. To convince oneself of the soundness of this approximation one should remember that the typical ionic mass  $m_i$  is  $\sim 10^5$  times bigger than the mass of an electron  $m_e$  and that the typical kinetic energy of an electron  $E_{ke}$  is  $\sim 10^3$  times bigger than the typical ionic kinetic energy  $E_{ki}$ , implying that the ratio between the typical velocity of an electron  $v_e$  and that of an ion  $v_i$  becomes  $(v_e/v_i) = \sqrt{E_{ke}m_i/(E_{ki}m_e)} \sim 10^4$ . Thus from the "perspective of an electron", the ions will always seem to have fixed positions. Hence if  $\mathbf{U}(\mathbf{R})$  are the deviations of the ions from their equilibrium positions at a snapshot in time, it is always possible to retain the total energy of the system, at that snapshot, by means of a static electronic structure calculation. Thus, through a series of electronic structure calculations, the potential energy of the ionic subsystem can be parameterized in terms of ionic deviations. It is general practice to express the potential energy in the Hamiltonian of the ionic subsystem, as a Taylor expansion around the equilibrium ionic configuration

$$\begin{aligned}
\mathcal{H} = & \sum_{\mathbf{R},\sigma} \frac{\mathbf{P}_{\mathbf{R}\sigma}^2}{2M_\sigma} + \frac{1}{2} \sum_{\mathbf{R},\sigma} \sum_{\mathbf{R}',\sigma'} \mathbf{U}_{\mathbf{R}\sigma} \bar{\bar{\Phi}}(\mathbf{R} + \mathbf{b}_\sigma - \mathbf{R}' - \mathbf{b}_{\sigma'}) \mathbf{U}_{\mathbf{R}'\sigma'} + \\
& \frac{1}{3!} \sum_{\mathbf{R},\sigma} \sum_{\mathbf{R}',\sigma'} \sum_{\mathbf{R}'',\sigma''} \sum_{\alpha\beta\gamma} \Phi_{\alpha\beta\gamma}(\mathbf{R} + \mathbf{b}_\sigma, \mathbf{R}' + \mathbf{b}_{\sigma'}, \mathbf{R}'' + \mathbf{b}_{\sigma''}) U_{\mathbf{R}\alpha} U_{\mathbf{R}'\beta} U_{\mathbf{R}''\gamma} + \dots
\end{aligned} \tag{8.1}$$

Here  $\mathbf{P}_{\mathbf{R}\sigma}$  and  $\mathbf{U}_{\mathbf{R}\sigma}$  are the momentum operator and the atomic displacement, respectively, of the atom with equilibrium lattice position  $\mathbf{R} + \mathbf{b}_\sigma$ . Furthermore,  $\mathbf{b}_\sigma$  is the atomic coordinate relative to the primitive lattice,  $M_\sigma$  the atomic mass,  $\bar{\bar{\Phi}}$  the force constant matrix and  $\Phi_{\alpha\beta\gamma}$  a tensor describing the third order anharmonic contribution to the potential energy.

## 8.2 The harmonic lattice

In the harmonic lattice approximation the atomic deviations are assumed to be so small that the potential energy is well described by the second order term in (8.1). This is generally a good approximation, at least at relatively low temperatures. Later on in this chapter examples of situations will be given in which the harmonic approximation fails, such as the high temperature bcc phase of Ti, Zr and Hf. Furthermore, in order to make the notation more transparent, the notation of a monoatomic lattice will be adapted without any loss of generality. The harmonic Hamiltonian in the case of a monoatomic lattice is given by

$$\mathcal{H}_h = \sum_{\mathbf{R}} \frac{\mathbf{P}_{\mathbf{R}}^2}{2M} + \frac{1}{2} \sum_{\mathbf{R}} \sum_{\mathbf{R}'} \mathbf{U}_{\mathbf{R}} \bar{\bar{\Phi}}(\mathbf{R} - \mathbf{R}') \mathbf{U}_{\mathbf{R}'} \tag{8.2}$$

In the harmonic approximation, the ionic displacements  $\mathbf{U}_{\mathbf{R}}$  satisfy Born von Karman periodic boundary conditions. This means that the displacements can be expressed as a superposition of plane waves with wavevectors  $\mathbf{k} \in 1 \text{ BZ}$ . Hence the canonical coordinates  $\mathbf{U}_{\mathbf{R}}$  and  $\mathbf{P}_{\mathbf{R}}$  appearing in (8.2), can be expressed in terms of a new set of canonical coordinates  $\mathcal{Q}_{\mathbf{k},s}$  and  $\mathcal{P}_{\mathbf{k},s}$ , i.e

$$\mathbf{U}_{\mathbf{R}} = \frac{1}{\sqrt{MN}} \sum_{\mathbf{k},s} \mathcal{Q}_{\mathbf{k},s} \boldsymbol{\varepsilon}_{\mathbf{k},s} e^{i\mathbf{k}\mathbf{R}} \tag{8.3}$$

$$\mathbf{P}_{\mathbf{R}} = \frac{1}{\sqrt{MN}} \sum_{\mathbf{k},s} \mathcal{P}_{\mathbf{k},s} \boldsymbol{\varepsilon}_{\mathbf{k},s} e^{i\mathbf{k}\mathbf{R}}. \tag{8.4}$$

Here  $\boldsymbol{\varepsilon}_{\mathbf{k},s}$  are the eigenvectors to the dynamical matrix  $\bar{\bar{\mathcal{D}}}(\mathbf{k})$  defined by

$$\bar{\bar{\mathcal{D}}}(\mathbf{k}) = \frac{1}{M} \sum_{\mathbf{R}} \bar{\bar{\Phi}}(\mathbf{R}) e^{-i\mathbf{k}\mathbf{R}}. \tag{8.5}$$

Inserting the expressions (8.3) and (8.4) into the Eq. (8.2), the Hamiltonian gets separated into the Hamiltonians of  $3N$  independent harmonic oscillators

$$\mathcal{H}_h = \sum_{\mathbf{k}s} \mathcal{H}_{\mathbf{k}s} \quad (8.6)$$

$$\mathcal{H}_{\mathbf{k}s} = \frac{1}{2} (\mathcal{P}_{\mathbf{k}s}^2 + \omega_{\mathbf{k}s}^2 \mathcal{Q}_{\mathbf{k}s}^2) \quad (8.7)$$

where  $\omega_{\mathbf{k}s}^2$  are the eigenvalues of the dynamical matrix (8.5). Furthermore, introducing the well known creation and annihilation operators  $a_{\mathbf{k}s}^\dagger$  and  $a_{\mathbf{k}s}$ , defined by

$$a_{\mathbf{k}s}^\dagger \equiv \sqrt{\frac{\omega_{\mathbf{k},s}}{2\hbar}} \mathcal{Q}_{\mathbf{k},s} - i \frac{\mathcal{P}_{\mathbf{k}s}}{\sqrt{2\hbar\omega_{\mathbf{k},s}}} \quad (8.8)$$

$$a_{\mathbf{k}s} \equiv \sqrt{\frac{\omega_{\mathbf{k},s}}{2\hbar}} \mathcal{Q}_{\mathbf{k},s} + i \frac{\mathcal{P}_{\mathbf{k}s}}{\sqrt{2\hbar\omega_{\mathbf{k},s}}} \quad (8.9)$$

and making use of the commutation relation  $[\mathcal{P}_{\mathbf{k}s}, \mathcal{Q}_{\mathbf{k},s}] = -i\hbar$ , the Hamiltonians (8.7) can be rewritten into the following form

$$\mathcal{H}_{\mathbf{k}s} = \hbar\omega_{\mathbf{k}s} (a_{\mathbf{k}s}^\dagger a_{\mathbf{k}s} + \frac{1}{2}). \quad (8.10)$$

Finally, from the definitions (8.8) and (8.9) it is straightforward to show (see for example the book by Taylor and Heinonen [43]) that

$$[a_{\mathbf{k}s}, a_{\mathbf{k}'s'}^\dagger] = \delta_{\mathbf{k}\mathbf{k}'} \delta_{ss'} \quad (8.11)$$

$$[a_{\mathbf{k}s}^\dagger, a_{\mathbf{k}'s'}^\dagger] = [a_{\mathbf{k}s}, a_{\mathbf{k}'s'}] = 0 \quad (8.12)$$

and that the eigenstates and eigenvalues of  $\mathcal{H}_{\mathbf{k}s}$  are given by

$$E_{n\mathbf{k}s} = \hbar\omega_{\mathbf{k}s} (\frac{1}{2} + n), \quad n \in \mathbf{N} \quad (8.13)$$

$$|n\rangle = \frac{(a_{\mathbf{k}'s'}^\dagger)^n}{\sqrt{n!}} |0\rangle \quad (8.14)$$

Here the state  $|0\rangle$  is defined by  $a_{\mathbf{k}s}|0\rangle = 0$  and  $\mathcal{H}_{\mathbf{k}s}|0\rangle = \hbar\omega_{\mathbf{k}s}|0\rangle$ .

As seen from the above discussion, in the harmonic approximation, the excitations of the lattice can be viewed as plane waves, which as they travel through the material move the atoms along directions given by the eigenvectors  $\mathbf{e}_{\mathbf{k}s}$ , or as bosonic particles propagating through the material carrying energy quanta  $\hbar\omega_{\mathbf{k}s}$ , more commonly known as phonons.

### 8.3 The supercell method

In the previous section it was shown that once the force constant matrix  $\bar{\bar{\Phi}}$  has been calculated and Fourier transformed, the phonon frequencies are easily accessed by a simple diagonalization. Fortunately there exists a fairly simple and straightforward method for calculating  $\bar{\bar{\Phi}}$  from first principles, namely the so-called supercell method. The foundation of the method is provided by the Hellman-Feynman theorem, stating that the force  $\mathbf{F}_{\mathbf{R}}$  acting on an atom with spatial coordinate  $\mathbf{R}$  is given by

$$\mathbf{F}_{\mathbf{R}} = -\langle \Psi | \nabla_{\mathbf{R}} \mathcal{H} | \Psi \rangle \quad (8.15)$$

Here  $\Psi$  is the wavefunction of the electronic groundstate, and  $\mathcal{H}$  the Hamiltonian of the electron system parameterized by the spatial coordinates of the atoms. The Hellman-Feynman theorem is then used to calculate the interatomic forces induced by displacing one of the atoms in the supercell. For example if an atom at position, lets say  $\mathbf{R} = 0$ , is moved, then the induced forces can be expressed in terms of the force constant matrix and the displacement  $\mathbf{U}_0$

$$\mathbf{F}_{\mathbf{R}} = -\bar{\bar{\Phi}}(\mathbf{R})\mathbf{U}_0. \quad (8.16)$$

From the above linear relation and the symmetry of the crystal the force constant matrix can then be easily calculated. The number of displacements needed to retain  $\bar{\bar{\Phi}}$  depends on the symmetry of the crystal. For instance in the case of the bcc or fcc structure one displacement is sufficient, while in the case of the hcp structure two displacements are needed.

However since, at least in principle,  $\bar{\bar{\Phi}}_{ij}(\mathbf{R}) \rightarrow 0$  only as  $|\mathbf{R}| \rightarrow \infty$ , and since only finite sized supercells can be used, the summation in (8.5) has to be truncated, and the dynamical matrix can only be approximately calculated. Furthermore, due to the periodic boundary conditions employed in the electronic structure calculations, the linear relation (8.16) is only true if an infinite sized supercell is used. In real life all the periodic images of the displaced atom contribute in the induction of the forces in the supercell. The correct linear relation between force and displacement(s), to be used in a supercell calculation, is given by

$$\mathbf{F}_{\mathbf{R}} = -\left( \sum_{\mathbf{L}} \bar{\bar{\Phi}}(\mathbf{R} + \mathbf{L}) \right) \mathbf{U}_0 \quad (8.17)$$

where  $\mathbf{L}$  is a generic lattice vector of the supercell. Consequently, the approximate dynamical matrix obtained from a supercell calculation is given by

$$\tilde{D}(\mathbf{k}) = \frac{1}{M} \sum_{\mathbf{R} \in SC} \bar{\bar{\Phi}}(\mathbf{R}) e^{i\mathbf{k}\mathbf{R}} + \frac{1}{M} \sum_{\mathbf{R} \in SC, \mathbf{L} \neq 0} \bar{\bar{\Phi}}(\mathbf{R} + \mathbf{L}) e^{i\mathbf{k}\mathbf{R}}, \quad (8.18)$$

where  $SC$  is the set of primitive lattice vectors in the supercell. It is instructive to decompose the sum in the expression of the exact dynamical matrix, into

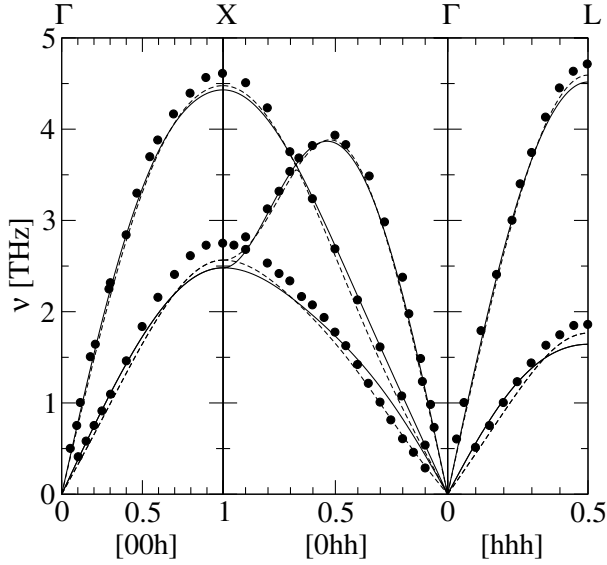


Figure 8.1: The phonon dispersion of fcc Au at room temperature and ambient pressure. The solid curve are the frequencies from the  $3 \times 3 \times 3$  supercell at the experimental volume  $V_0 = 16.96 \text{ \AA}^3$ . The dashed curve are the frequencies from the  $4 \times 4 \times 4$  supercell at the experimental volume. The filled circles are the experimental data of Lynn *et al* [44].

sums over lattice vectors belonging to the supercell and over generic supercell vectors, i.e

$$\bar{\bar{D}}(\mathbf{k}) = \frac{1}{M} \sum_{\mathbf{R} \in SC} \bar{\Phi}(\mathbf{R}) e^{i\mathbf{k}\mathbf{R}} + \frac{1}{M} \sum_{\mathbf{R} \in SC, \mathbf{L} \neq 0} \bar{\Phi}(\mathbf{R} + \mathbf{L}) e^{i\mathbf{k}(\mathbf{R} + \mathbf{L})}. \quad (8.19)$$

From the two expressions (8.18) and (8.19) the importance of minimizing the contributions to  $\bar{\bar{D}}(\mathbf{k})$  from force constants between atoms in different Wigner-Seitz cells of the superlattice becomes obvious. But it also becomes clear that for wave vectors commensurate with the superlattice ( $\mathbf{k}\mathbf{L} = 2\pi$ ), the dynamical matrix given by (8.18) is exact! Thus increasing the supercell size not only enhances the accuracy of the phonons with incommensurate wave vectors due to the fact that  $\bar{\Phi}(\mathbf{R} + \mathbf{L}) \rightarrow 0$  for  $\mathbf{L} \neq 0$ , but also because the number of exactly calculated phonons increase, which in turn makes the interpolation used for calculating the phonons with incommensurate wave vectors more exact. In Fig. 8.1 supercell calculations for fcc Au using two different supercell sizes are shown (paper III). Here it can be seen that the calculated phonons only slightly change as the supercell size is increased from  $3 \times 3 \times 3$  to  $4 \times 4 \times 4$ , suggesting that  $3 \times 3 \times 3$  calculation is more or less converged with respect to cell size.

In all the phonon calculations presented in this thesis the Hellman-Feynman forces have been calculated with the PAW method implemented

in the Viena Ab-initio Simulation Package (VASP) [45]. For selecting the appropriate displacements and extracting the force constant matrix from the Hellman-Feynman forces, the code of Ref. [46] has been used in all harmonic phonon calculations presented in this thesis.

## 8.4 Some thermodynamics and the quasi harmonic approximation

In this section relations between the harmonic phonon spectrum and different thermodynamic quantities, such as the free energy, internal energy and mean square atomic deviation, will be derived and briefly discussed. Furthermore a short presentation of the quasi harmonic approximation will also be given.

The thermodynamic average of an arbitrary operator  $\hat{A}$  is given by

$$\langle A \rangle = \frac{\text{Tr}[\hat{A}e^{-\frac{\mathcal{H}}{k_B T}}]}{\mathcal{Z}}, \quad (8.20)$$

where  $\mathcal{Z}$  is the partition function and  $\text{Tr}$  the trace, defined by

$$\mathcal{Z} = \text{Tr}[e^{-\frac{\mathcal{H}}{k_B T}}] \equiv \sum_n \langle \Psi_n | e^{-\frac{\mathcal{H}}{k_B T}} | \Psi_n \rangle \quad (8.21)$$

where  $\Psi_n$  is an eigen state of the Hamiltonian  $\mathcal{H}$ . With the above definitions, and the properties of the harmonic oscillator derived in section 7.2, it is now easy to calculate the partition function  $\mathcal{Z}$  and the thermodynamic average of the operator  $\mathcal{Q}_{\mathbf{k}s}^\dagger \mathcal{Q}_{\mathbf{k}s}$  for a phonon mode  $s$  with wave vector  $\mathbf{k}$

$$\mathcal{Z} = \prod_{\mathbf{k}s} \text{Tr}[e^{-\frac{\mathcal{H}_{\mathbf{k}s}}{k_B T}}] = \prod_{\mathbf{k}s} \mathcal{Z}_{\mathbf{k}s} \quad (8.22)$$

$$\langle \mathcal{Q}_{\mathbf{k}s}^\dagger \mathcal{Q}_{\mathbf{k}s} \rangle = \frac{\text{Tr}[\mathcal{Q}_{\mathbf{k}s}^\dagger \mathcal{Q}_{\mathbf{k}s} e^{-\frac{\mathcal{H}_{\mathbf{k}s}}{k_B T}}]}{\mathcal{Z}_{\mathbf{k}s}} = \frac{\hbar}{\omega_{\mathbf{k}s}} \left[ \frac{1}{2} + \bar{n} \left( \frac{\hbar \omega_{\mathbf{k}s}}{k_B T} \right) \right] \quad (8.23)$$

where  $\bar{n}(x) = 1/(e^x - 1)$  and

$$\mathcal{Z}_{\mathbf{k}s} = \text{Tr}[e^{-\frac{\mathcal{H}_{\mathbf{k}s}}{k_B T}}] = \sum_{n=0}^{\infty} e^{-\frac{\hbar \omega_{\mathbf{k}s}}{k_B T} (\frac{1}{2} + n)} = \frac{e^{-\frac{\hbar \omega_{\mathbf{k}s}}{2k_B T}}}{1 - e^{-\frac{\hbar \omega_{\mathbf{k}s}}{k_B T}}}. \quad (8.24)$$

From the partition function, the internal energy  $E$  and the free energy  $F$  is also easily calculated

$$E = \frac{\text{Tr}[\mathcal{H} e^{-\frac{\mathcal{H}}{k_B T}}]}{\mathcal{Z}} = -\frac{\partial \ln(\mathcal{Z})}{\partial (\frac{1}{k_B T})} = \sum_{\mathbf{k},s} \left[ \hbar \omega_{\mathbf{k}s} \left[ \frac{1}{2} + \bar{n} \left( \frac{\hbar \omega_{\mathbf{k}s}}{k_B T} \right) \right] \right] \quad (8.25)$$

$$F = -k_B T \ln(\mathcal{Z}) = \sum_{\mathbf{k},s} \left[ \frac{\hbar \omega_{\mathbf{k}s}}{2} + k_B T \ln \left[ 1 - e^{-\frac{\hbar \omega_{\mathbf{k}s}}{k_B T}} \right] \right] \quad (8.26)$$

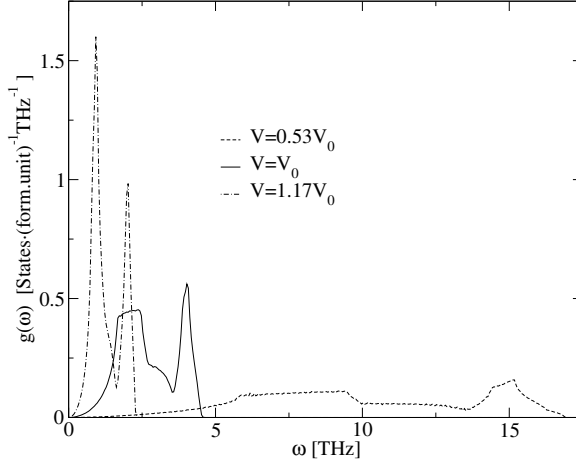


Figure 8.2: The calculated phonon density of states for three different volumes of fcc Au. The volume  $V_0$  is the experimental volume at ambient conditions.

By introducing the phonon density of states  $g(\omega)$ , (8.25) and (8.26) can be expressed in integral form

$$E = \int_0^\infty d\omega g(\omega) \hbar\omega \left[ \frac{1}{2} + \bar{n} \left( \frac{\hbar\omega}{k_B T} \right) \right] \quad (8.27)$$

$$F = \int_0^\infty d\omega g(\omega) \left[ \frac{\hbar\omega}{2} + k_B T \ln \left[ 1 - e^{-\frac{\hbar\omega}{k_B T}} \right] \right] \quad (8.28)$$

The two above expressions for the internal- and free-energy have been used in the context of the so-called quasi harmonic approximation to calculate Equations of state, Hugoniot and thermal expansions (see papers III, IV and VI).

What now remains in this section is a short discussion of the quasi harmonic approximation. This is the most simple approximation dealing with the effects of anharmonicity in which the anharmonicity related to the terms of order  $> 2$  in the Taylor expansion (8.1) is neglected, only taking into account the anharmonicity related to the force constants dependence upon symmetry conserving strain. The simplicity of this approximation lies in the fact that for each symmetry conserving strain the lattice dynamics of the system is regarded as being harmonic, permitting the use of the supercell method separately for each symmetry conserving strain. In Fig. 8.2 the phonon density of states for fcc Au calculated with the supercell method for three different volumes are displayed, as an example of the volume dependence of the phonon spectra.

## 8.5 The equation of state and the Hugoniot of fcc Au

In this section paper III of this thesis will be discussed. This presentation will also serve as a first example of how, and why calculations of lattice dynamics from first principles are important in modern physics.

The answer to the question why the investigation in paper III was done leads us to yet another question, namely; How accurate is the pressure calibration provided by the high-pressure equation of state (EOS) of fcc Au? This doubt concerned with the pressure standard provided by the EOS of Au originates from recent experiments [47], where the secondary standard of the  $R_1$  ruby line, calibrated with the EOS of Au, was used as a pressure standard. Furthermore, analyses of the static EOS data of diamond and Ta have suggested that the ruby pressure scale might underestimate pressure by  $\sim 10$  GPa at 150 GPa [48, 49, 50]. These suggestions of an underestimated pressure scale has also been supported in the experimental work by Dewaele *et al* [51], who have proposed a new ruby pressure scale. Thus since the foundation of all high pressure experiments was being questioned, the need for an EOS of Au calculated from first principles was obvious.

The calculations of the EOS of gold was done by calculating the total free energy of fcc Au

$$F(V, T) = U(V) + F^{phon}(V, T) + F^{el}(V, T), \quad (8.29)$$

where  $U(V)$  is the static lattice energy calculated with the FPLMTO method,  $F^{phon}(V, T)$  the phonon contribution to the free energy (see Eq. 8.26) calculated by means of the supercell method and  $F^{el}(V, T)$  the free energy of the electronic subsystem here calculated with the Sommerfeld approximation [52]

$$F^{el}(V, T) = -\frac{(\pi k_B)^2}{6} N(\epsilon_F, V) T^2, \quad (8.30)$$

where  $N(\epsilon_F, V)$  is the electronic density of states at the Fermi level.

In Fig. 8.3, upper panel (a), the calculated room temperature isotherm of paper III is shown together with experimental data and other theoretical EOS. In the lower panel (b), the differences between the isotherm and the other experimental and theoretical data are shown. From panel (a) in Fig 8.3 it can be seen that the present isotherm is in good agreement with experimental data. Furthermore, in panel (b) it can be seen that the best agreement between the present isotherm and other EOS is found with the EOS of Dewaele based on a new calibration of the ruby scale. For compressions around  $V/V_0 = 0.75$  the theoretical and experimental EOS data obtained with the old calibration lies  $\sim 10$  GPa lower in pressure. Thus the results of the calculations of paper III, add further support to the doubts concerned with the old ruby pressure scale.

In paper III a more direct comparison to experimental data was also made without any reference to pressure calibration. In a typical high pressure shock wave experiment a driver is shot with high velocity into a sample, and a shock

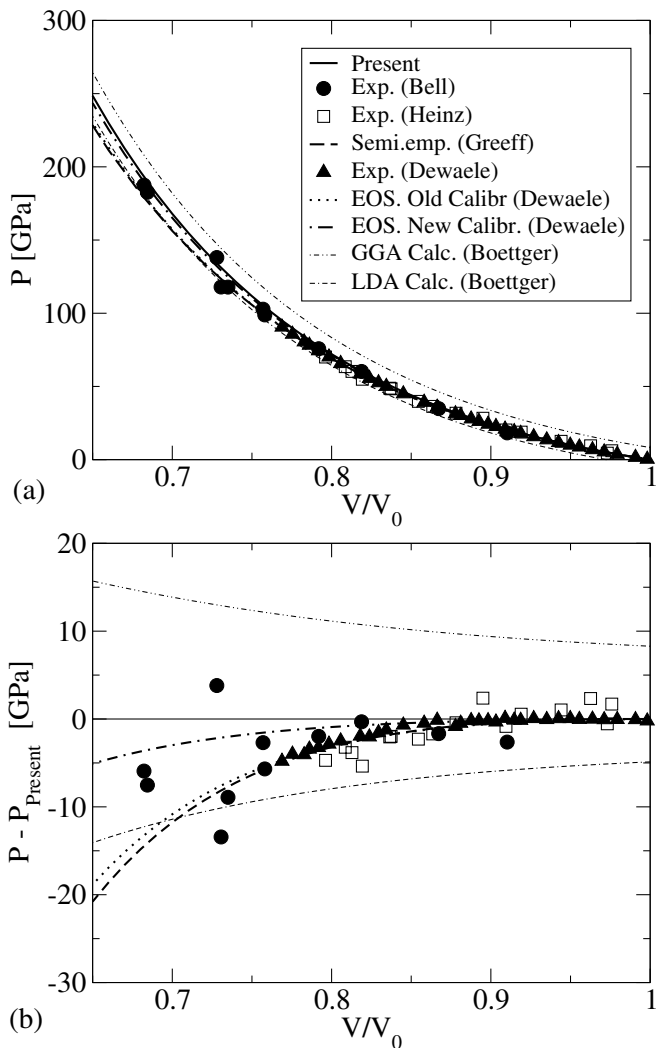


Figure 8.3: (a) Theoretical and experimental isotherms for Au at  $T=298\text{K}$ . Here  $V_0$  is equal to the experimental volume at ambient conditions. The solid curve is the present EOS. Filled circles are the data of Bell *et al* [53]. The open squares are the data of Heinz and Jeanloz [54]. The dashed curve is the EOS of Greeff and Graf [55]. The filled triangles are the data of Dewaele *et al* [51]. The dotted line is the EOS of Dewaele *et al* [51] obtained with the standard ruby scale [56]. The dashed dotted line is the EOS of Dewaele *et al* [51] obtained with their recalibrated ruby scale. The double dotted dashed line is the GGA calculation of Boettger [57]. The double dashed dotted line is the LDA calculation of Boettger [57]. (b) Difference between the present isotherm and the other experimental and theoretical data in (a).

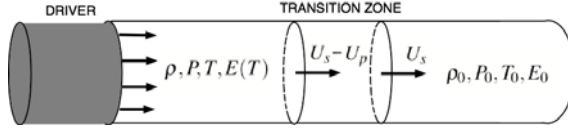


Figure 8.4: Schematic figure of a shock front traveling through a cylindrical sample. Here  $U_s$  is the velocity of the frontal boundary of the shock,  $U_s - U_p$  is the velocity of the back boundary of the shock wave,  $\rho$  and  $\rho_0$  are densities to the left and right of the shock wave,  $P$  and  $P_0$  are pressures to the left and right of the shock wave,  $E(T)$  and  $E_0$  are internal energy per unit cell to the left and right of the shock wave.

wave is transferred into the sample material. By measuring the velocities of the back and front of the shock wave the pressure can be calculated. In Fig. 8.4 a schematic picture is shown of a typical high pressure experiment. The relation between the shock velocities and the pressure behind the shock wave can easily be derived by first assuming that there is no mass accumulation in the transition zone (see Fig. 8.4), i.e the mass flux in and out of the transition zone are assumed to be equal

$$(U_s - U_p)\rho = U_s\rho_0, \quad (8.31)$$

where  $\rho$  and  $\rho_0$  are the densities behind and in front of the transition zone,  $U_s - U_p$  is the velocity of the rear boundary of the shock and  $U_s$  is the velocity of the frontal boundary of the shock wave. Then by using the above relation the momentum flux  $P - P_0$  into the transition region can be expressed as

$$P - P_0 = \rho_0 U_s^2 - \rho(U_s - U_p)^2 = \rho_0 U_s U_p, \quad (8.32)$$

where  $P$  is the pressure behind the shock wave and  $P_0$  the pressure in front of the shock wave. By varying the impact velocity of the driver a non-isothermal relation between pressure and volume, more commonly known as the Hugoniot can be obtained.

To calculate the pressure behind the shock front from first principles the so-called jump condition is employed. This condition requires that the energy flux  $\Phi_{in}$  into the transition zone equals the energy flux  $\Phi_{out}$  out of the transition zone. Here  $\Phi_{in}$  and  $\Phi_{out}$  are given by

$$\Phi_{in} = \frac{E(T)}{m}\rho(U_s - U_p) + \frac{(U_s - U_p)^3}{2}\rho + P(U_s - U_p) \quad (8.33)$$

$$\Phi_{out} = \frac{E_0}{m}\rho_0 U_s + \frac{U_s^3}{2}\rho_0 + P_0 U_s, \quad (8.34)$$

$$(8.35)$$

where  $E(T)$  and  $E_0$  are internal energies per unit cell to the back and in front of the shock wave and  $m$  is the mass per unit cell. From the requirement that  $\Phi_{in} = \Phi_{out}$  and the relations (8.31) and (8.32) the internal energy change due

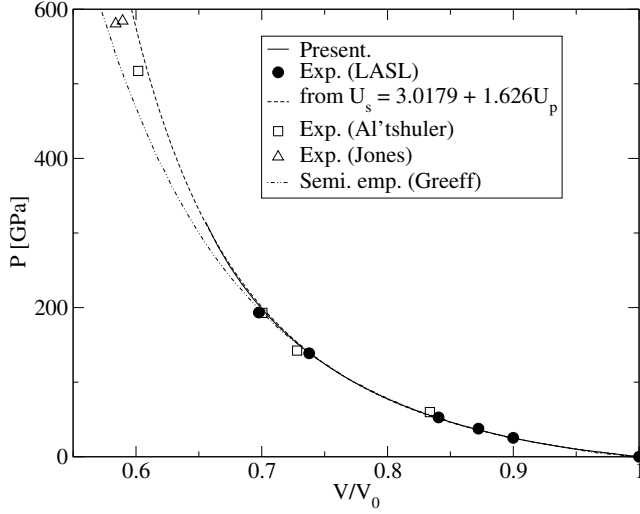


Figure 8.5: Theoretical and experimental Hugoniot of Au. Here  $V_0$  is the experimental volume. The solid line is the present Hugoniot. The dashed line is obtained from calculated shock velocities  $U_s = 3.0179 + 1.626U_p$ . The filled circles are the experimental LASL data [58]. Empty squares data of Al'tshuler [59]. The empty triangles are the data of Jones [60].

to the shock can be related to the volume change and the pressure behind the shock wave

$$E(V, T) - E_0 = \frac{1}{2}(P(T, V) + P_0)(V_0 - V), \quad (8.36)$$

where  $V_0$  is the initial volume in front of the shock wave and  $V$  the volume behind the shock wave. The above equation is known as the Hugoniot equation. The internal energy  $E(V, T)$  and the pressure  $P(V, T) = -\partial F(V, T)/\partial V$  can then be calculated from the phonon density of states and the total free energy (8.29). In Fig. 8.7 the calculated Hugoniot for fcc Au is shown together with experimental and theoretical data of Greeff *et al* [55]. Here excellent agreement between experiment and theory is found for  $V/V_0 \lesssim 0.65$ . Furthermore the linear relation between the shock velocities  $U_s$  and  $U_p$  was also calculated to be  $U_s = 3.0179 \text{ km/s} + 1.626U_p$ , which is in reasonable agreement with the experimental relation  $U_s = 3.12 \text{ km/s} + 1.521U_p$  [61].

So by comparing the experimental and theoretical Hugoniots the quality of the calculation can be checked without any assumptions regarding pressure calibration. However the high pressure part of the experimental room temperature isotherm has to be calculated by subtracting the temperature induced pressure from the Hugoniot

$$P_0(V) = P_{Hugoniot}(V) - (P_T(T) - P_T(298K)), \quad (8.37)$$

where  $P_T$  is a parameterization of the temperature pressure using some pressure standard and  $T$  is the temperature behind the shock wave. In Fig. 6 of

paper III calculated temperature pressures are displayed for two different volumes.

## 8.6 Thermal expansion

In this section the art of calculating thermal expansion coefficients from first principles will be discussed. This discussion will be based on the work done in papers IV and VI of the thesis.

### 8.6.1 Thermal expansion of cubic metals

The calculation of the thermal expansion of elements with cubic symmetry is very straightforward when done in the quasi harmonic approximation. First the phonon and electron density of states together with static lattice energy is calculated for a number of volumes around the  $T = 0K$  equilibrium volume. Then using Eq. (8.28-8.30) the total free energy is calculated for the different volumes at constant temperature and fitted to some EOS. In the case of paper VI the Vinet EOS [62]

$$\begin{aligned} F(V) &= \frac{4V_0 B_T}{(B' - 1)^2} \left[ 1 - (1 + x)e^{-x} \right], \\ x &= \frac{3}{2}(B' - 1) \left[ \left( \frac{V}{V_0} \right)^{1/3} - 1 \right], \end{aligned} \quad (8.38)$$

was used. Here the parameters are the equilibrium volume  $V_0$ , the isothermal bulk modulus  $B_T$  and its pressure derivative  $B'$ . Once the fit of the free energy is calculated, the equilibrium volume is obtained, and by repeating the process for different temperatures the thermal expansion coefficient  $\alpha$  defined by

$$\alpha \equiv \frac{1}{a} \frac{da}{dT} = \frac{1}{3V} \frac{dV}{dT} \quad (8.39)$$

can be calculated. Here  $a$  is the lattice constant. In Fig. 8.6 and 8.7 the thermal expansions and phonon dispersions of the 4d cubic metals calculated in paper VI are displayed together with experimental data. Here good agreement can be found between experiment and theory, both for the phonon dispersions and the thermal expansion in the case of the fcc metals. However, in the case of the bcc 4d metals, only the phonon dispersions show good agreement with experiment, the thermal expansion is found to deviate with up to 30 %.

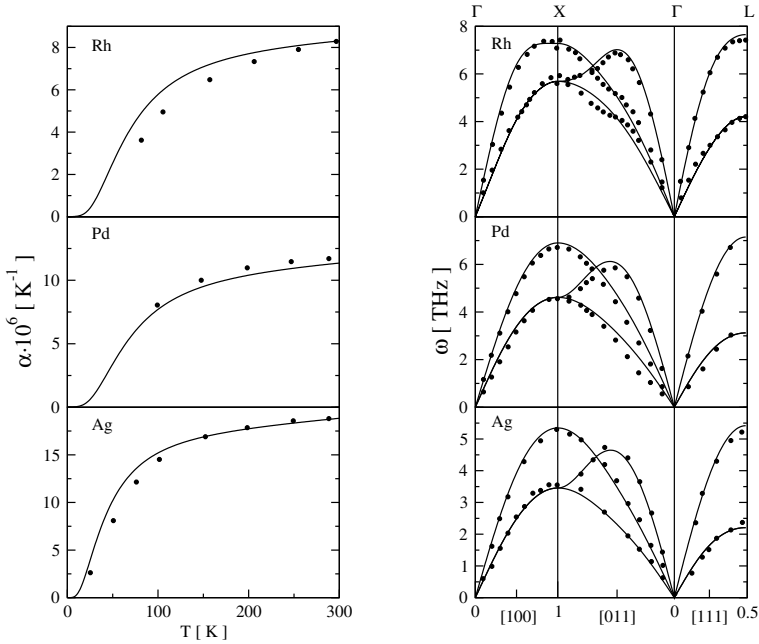


Figure 8.6: Theoretical and experimental thermal expansions and phonon dispersions for the fcc 4d metals. In the left column the thermal expansions and in the right column the phonon dispersions. The solid lines corresponding to the calculation of paper VI, the solid circles for the thermal expansion are the experimental data of Ref. [63] and for the phonon dispersions the experimental data of Ref. [64, 65, 66].

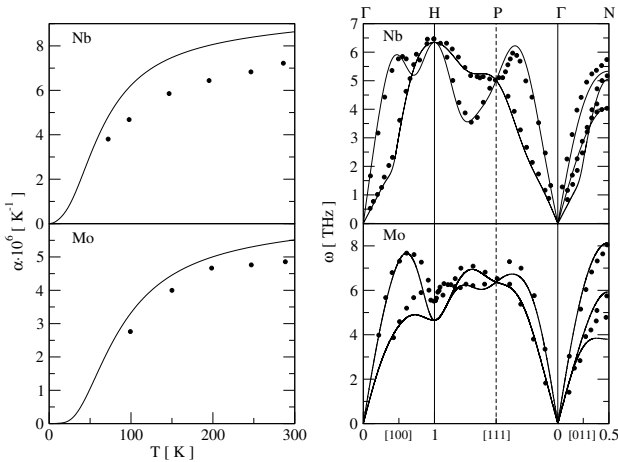


Figure 8.7: Theoretical and experimental thermal expansions and phonon dispersions for the bcc 4d metals. In the left column the thermal expansions and in the right column the phonon dispersions. The solid lines corresponding to the calculation of paper VI, the solid circles for the thermal expansion are the experimental data of Ref. [63] and for the phonon dispersions the experimental data of Ref. [67, 68].

## 8.6.2 Thermal expansion of hexagonal metals

To calculate the thermal expansion of hexagonal metals, the free energy and static lattice energy have to be parameterized with respect to two degrees of freedom. The most general second order parameterization of the free lattice energy, allowing only symmetry conserving strains, can be expressed with the six dimensional strain vector  $\bar{\varepsilon} = (\varepsilon_1, \varepsilon_1, \varepsilon_3, 0, 0, 0)$  and the elastic constants. Using this strain vector together with the definitions given in chapter 5, the static lattice energy  $U$ , accurate to second order in  $\varepsilon$ , can be expressed as

$$U(\varepsilon_1, \varepsilon_3) = \frac{V}{2} \left[ 2(C_{11} + C_{12})\varepsilon_1^2 + 4C_{13}\varepsilon_1\varepsilon_3 + C_{33}\varepsilon_3^2 \right], \quad (8.40)$$

where  $V$  is the zero temperature equilibrium volume. The strains  $\varepsilon_1$  and  $\varepsilon_3$  are related to the volume strain  $\varepsilon_v \equiv d\ln(V)/dV$  and tetragonal strain  $\varepsilon_c \equiv d\ln(c/a)/d(c/a)$  by the linear relations

$$\varepsilon_1 = \frac{1}{3}(\varepsilon_v - \varepsilon_c), \quad \varepsilon_3 = \frac{1}{3}(\varepsilon_v + 2\varepsilon_c) \quad (8.41)$$

Equation (8.40) together with Eq. (8.41) then gives the following parameterization of the free energy

$$F(\varepsilon_v, \varepsilon_c, T) = U(\varepsilon_v, \varepsilon_c) + F^{phon}(\varepsilon_v, \varepsilon_c, T) + F^{el}(\varepsilon_v, \varepsilon_c, T) \quad (8.42)$$

$$U(\varepsilon_v, \varepsilon_c) = V \left[ \frac{1}{2}B_{11}\varepsilon_v^2 + 2B_{12}\varepsilon_v\varepsilon_c + \frac{1}{2}B_{22}\varepsilon_c^2 \right] \quad (8.43)$$

where

$$B_{11} = \frac{2}{9}(C_{11} + C_{12} + \frac{1}{2}C_{33} + 2C_{13}) \quad (8.44)$$

$$B_{22} = \frac{2}{9}(C_{11} + C_{12} + 2C_{33} - 4C_{13}) \quad (8.45)$$

$$B_{12} = \frac{1}{9}(C_{33} + C_{13} - C_{11} - C_{12}) \quad (8.46)$$

$$(8.47)$$

By calculating the phonon and electron density of states for a number of volume strains (with  $\varepsilon_c = 0$ ) and a number of tetragonal strains (with  $\varepsilon_v = 0$ ), the free energy of the electron and phonon subsystems  $F^* = F^{phon} + F^{el}$  can be parameterized. Furthermore since  $F^*$  basically is linear both in  $\varepsilon_v$  and  $\varepsilon_c$ , the equilibrium strains  $\varepsilon_v^0$  and  $\varepsilon_c^0$  can be derived from the condition  $\nabla_{\varepsilon} F = 0$ , giving

$$\varepsilon_v^0(T) = \frac{1}{V(B_{11}B_{22} - B_{12}^2)} \left[ -B_{22} \frac{\partial F^*}{\partial \varepsilon_v} + B_{12} \frac{\partial F^*}{\partial \varepsilon_c} \right] \quad (8.48)$$

$$\varepsilon_c^0(T) = \frac{1}{V(B_{11}B_{22} - B_{12}^2)} \left[ B_{12} \frac{\partial F^*}{\partial \varepsilon_v} - B_{11} \frac{\partial F^*}{\partial \varepsilon_c} \right] \quad (8.49)$$

The linear relations (8.41) together with the above expression can then be used to express the thermal expansion coefficients as

$$\alpha_{\perp} = \frac{1}{3V(B_{11}B_{22} - B_{12}^2)} \left[ - (B_{22} + B_{12}) \frac{\partial^2 F^*}{\partial T \partial \varepsilon_v} + (B_{12} + B_{11}) \frac{\partial^2 F^*}{\partial T \partial \varepsilon_c} \right] \quad (8.50)$$

$$\alpha_{\parallel} = \frac{1}{3V(B_{11}B_{22} - B_{12}^2)} \left[ - (B_{22} - 2B_{12}) \frac{\partial^2 F^*}{\partial T \partial \varepsilon_v} + (B_{12} - 2B_{11}) \frac{\partial^2 F^*}{\partial T \partial \varepsilon_c} \right] \quad (8.51)$$

$$\beta = \frac{1}{V(B_{11}B_{22} - B_{12}^2)} \left[ -B_{22} \frac{\partial^2 F^*}{\partial T \partial \varepsilon_v} + B_{12} \frac{\partial^2 F^*}{\partial T \partial \varepsilon_c} \right], \quad (8.52)$$

where  $\alpha_{\perp} = \frac{d\varepsilon_1}{dT}$ ,  $\alpha_{\parallel} = \frac{d\varepsilon_3}{dT}$  and  $\beta = \frac{d\varepsilon_v}{dT}$ .

In Fig. 8.8 the results from paper VI are presented together with experimental data. For the hcp 4d metals good agreement between theory and experiment is found for all phonon dispersions. However, for the thermal expansion coefficients the situation is somewhat different. Here the best agreement between theory and experiment is found for the volume thermal expansion coefficients  $\beta$  in the temperature interval  $200 \text{ K} \lesssim T \lesssim 300 \text{ K}$ . Also the theoretical thermal expansion coefficients  $\alpha_{\perp}$  for Zr and Ru are in fairly good agreement with the experimental data for temperatures  $\gtrsim 100 \text{ K}$ . The biggest discrepancy between theory and experiment appears for the thermal expansion coefficient  $\alpha_{\parallel}$  in Zr. Not only is the theoretical prediction of  $\alpha_{\parallel}$  considerably smaller than the corresponding experimental data, but also negative for  $T \lesssim 75 \text{ K}$ . However, the experimental data for Zr displays some peculiar features, especially the thermal expansion coefficients  $\alpha_{\perp}$  and  $\beta$ , which show only the slightest variation across the entire temperature interval. Furthermore, if one would extrapolate the experimental  $\alpha_{\perp}$  and  $\beta$  along their respective tangents at  $T \sim 50 \text{ K}$  down to  $0 \text{ K}$ , they would be positive and considerably different from zero. A general property of all materials is that the thermal expansion coefficients should approach zero at  $T = 0 \text{ K}$ . This is the situation for hcp Ti which is iso-electronic to Zr. It is a matter of fact that hcp Ti has a general behaviour of  $\alpha_{\perp}$  and  $\alpha_{\parallel}$  (see paper IV) corresponding to the curves for Zr in Fig. 8.8. The lack of such behaviour in the experimental data of Zr suggests that the experimental thermal expansion data of Zr is indeed most peculiar, which may explain the difference between theory and experiment. The reason behind the negative thermal expansion coefficient  $\alpha_{\perp}$  of Zr will be theoretically explained in the next subsection.

In Fig. 8.9 the calculated linear thermal expansion  $\alpha = (\beta/3)$  at room temperature and ambient pressure is shown together with experimental data, for

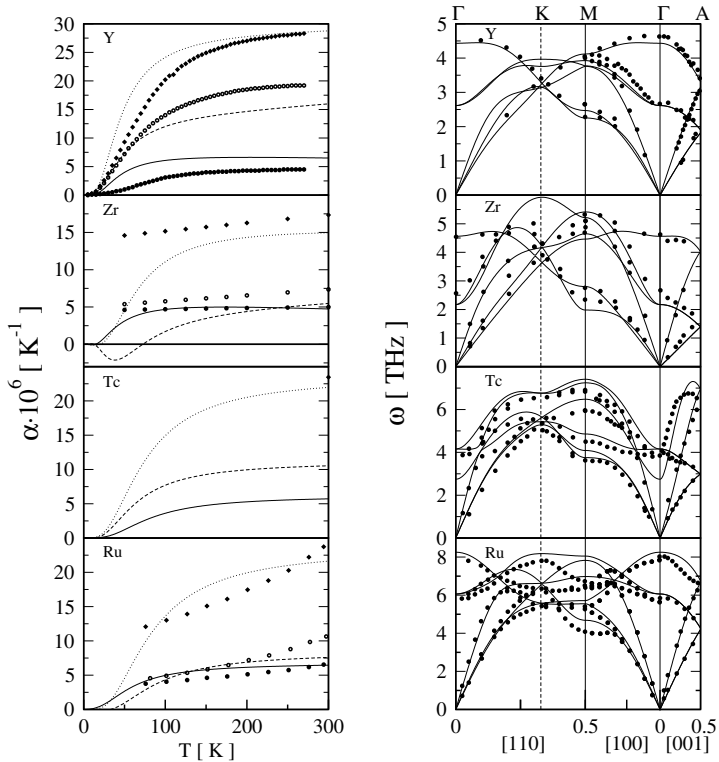


Figure 8.8: Theoretical and experimental thermal expansions and phonon dispersions for the hcp 4d metals. In the left column the thermal expansions and in the right column the phonon dispersions. The lines corresponding to the calculation of paper VI, the solid circles, empty circles and solid diamonds for the thermal expansion are the experimental  $\alpha_{\perp}$ ,  $\alpha_{\parallel}$  and  $\beta$  respectively of Ref. [69, 70, 71]. For the phonon dispersions the solid circles are the experimental data of Ref. [72, 73, 74, 75]. For the thermal expansion coefficients the solid line, dashed line and dotted line are the calculated thermal expansion coefficients  $\alpha_{\perp}$ ,  $\alpha_{\parallel}$  and  $\beta$  respectively.

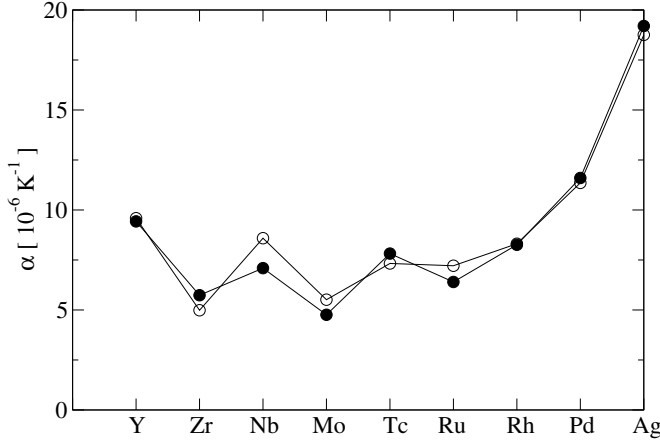


Figure 8.9: Linear thermal expansion for the 4d metals at room temperature and ambient pressure. The empty circles are the present calculation. The filled circles are the experimental data of Ref. [71]. For the hexagonal elements the polycrystalline expansion coefficients  $\alpha \equiv \beta/3$  are displayed.

all the 4d transition metals. Here it can be seen that theory manages to reproduce, not only qualitatively but also quantitatively, the trend of the thermal expansion across the entire 4d series.

## 8.7 Electronic topological transitions and thermal contraction

In this section it will be discussed how the closeness of the Fermi energy  $E_F$  to an electronic topological transition (ETT) affects the thermal expansion of hexagonal metals. An ETT occurs when the Fermi energy crosses a critical energy  $E_c$  for which the topology of the Fermi surface is drastically altered. In what follows two different types of ETTs and their effect upon the thermal expansion will be discussed. In Fig. 8.10 an example is shown of a saddle point topological transition calculated from the model electronic band structure

$$\varepsilon(\mathbf{k}) = E_c + E^* c^2 k_z^2 - E^* a^2 (k_x^2 + k_y^2), \quad (8.53)$$

Here  $\mathbf{k} = (k_x, k_y, k_z)$  is the band structure quantum number (k-point),  $E_c$  is the critical energy,  $E^*$ ,  $a$  and  $c$  are real parameters. The model band structure (8.53) can be used to calculate the features of the electronic density of states  $N(E)$  in the case when  $E$  is close to  $E_c$

$$N(E) = \frac{V}{4\pi^3} \int_{S(E)} \frac{dS}{|\nabla\varepsilon|} = \frac{1}{4\pi^2 |E^*|} \left[ \pi - \sqrt{\frac{E - E_c}{E^*}} \Theta\left(\frac{E - E_c}{E^*}\right) \right] \quad (8.54)$$



Figure 8.10: Fermi surfaces close to a saddle point topological transition, calculated with the model band structure given by Eq. 8.53 for  $E^* > 0$ . In the left surface  $E_F = 0.95E_c$ , in the middle  $E_F = E_c$  and in the right  $E_F = 1.05E_c$ .

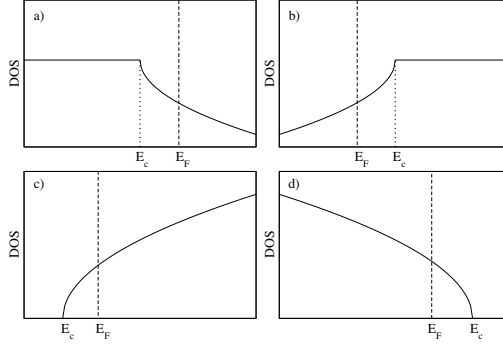


Figure 8.11: The different electronic density of states associated to ETTs corresponding to saddle point singularities, (a) and (b), and the appearance/disappearance of ellipsoidal surfaces, (c) and (d).

Here  $S(E) = \{\mathbf{k} \in \mathbf{R}^3 | \varepsilon(\mathbf{k}) = E\}$  and  $\Theta(x) = 1$  for  $x > 0$  and  $\Theta(x) = 0$  for  $x < 0$ . Similarly the model band structure given by

$$\varepsilon(\mathbf{k}) = E_c + E^* c^2 k_z^2 + E^* a^2 (k_x^2 + k_y^2), \quad (8.55)$$

describing an ETT associated with, as  $E$  is decreased towards  $E_c$ , the disappearance ( $E^* > 0$ ) or a appearance ( $E^* < 0$ ) of an ellipsoidal surface, give the following density of states

$$N(E) = \frac{V}{4\pi^3} \int_{S(E)} \frac{dS}{|\nabla \varepsilon|} = \frac{1}{4\pi^2 |E^*|} \sqrt{\frac{E - E_c}{E^*}} \Theta\left(\frac{E - E_c}{E^*}\right) \quad (8.56)$$

From the above results it is obvious that the presence of ETTs give rise to strong Van Hove singularities in the electronic density of states. In Fig. 8.11 the characteristic features of density of states corresponding to the Van Hove singularities associated to the ETTs are displayed. Whenever the Fermi level  $E_F$  is close to such a singularity the thermal expansion coefficients  $\alpha_{\perp}$  and  $\alpha_{\parallel}$  will be strongly effected by the strain derivatives of the electronic free energy. In order to make this statement plausible it is instructive to use the

Sommerfeld approximation (8.30) of the electronic free energy together with the expressions (8.54) and (8.55) which reveals

$$\frac{\partial^2 F^{el}}{\partial T \partial \varepsilon_v} = \pm \frac{k_B^2}{12(E^*)^{3/2}} \frac{T}{\sqrt{E_F - E_c}} \frac{\partial(E_F - E_c)}{\partial \varepsilon_v} \quad (8.57)$$

$$\frac{\partial^2 F^{el}}{\partial T \partial \varepsilon_c} = \pm \frac{k_B^2}{12(E^*)^{3/2}} \frac{T}{\sqrt{E_F - E_c}} \frac{\partial(E_F - E_c)}{\partial \varepsilon_c} \quad (8.58)$$

Here the upper sign corresponds to a saddle point van Hove singularity and the lower sign to an ellipsoidal singularity. Furthermore  $E^* > 0$  is assumed. From the above expressions it now becomes obvious that if  $E_F$  is close to a critical point, the effect of  $F^{el}$  upon the thermal expansion coefficients will be considerable. Let's assume that the Fermi level is close to a saddle point type of ETT and that a tetragonal strain  $\varepsilon_c$  moves the Fermi level away from the critical point  $E_c$ . Then if  $E_F - E_c$  decreases upon volume strain  $\varepsilon_v$  it becomes clear from (8.51) that the electronic contribution will give  $\alpha_{\perp} > 0$  and  $\alpha_{\parallel} < 0$ , whenever  $B_{11}, B_{22} \gg B_{12}$  and

$$\left| (B_{22} - 2B_{12}) \frac{\partial^2 F^{el}}{\partial \varepsilon_v \partial T} \right| < \left| (B_{11} - 2B_{12}) \frac{\partial^2 F^{el}}{\partial \varepsilon_c \partial T} \right| \quad (8.59)$$

Up to now attention has been paid only to the effect of the electronic free energy upon the thermal expansion coefficients. Certainly the main effect on the thermal expansion comes from the phonon part of the free energy. Thus without connecting the effects of an ETT to this part of the free energy no conclusions can be drawn upon how the thermal expansion is effected. In what follows a brief sketch of how an ETT effects the phonon part of the free energy will be given. Let  $g(E) = \bar{N}(E) + N(E)$  be the electronic density of states (DOS), where  $\bar{N}(E)$  is the non-singular part of the DOS and  $N(E)$  the contribution to the DOS coming from a saddle point van Hove singularity. Then the static lattice energy  $U$ , neglecting all coulomb contributions, can be written as

$$U = \int_0^{E_F} g(E) E dE = \bar{E} - \frac{1}{30\pi^2} \left[ \frac{E_F - E_c}{E^*} \right]^{3/2} (3E_c + 2E_F), \quad (8.60)$$

where  $\bar{E}$  is given by

$$\bar{E} = \int_0^{E_F} \bar{N}(E) E dE \quad (8.61)$$

Now from the above expression for the total energy it is possible to express the elastic constants  $C_{ij}$  to leading order in  $E_F - E_c$  as

$$C_{ij} = \frac{\partial^2 U}{\partial \varepsilon_i \partial \varepsilon_j} = \bar{G}_{ij} + G_{ij} \quad (8.62)$$

where

$$G_{ij} = -\frac{(E_F - E_c)^{-1/2}}{40\pi^2(E^*)^{3/2}} (3E_c + 2E_F) \frac{\partial(E_F - E_c)}{\partial \varepsilon_i} \frac{\partial(E_F - E_c)}{\partial \varepsilon_j} \quad (8.63)$$

$$\bar{G}_{ij} = \frac{\partial^2 \bar{E}}{\partial \varepsilon_i \partial \varepsilon_j} \quad (8.64)$$

Under the assumption that  $|\partial G_{ij}/\partial \varepsilon_k| \gg |\partial \bar{G}_{ij}/\partial \varepsilon_k|$  the strain derivatives of the elastic constant to leading order in  $E_F - E_c$  become

$$\frac{\partial C_{ij}}{\partial \varepsilon_k} = \frac{|G_{ij}|}{2(E_F - E_c)} \frac{\partial(E_F - E_c)}{\partial \varepsilon_k}. \quad (8.65)$$

The temperature derivative  $\partial F^{phon}/\partial T$  can at low temperatures be approximated with the Debye model using the phonon DOS  $g(\omega) = 9\omega^2/\omega_D^3$ , (here  $\omega_D$  is the Debye frequency)

$$\frac{\partial F^{phon}}{\partial T} = \frac{\partial}{\partial T} \int_0^{\omega_D} d\omega g(\omega) \left[ \frac{\hbar\omega}{2} + k_B T \ln \left[ 1 - e^{-\frac{\hbar\omega}{k_B T}} \right] \right] \approx -54 K_B \left( \frac{k_B T}{\hbar\omega_D} \right)^3, \quad (8.66)$$

Here it is assumed that  $k_B T \ll \hbar\omega_D$ . The average frequency  $\omega_D^2$  is here expressed as a linear combination of the elastic constants, i.e

$$\omega_D^2 = \gamma_1 C_{11} + \gamma_2 C_{22} + \gamma_3 C_{13} + \gamma_4 C_{13} + \gamma_5 C_{55}, \quad (8.67)$$

where  $\gamma_i$  are real expansion coefficients. Now the strain derivatives of  $\partial F^{phon}/\partial T$  can with the help of Eq. (8.65-8.67) be given the following form

$$\begin{aligned} \frac{\partial^2 F^{phon}}{\partial T \partial \varepsilon_k} &= \frac{162 k_B}{\omega_D} \left( \frac{K_B T}{\hbar\omega_D} \right)^3 \frac{\partial \omega_D}{\partial \varepsilon_k} = \\ &= \left( \frac{k_B T}{\hbar\omega_D} \right)^3 \left( \frac{\bar{\omega}}{\omega_D} \right)^2 \frac{81 k_B}{(E_F - E_c)} \frac{\partial(E_F - E_c)}{\partial \varepsilon_k}. \end{aligned} \quad (8.68)$$

where

$$\bar{\omega}^2 = \gamma_1 |G_{11}| + \gamma_2 |G_{22}| + \gamma_3 |G_{13}| + \gamma_4 |G_{13}| + \gamma_5 |G_{55}| \quad (8.69)$$

Finally comparing the Eq. (8.68) with the corresponding expressions for the electronic free energy (8.57) and (8.58), it becomes clear that the van Hove singularities affect the phonon contribution to the thermal expansion coefficients in such a way that

$$\frac{\partial^2 F^{phon}}{\partial T \partial \varepsilon_k} = \frac{972(E^*)^{3/2}}{k_B T \sqrt{E_F - E_c}} \left( \frac{k_B T}{\hbar\omega_D} \right)^3 \left( \frac{\bar{\omega}}{\omega_D} \right)^2 \frac{\partial^2 F^{el}}{\partial T \partial \varepsilon_k}. \quad (8.70)$$

From the relation (8.70) it can be seen that at relatively low temperatures, and when the Fermi energy is close enough to an ETT, the thermal expansion emanating from the phonon contribution follows the thermal expansion related to the electronic contribution! This is a very powerful property of the ETTs, which can be used to predict anomalous behaviour of the low temperature thermal expansion coefficients without ever calculating a single phonon. A much more rigorous derivation on the effect that van Hove singularities have on the phonon part of the free energy is given in the paper by Katsnelson *et al* [76].

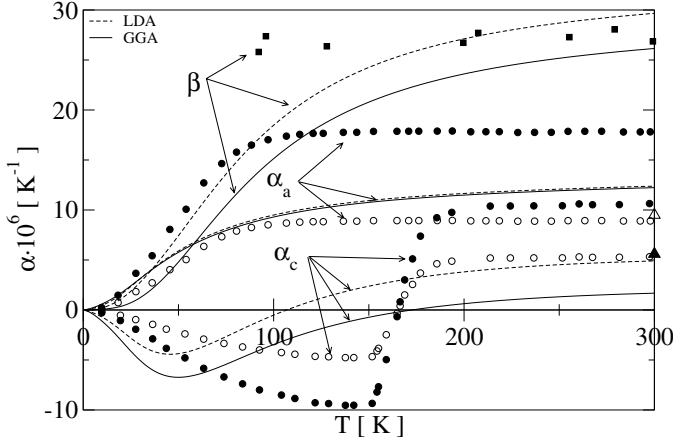
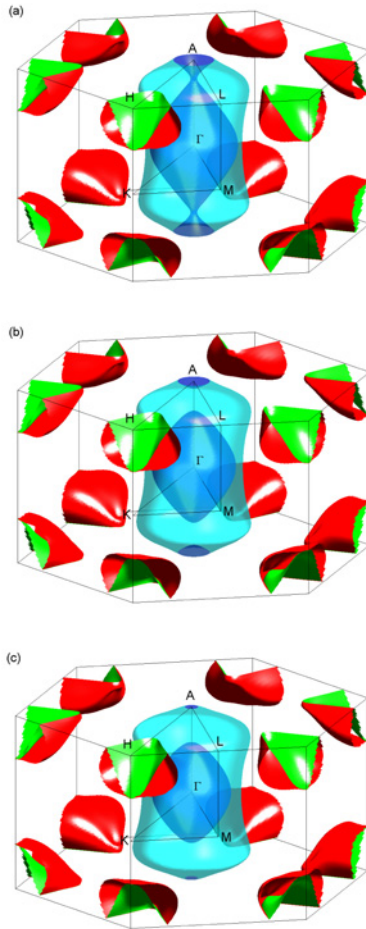


Figure 8.12: Linear thermal expansion for hcp Ti at ambient pressure. The solid lines are the theoretical calculation using GGA and the dashed line is from an LDA calculation. The filled circles are the experimental data of Nizhankovskii *et al* [77]. The filled squares are the experimental volume expansion coefficient of Mal'ko *et al* [78]. The filled and empty triangle are the experimental data of  $\alpha_a$  and  $\alpha_c$  respectively of Ram *et al* [79]. The empty circles are the experimental data of Nizhankovskii *et al* scaled to give a volume expansion coefficient in agreement with Ref.[78].

In paper IV the thermal expansion coefficients of hcp titanium were calculated from first principles. In Fig. 8.12 the calculated thermal expansion coefficients of hcp Ti are displayed together with experimental data. Here the most striking feature is that the thermal expansion coefficient  $\alpha_{||}$  along the c-axis is negative for  $T \lesssim 175K$ . Furthermore, in paper IV the Fermi surface of hcp Titanium was also calculated for different tetragonal and volume strains. In Fig. 8.13 the calculated Fermi surfaces of hcp Ti for three different tetragonal strains are displayed. Here as the c-axis is decreased, a clear electronic topological transition can be observed. The two Fermi surface sheets, one rugby ball shaped around the  $\Gamma$ -point and one disc shaped at the A-point, get connected by a neck upon compression along the c-axis. From the previous discussion it is clear that the Fermi energy of Ti lies close to a critical energy point  $E_{c1}$  corresponding to saddle point type ETT. The observation of a saddle point ETT in the vicinity of  $E_F$  together with the calculated derivatives  $\partial N(E_F)/\partial \epsilon_v \sim 0.75 \text{ eV}^{-1}$  and  $N(E_F)/\partial \epsilon_c \sim -0.77 \text{ eV}^{-1}$ , led to the conclusion that the negative thermal expansion coefficient  $\alpha_{||}$  along the c-axis must be the result of  $E_F$  being close to a saddle point ETT.

Finally, in connection to the previously presented calculations of hcp Zr (see Fig. 8.7), it should be mentioned that the calculated negative  $\alpha_{||}$  for  $T \lesssim 50K$  also can be connected to a saddle point ETT. The calculated Fermi surfaces of hcp Zr for different tetragonal strains show exactly the same features as those of hcp Ti. The Fermi surfaces of Zr are presented in appendix A.



*Figure 8.13:* Calculated Fermi surface of hcp Ti at  $T=0$  equilibrium volume for three different lattice constants  $c$ , at  $c = 0.988c_0$  (a), at  $c = c_0$  (b) and at  $c = 1.012c_0$  (c). Here  $c_0$  corresponds to the ( $T=0$ ) equilibrium lattice constant.

## 8.8 The self-consistent ab initio lattice dynamical method

In this the final part of the thesis the self-consistent ab initio lattice dynamical method (SCAILD) will be presented. But before this method is presented the background motivation for developing the SCAILD method will be discussed.

### 8.8.1 The anharmonic lattice

Up to this section all phonon calculations presented in this thesis have been done within the quasi harmonic approximation. In this approximation the only temperature dependence taken into account is the force constants  $\bar{\Phi}$  dependence upon the thermal expansion. All other anharmonic contributions to the temperature dependence of the phonons, such as the terms of order greater than 2 in the Taylor expansion of the potential energy (8.1), are neglected. However, as the temperature increases the thermally induced displacements  $U_{\mathbf{R}}$  become bigger and bigger, and the anharmonic terms in the lattice dynamical Hamiltonian (8.1) cannot longer be neglected. To illustrate this it is instructive to look at the expression for the mean square deviation of the atoms  $\langle U^2 \rangle$  from their  $T = 0$  positions (here given in the harmonic approximation)

$$\langle U^2 \rangle = \frac{1}{N} \sum_{\mathbf{R}} \langle U_{\mathbf{R}}^2 \rangle = \int_0^\infty d\omega g(\omega) \frac{\hbar}{M\omega} \left[ \frac{1}{2} + \bar{n} \left( \frac{\hbar\omega}{k_B T} \right) \right] \quad (8.71)$$

Furthermore there are situations such as the high temperature bcc phase of many elemental metals (Ti, Hf, Zr, La,...) where harmonic lattice theory fails miserably even at low temperatures. In these cases a standard phonon calculation performed within the harmonic approximation yields imaginary phonon frequencies. This is a result of the lattice being unstable with respect to the periodic atomic motion in which the atoms move along the eigenvectors  $\epsilon_{\mathbf{k}_s}$  corresponding to the imaginary frequencies. Thus the atoms will move away from their local energy maxima/saddle points into positions corresponding to a energetically more stable structure. In Fig. 8.14 the results of a harmonic phonon calculation for bcc Zr are shown together with a schematic plot of the potential energy as a function of displacement amplitude for the  $T_1$  N-point phonon. Here the failure of the harmonic approximation is obvious with imaginary frequencies not only along the  $\Gamma$  to  $N$  direction but also around the  $P$  symmetry point.

One of the first to ponder upon the enigma of the occurrence of high temperature bcc phases in nature was Zener [6]. He argued that the mechanically unstable ( at  $T = 0K$ ) bcc phase at high temperatures got stabilized by entropy. However, in the harmonic approximation the force constants are completely inert to all entropy effects. The only way to incorporate the effect of entropy is to go beyond the harmonic approximation and take into account the anharmonic terms in the lattice dynamical Hamiltonian 8.1. These anharmonic

terms describe the phonon-phonon interaction which is the mediator of entropy effects. One way to incorporate the effect of entropy into a phonon calculation is to start by substituting  $\mathbf{P}_{\mathbf{R}}$  and  $\mathbf{U}_{\mathbf{R}}$  in the lattice dynamical Hamiltonian (8.1) with the right hand expressions of Eqn. (8.3) and (8.6), to obtain the following

$$\mathcal{H} = \frac{1}{2} \sum_{\mathbf{k}s} \left[ \mathcal{P}_{\mathbf{k}s}^2 + \omega_{\mathbf{k}s}^2 \left( 1 + \frac{1}{3} \sum_{\mathbf{k}_1, \mathbf{k}_2, s_1, s_2} \mathcal{A}(\mathbf{k}, \mathbf{k}_1, \mathbf{k}_2, s, s_1, s_2) \frac{\mathcal{Q}_{\mathbf{k}_1 s_1} \mathcal{Q}_{\mathbf{k}_2 s_2}}{\mathcal{Q}_{\mathbf{k}s} \omega_{\mathbf{k}s}^2} + \dots \right) \mathcal{Q}_{\mathbf{k}s}^2 \right] \quad (8.72)$$

where

$$\mathcal{A}(\mathbf{k}, \mathbf{k}_1, \mathbf{k}_2, s, s_1, s_2) = \frac{1}{(MN)^{3/2}} \sum_{\mathbf{R}, \mathbf{R}_1, \mathbf{R}_2} \sum_{\alpha, \beta, \gamma} \Phi_{\alpha\beta\gamma}(\mathbf{R}, \mathbf{R}_1, \mathbf{R}_2) \epsilon_{\mathbf{k}s\alpha} \epsilon_{\mathbf{k}_1 s_1 \beta} \epsilon_{\mathbf{k}_2 s_2 \gamma} e^{i(\mathbf{R}\mathbf{k} + \mathbf{R}_1 \mathbf{k}_1 + \mathbf{R}_2 \mathbf{k}_2)} \quad (8.73)$$

The first obvious thing about the Hamiltonian  $\mathcal{H}$  is that it is not separable into independent Hamiltonians. Nevertheless assuming that the frequencies  $\omega_{\mathbf{k},s}$  and their respective eigenvectors have been taken from a harmonic calculation of the same system, and that the temperature is sufficiently high to permit the operators  $\mathcal{Q}_{\mathbf{k}s}$  to be replaced with real numbers

$$\mathcal{Q}_{\mathbf{k}s} \approx \pm \sqrt{\langle \mathcal{Q}_{\mathbf{k}s}^2 \rangle} = \pm \sqrt{\frac{\hbar}{\omega_{\mathbf{k}s}} \left[ \frac{1}{2} + \bar{n} \left( \frac{\hbar \omega_{\mathbf{k}s}}{k_B T} \right) \right]} \quad (8.74)$$

the Hamiltonian (8.72) can be used to create the meanfield Hamiltonian

$$\mathcal{H}^{MF} = \sum_{\mathbf{k}s} \frac{1}{2} (\mathcal{P}_{\mathbf{k}s}^2 + \bar{\omega}_{\mathbf{k}s}^2 \mathcal{Q}_{\mathbf{k}s}^2) \quad (8.75)$$

where<sup>1</sup>

$$\bar{\omega}_{\mathbf{k}s}^2 = \omega_{\mathbf{k}s}^2 \left( 1 + \frac{1}{2} \sum_{\mathbf{k}_1, \mathbf{k}_2, s_1, s_2} \mathcal{A}(\mathbf{k}, \mathbf{k}_1, \mathbf{k}_2, s, s_1, s_2) \frac{\mathcal{Q}_{\mathbf{k}_1 s_1} \mathcal{Q}_{\mathbf{k}_2 s_2}}{\mathcal{Q}_{\mathbf{k}s} \omega_{\mathbf{k}s}^2} + \dots \right) \quad (8.76)$$

The system of equations (8.74-8.76) can, once an initial guess has been provided by a harmonic calculation and the coefficients  $\mathcal{A}(\mathbf{k}, \mathbf{k}_1, \mathbf{k}_2, s, s_1, s_2), \dots$  have been calculated, be solved self-consistently. These equations are the phonon equivalent of the Hartree-Fock equations and they demonstrate the basic principle of the SCAILD method.

---

<sup>1</sup>See Appendix B

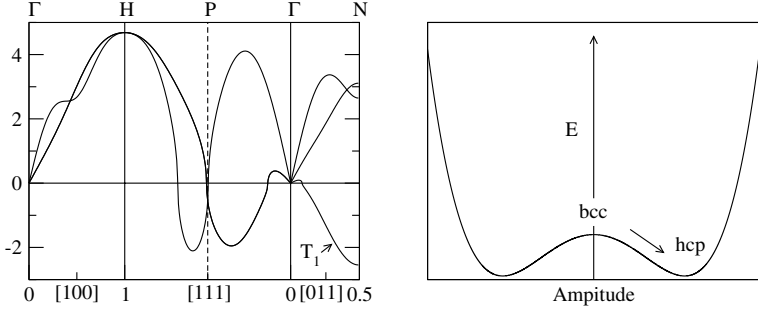


Figure 8.14: To the left the bcc Zr phonon dispersion calculated with the harmonic approximation. To the right a schematic plot of the potential energy as a function of displacement amplitude for the  $T_1$  N-point phonon of bcc Zr. The arrow in the right plot does not point towards the real energy minimum of the hcp structure. However the movement of atomic planes along the eigenvector of the  $T_1$  N phonon is taking part in the bcc to hcp transformation path.

## 8.8.2 The self-consistent cycle

The SCAILD method is a novel method developed for solving the equations (8.74-8.76) in a self-consistent manner. The SCAILD method utilizes the supercell technique (see section 7.3) to calculate the contribution to  $\bar{\omega}_{\mathbf{k}s}$  from the interaction terms  $\mathcal{A}(\mathbf{k}, \mathbf{k}_1, \mathbf{k}_2, s, s_1, s_2), \dots$  in (8.76). This is not done by an explicit calculation of the phonon-phonon interaction terms, instead the effect of these terms is implicitly calculated by exciting all the lattice waves with  $\mathbf{k}$ -vectors commensurate with the supercell that has been chosen for the calculation. The superposition of these lattice waves will stipulate atomic displacements in the supercell

$$\mathbf{U}_{\mathbf{R}} = \frac{1}{\sqrt{N}} \sum_{\mathbf{k}, s} \mathcal{R}_{\mathbf{k}s} \boldsymbol{\epsilon}_{\mathbf{k}s} e^{i\mathbf{k}\mathbf{R}}. \quad (8.77)$$

where the operators  $\mathcal{Q}_{\mathbf{k}s}/\sqrt{M}$  in (8.3) have, under the assumption that the system is within the classical limit, been replaced by the numbers given by

$$\mathcal{R}_{\mathbf{k}s} = \pm \sqrt{\frac{\langle \mathcal{Q}_{\mathbf{k}s}^2 \rangle}{M}} = \pm \sqrt{\frac{\hbar}{\omega_{\mathbf{k}s} M} \left[ \frac{1}{2} + \bar{n} \left( \frac{\hbar \omega_{\mathbf{k}s}}{k_B T} \right) \right]} \quad (8.78)$$

The Hellman-Feynman forces on the atoms  $\mathbf{F}_{\mathbf{R}}$  can then be calculated with some ab initio code

$$\mathbf{F}_{\mathbf{R}} = - \sum_{\mathbf{R}'} \bar{\Phi}^{MF}(\mathbf{R} - \mathbf{R}') \mathbf{U}_{\mathbf{R}'}. \quad (8.79)$$

where  $\bar{\Phi}^{MF}$  is the mean-field force constants given by

$$\bar{\Phi}_{\alpha\beta}^{MF}(\mathbf{R} - \mathbf{R}') = \bar{\Phi}_{\alpha\beta}(\mathbf{R} - \mathbf{R}') + \frac{1}{2} \sum_{\mathbf{R}', \mathbf{R}''} \Phi(\mathbf{R}, \mathbf{R}', \mathbf{R}'')_{\alpha\beta\gamma} U_{\mathbf{R}'\gamma} + \dots \quad (8.80)$$

Fourier transforming Eqn. 8.79 and substituting  $\mathbf{U}_R$  with the expression in Eqn. 8.77 gives

$$\mathbf{F}_k = - \sum_s M \bar{\omega}_{k_s}^2 \mathcal{R}_{k_s} \boldsymbol{\varepsilon}_{k_s}. \quad (8.81)$$

Finally, using the orthogonality of the eigenvectors  $\boldsymbol{\varepsilon}_{k_s}$  the phonon frequencies can be expressed as

$$\bar{\omega}_{k_s}^2 = - \frac{1}{M} \frac{\boldsymbol{\varepsilon}_{k_s} \mathbf{F}_k}{\mathcal{R}_{k_s}}. \quad (8.82)$$

From the above discussion it is now simple to construct the self-consistent cycle used in the SCAILD method for solving the system of equations (8.74-8.76), namely:

1. In the initializing step a standard supercell calculation is used to calculate the frequencies  $\omega_{k_s}$  and eigenvectors  $\boldsymbol{\varepsilon}_{k_s}$ .
2. The frequencies  $\omega_{k_s}$  and eigenvectors  $\boldsymbol{\varepsilon}_{k_s}$  are here used together with Eqn. 8.77 and 8.78 to calculate the displacements  $\mathbf{U}_R$  of the atoms of the supercell. Here the +/- signs in 8.78 are chosen randomly with equal probability for either sign.
3. The Hellman-Feynman forces are calculated on the displaced atoms of the supercell by some ab initio code.
4. From the Fourier transform of the forces through Eqn. 8.82 a new set of eigenvalues  $\bar{\omega}_{k_s}^2$  are calculated.
5. From the new eigenvalues of step 4 a set of symmetry restored frequencies are calculated

$$\Omega_{k_s}^2 = \frac{1}{m_k} \sum_{S \in S(\mathbf{k})} \bar{\omega}_{S^{-1}k_s}^2, \quad (8.83)$$

where  $S(\mathbf{k})$  is the symmetry group of the wave vector  $\mathbf{k}$ , and  $m_k$  the number of elements of the group. The mean value of all iterations supplies a new set of frequencies,

$$\omega_{k_s}^2(N) = \frac{1}{N} \sum_{i=1}^N \Omega_{k_s}^2(i), \quad (8.84)$$

where  $\Omega_{k_s}(i)$ ,  $i = 1, \dots, N$  are the symmetry restored frequencies from all iterations. The new set of frequencies calculated in (8.84) are then used in step 2 to calculate a new set of displacements, and the cycle is continued until self-consistency is reached.

In Fig. 8.15 a schematic outline is shown of the different steps performed in a SCAILD calculation.

Before going to the next section, where some of the results obtained with the SCAILD method are presented, it should be stressed that the implicit calculation of the k-point sums in (8.76) are approximate. The exact values of these sums are only reached in the limit of infinite supercell size, since these sums only include wavevectors commensurate with the supercell.

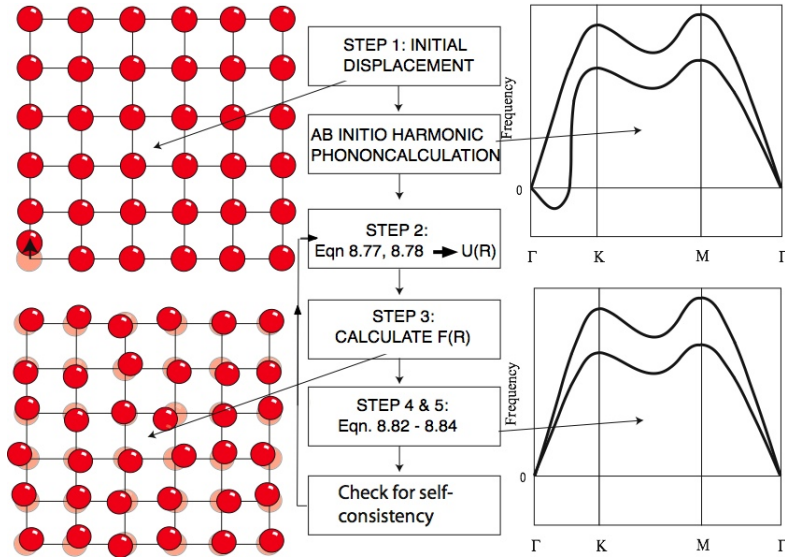


Figure 8.15: Schematic outline over the different tasks performed in a self-consistent phonon calculation.

### 8.8.3 Results

In this the final subsection some of the tests and results on the SCALD method will be presented. Most of the calculations have been made on the group IV elements, Ti, Zr and Hf, both for the hcp and bcc structures at elevated temperatures. The inter atomic forces in the calculations have been calculated both from first principles and from embedded atom potentials (EAP). For details concerning the EAPs, see appendix C. The results of the ab initio calculations are taken from paper V of this thesis.

Figure 8.16 shows the calculated phonon dispersions together with the experimental data of Ref. [80, 81, 82] for the bcc phase of the group IV B metals at temperatures 1293 K, 1188 K, and 2073 K for Ti, Zr, and Hf, respectively. The finite temperature calculations predict the stability of the bcc phase of all group IV B metals by promoting the frequencies of the phonons along the  $\Gamma$  to  $N$  symmetry line and around the  $P$  symmetry point from imaginary to real. The finite temperature phonon calculations result in an overall quantitative agreement with experimental values. Smaller deviations are observed around the P and H point of the Brillouin-zone, most likely due to finite size effects of the supercell used in the calculations. From the self-consistent phonon spectrum the free energy is approximated from the density of states of the phonon DOS  $g(\omega)$  through the expression (8.28). Figure 8.17 shows the convergence of free energy, as a function of the number of iterations, for the three elements considered. In all calculations presented here the self-consistent cycle was terminated when the difference in the approximate free energy of the lat-

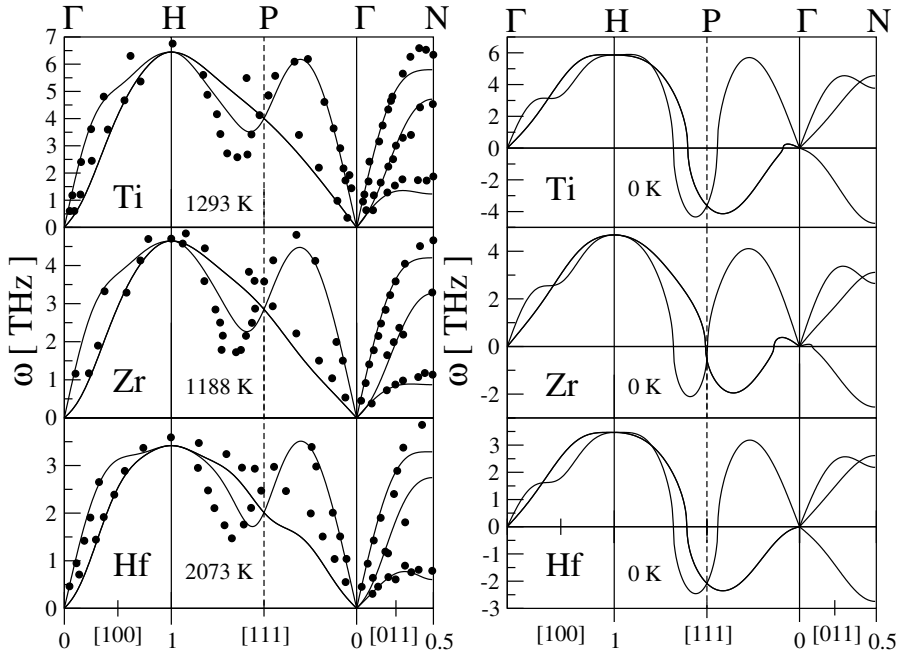


Figure 8.16: The phonon dispersions of the group IV B metals. The solid lines are the first principles self-consistent phonon calculations. In the left column the finite temperature calculations, and in the right column the  $T = 0$  K calculations. The filled circles are the experimental data of Ref. [80, 81, 82].

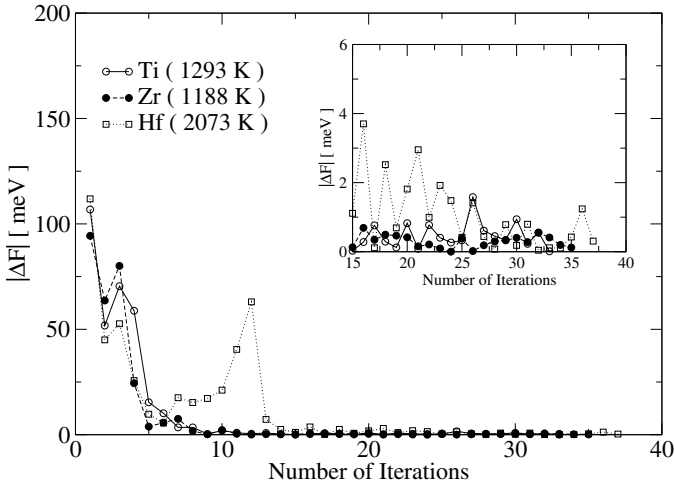


Figure 8.17: The change in free energy between two consecutive iterations, here plotted as a function of the number of iterations. The inset in the figure shows the same plots but at a smaller energy scale.

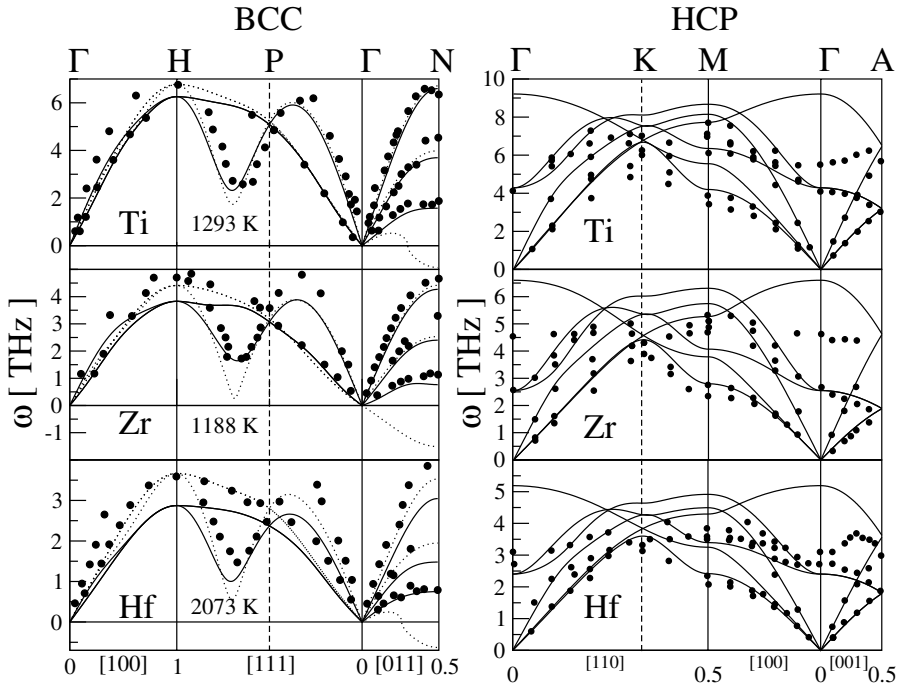


Figure 8.18: The phonon dispersions of the group IV B metals. The solid lines are the SCAILD calculations using EAP potentials. In the left column the finite temperature calculations for the bcc structure, and in the right column the  $T = 0$  K calculations for the hcp structure. The filled circles are the experimental data of Ref. [80, 81, 82] and Ref. [73, 85, 86] for the bcc and hcp structures respectively.

tice between two consecutive iterations was less than 1 meV. Convergence in the free energy with such accuracy is very encouraging and opens up the possibility to investigate temperature induced phase stability for a very large set of materials, since the accuracy needed to e.g. resolve crystallographic energy differences is of the order of a few meV. In a preliminary test of the SCAILD method, EAP model potentials were used together with the SCAILD method to calculate the free energy difference between the hcp and bcc structure for the group IV metals. The calculations were done at ambient pressure using the EAP potentials of Pasianot *et al* [83, 84], and the supercell sizes used were  $4 \times 4 \times 4$  and  $4 \times 4 \times 3$  for the bcc and hcp structures respectively. In appendix C a description of these potentials is given together with their respective parameters. Figure 8.18 (left column) shows the phonon dispersions calculated with the EAP potentials together with the experimental data of Ref. [80, 81, 82] for the bcc phase of the group IV A metals at elevated temperatures. In the same figure (right column) the phonon dispersions calculated with EAP potentials

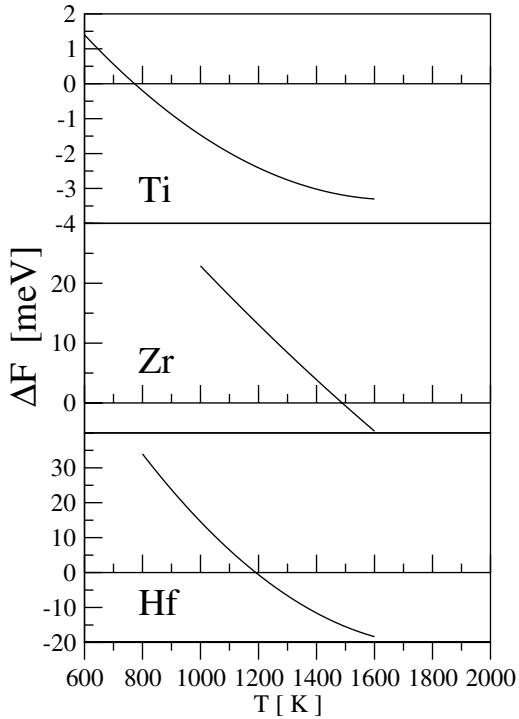


Figure 8.19: The calculated difference in free energy  $\Delta F = F(bcc) - F(hcp)$ , using EAP potentials, between the hcp and bcc structure of the group IV metals

together with the experimental data of Ref. [73, 85, 86] for the hcp phase of the group IV A metals is also shown. Here the calculated hcp phonon dispersions have been done at  $T=0K$ , i.e the standard supercell method has been used. By calculating the phonon density of states for different volumes and for different temperatures, the approximate free energy was calculated by means of (8.28) for the hcp and bcc structure of the group IV metals. It should be stressed that the SCAILD scheme was also used when the free energy for the hcp structure was calculated. In Figure. 8.19 the calculated free energy difference between the hcp and bcc structure is shown. The calculated transition temperatures are displayed together with experimental data in table 8.1. Here the agreement between experiment and theory is acceptable for Ti and Zr, while for Hf the theoretical transition temperature is almost 900K lower then the experimental transition temperature. The poor agreement is of course expected since only model potentials have been used, but at least these preliminary tests show that the SCAILD method in principle can be used to predict temperature induced phase transitions.

As previously mentioned, the size of the supercell used in a SCAILD calculation also determines the size of the k-point mesh for the implicitly calculated sums in equation (8.76). Thus it is also important to check the convergence of

	$T_c^{th}[K]$	$T_c^{ex}[K]^a$
<i>Ti</i>	773	1155
<i>Zr</i>	1489	1135
<i>Hf</i>	1191	2015

Table 8.1: Theoretical and experimental temperatures for which the  $\alpha$  to  $\beta$  transition takes place in the group IV B metals. <sup>a</sup>The experimental data are from Ref. [80, 81, 82].

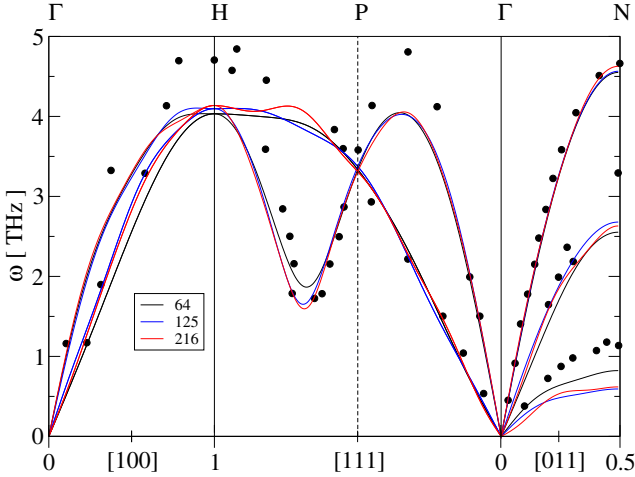


Figure 8.20: Phonon dispersions of bcc Zr calculated with the SCAILD method and the EAP potential of Ref. [84]. The black line is the calculation with a 64 atom supercell, the blue line is the calculation with a 125 atom supercell and the red line is the calculation with a 216 atom supercell. All three calculations have been made with the same lattice constant at  $T=1188$  K. The solid circles are the experimental data of Ref. [85].

the phonon frequencies with respect to increasing supercell size. This has been done by calculating the phonon frequencies for bcc Zr at  $T=1188$  K for three different supercell sizes 64 atoms, 125 atoms and 216 atoms. Here the EAP potentials of Ref. [84] were used together with the SCAILD scheme. In Fig. 8.20 the results of these tests are shown. Furthermore, the difference in free energy between the 64 atom calculation and the other two calculations is  $\lesssim 1$  meV.

This section is ended by concluding that the SCAILD method has proven Zener's old assumption [6] to be true in the case of the high temperature bcc phase of Ti, Zr and Hf. Furthermore, it has also been shown that the SCAILD method could be used to calculate free energy differences between different crystallographic phases.



## 9. Summary and outlook

The work of this thesis has been focused on three of the main areas of condensed matter theory, namely; materials design, testing of the limitations of DFT calculations and development of new theoretical tools to be used together with DFT calculations. Chapter 6 and 7 were concerned with materials design issues, where the attempts to remedy the brittle behaviour of the recently discovered super conductor  $MgB_2$  [1], together with theoretical predictions of superplastic transition metal alloys were discussed. In chapter 8 the limitations of DFT calculations of lattice dynamical properties together with the development of the new theoretical SCAILD tool were discussed.

In the case of  $MgB_2$  it was found that the introduction of Aluminum suppressed the elastic anisotropy of the superconductor but not to the extent that the material became ductile. Thus the large scale use of  $MgB_2$  has to wait until future research comes up with a solution to the brittleness of the material. Perhaps the problem can be solved by doping with elements other than those in the neighboring periods of Mg. However, this implies that in future theoretical studies the VCA approximation utilized in chapter 6 has to be replaced by more sophisticated methods such as the coherent potential approximation (CPA). The studies of the superplastic transition metal alloys presented in chapter 7 showed that Fe-Co, Mo-Tc and W-Re alloys were plausible candidates for having a vanishingly low  $C'$  elastic constant. However, it was also shown that these alloys become unstable relative to the hcp and fcc phases before the alloying concentration reaches the critical point where the superplastic transition occurs, suggesting that other elements have to be added to stabilize the bcc structure. Hence for future studies of superplastic transition metal alloys, more elaborate methods such as CPA have to be used to find ways to stabilize the bcc structure of the alloys discussed in chapter 7.

In testing the predictive power of DFT calculations the phonon dispersions and thermal expansions of the 4d transition metals were calculated. Here it was found that the calculated phonon dispersions and thermal expansion coefficients of the fcc metals showed the best agreement with experiment. In the case of the hcp 4d metals the calculated phonon dispersions showed reasonable agreement with experiment, while for the hcp thermal expansion coefficients the best agreement between theory and experiment could be found for the volume thermal expansion at  $T \gtrsim 200$  K. For the bcc 4d metals the calculated phonon dispersions showed reasonable agreement with experiment while the calculated thermal expansion coefficients showed an overall less ac-

curate agreement. The results of these tests show that not only a more elaborate parameterization of the static lattice energy in the case of the hcp metals, taking into account anharmonic contributions, but also bigger supercells to avoid finite size effects have to be used in order to increase the accuracy of calculated thermal expansion coefficients and phonon frequencies of the bcc and hcp transition metals. Furthermore the high accuracy in the calculation of the EOS of Au presented in chapter 8 added further support to the doubts concerned with the old ruby pressure scale. The thermal expansion calculations of  $\alpha$ -Ti presented in the same chapter showed that the reason behind the negative thermal expansion along the c-axis was the closeness of the Fermi level to a saddle point ETT. This finding in itself is very interesting, but it also illustrates a mechanism suggesting the existence of non-magnetic invar alloys.

Finally the preliminary tests of the SCAILD have perhaps proved Zener's [6] old argument, pointing out the entropy as the main stabilization factor of the high temperature bcc phase of Ti, Zr and Hf. Furthermore the energy resolution of  $\lesssim 1$  meV of the method shows great promise in being able to predict free energy differences as a function of temperature between different crystallographic phases. Hence due to limited number of atoms needed ( $\lesssim 100$ ) compared to ab initio molecular dynamics, the SCAILD method might even have opened the door to the theoretical study of the high temperature phases of the lanthanides and actinides.

# Acknowledgments

First of all I would like to thank all of the people in the condensed matter group who have made every day's work an exclusively joyful experience, and I dare say there were lots of them. And when mentioning the great atmosphere I must also thank the founder of our group Professor Börje Johansson not only for starting the group, but also for inspiring me to begin my Phd here. I am also grateful for the guidance of my supervisor, Professor Olle Eriksson, especially for his patience and endless optimism. Not forgetting to pay tribute to Mikhail Katsnelson for being so generous with his extensive knowledge in physics. Furthermore, I must also thank Sven Rudin for the inspiring time in Los Alamos, and for scaring the living day lights out of me during our trip to Cabezon peak. Thank you Anna, not only for your guidance when we worked on the gold paper, but also for all the nice food I have had the pleasure to enjoy at your place. Thank you *Syrran* and *Morsan* for all your support. Thank you Micke and Martin for your never failing good spirits and thank you Biplab for your most extensive and passionate exposé of Indian cricket. I also want to thank Velimir for never getting tired of helping me tame misbehaving computers, and for supplying me with an almost endless arsenal of burlesque stories. And who can ever forget Love's unparalleled ability to come up with "good bad jokes". Thank you Oscar for all the good times we had discussing physics and for all the other times as well. Furthermore I would like to thank Alexei for helping me with all the BCOOP related issues and for all the nice times we had at the various pubs of Uppsala. I must also thank Weine for sharing the vice of having a black sense of humor, and for making me think I little bit further than the tip of my nose. And speaking about the art of black humor, I must not forget to thank the masters of all masters, Fredrik and Francesco. Fredrik for his musical generosity and his speech on the subject: "Why the people of Gräsö are considered to be a bit mad", and Francesco for all his stories from Italy. I must also pay tribute to Torbjörn the living jukebox Björkman for raising the standard of the *förnedrings orkestern*, and for his performance of the song *stor svensken* at Gotlands nation (who could ever forget that?). Furthermore, thank you Johan for being Johan, and Diana and Pooja for disturbing me whenever I was working too hard. And of course, I am endlessly thankful to Thomas who like Jesus, who brought Lazarus back from the dead, did the same thing with our computer system. Finally, last but not least, I must also thank my former room-mates Andreas and Carlos, Andreas for his advice in

the art of remaining sane and Carlos for his endless efforts in trying to confuse me.

## A. Fermi surfaces of hcp Zr

In figure A.1 the calculated Fermi surfaces for hcp Zr are displayed for three different compressions of the c-axis.

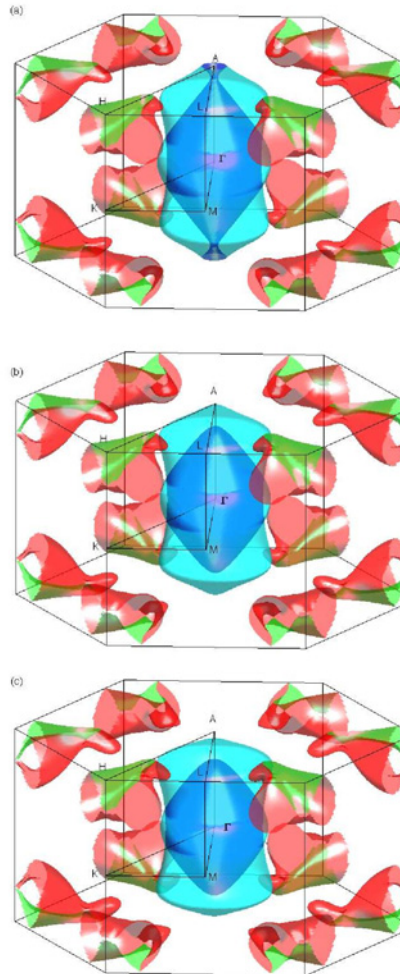


*Figure A.1:* Calculated Fermi surfaces of hcp Zr at T=0 equilibrium volume for three different lattice constants  $c$ , at  $c = 0.988c_0$  (a), at  $c = c_0$  (b) and at  $c = 1.012c_0$  (c). Here  $c_0$  corresponds to the (T=0) equilibrium lattice constant.



## B. The mean field Hamiltonian

This appendix shows how the mean field Hamiltonian (8.75) with eigenvalues given by (8.76) is chosen. The construction of this Hamiltonian is based on the SCAILD method for calculating the mean field eigenvalues  $\bar{\omega}_{\mathbf{k}s}$  from the fourier transform of the forces. Using the sum convention for the coordinate indexes the forces can be expressed as

$$F_{\mathbf{R}j} = - \sum_{\mathbf{R}'} \bar{\Phi}_{j\alpha}(\mathbf{R} - \mathbf{R}') U_{\mathbf{R}'\alpha} - \frac{1}{2} \sum_{\mathbf{R}', \mathbf{R}''} \Phi_{j\alpha\beta}(\mathbf{R}, \mathbf{R}', \mathbf{R}'') U_{\mathbf{R}'\alpha} U_{\mathbf{R}''\beta} + \dots \quad (\text{B.1})$$

Fourier transforming the above expression and substituting the displacements  $\mathbf{U}_{\mathbf{R}}$  with (8.3) gives

$$F_{\mathbf{k}j} = - \sum_s \sqrt{M} \omega_{\mathbf{k}s}^2 \varepsilon_{\mathbf{k}s j} \mathcal{Q}_{\mathbf{k}s} - \frac{1}{2MN^{3/2}} \sum_{\mathbf{k}_1, \mathbf{k}_2} \sum_{s_1, s_2} \Phi_{j\alpha\beta}(\mathbf{k}, \mathbf{k}_1, \mathbf{k}_2) \varepsilon_{\mathbf{k}_1 s_1 \alpha} \varepsilon_{\mathbf{k}_2 s_2 \beta} \mathcal{Q}_{\mathbf{k}_1 s_1} \mathcal{Q}_{\mathbf{k}_2 s_2} + \dots \quad (\text{B.2})$$

Finally multiplying (B.2) with  $-\varepsilon_{\mathbf{k}s j} / (\mathcal{Q}_{\mathbf{k}s} \sqrt{M})$  and summing over  $j$  gives

$$- \frac{\mathbf{F}_{\mathbf{k}} \varepsilon_{\mathbf{k}s}}{\sqrt{M} \mathcal{Q}_{\mathbf{k}s}} = \omega_{\mathbf{k}s}^2 \left( 1 + \frac{1}{2} \sum_{\mathbf{k}_1, \mathbf{k}_2} \sum_{s_1, s_2} \mathcal{A}(\mathbf{k}, \mathbf{k}_1, \mathbf{k}_2, s, s_1, s_2) \frac{\mathcal{Q}_{\mathbf{k}_1 s_1} \mathcal{Q}_{\mathbf{k}_2 s_2}}{\mathcal{Q}_{\mathbf{k}s} \omega_{\mathbf{k}s}^2} + \dots \right). \quad (\text{B.3})$$

where  $\mathcal{A}(\mathbf{k}, \mathbf{k}_1, \mathbf{k}_2, s, s_1, s_2)$  is given by (8.73). Now it becomes obvious that the right hand side of (B.3) is equivalent to the right hand side of (8.76).

From the above discussion it has been seen that by defining a mean field Hamiltonian through (8.75) and (8.76), the eigenvalues of the Hamiltonian can always be accessed by means of a fourier transform of the inter atomic forces.



## C. Embedded atom potentials

This appendix contains the explicit analytic forms of the embedded atom potentials used in chapter 7, together with the parameters for Ti, Zr and Hf. For Ti and Hf the Finnis-Sinclair [83] EAP was used, where the contribution to the total energy from an atom indexed  $i$  is given by

$$E_i = \frac{1}{2} \sum_{j(\neq i)} V(R_{ij}) + F(\rho_i). \quad (\text{C.1})$$

Here the index  $j$  is that of an atom at distance  $R_{ij}$  from the atom  $i$ . Furthermore the pair potential part is given by

$$V(r) = \sum_{k=1}^7 A_k (R_k - r)^3 \Theta(R_k - r), \quad (\text{C.2})$$

where  $\Theta(x > 0) = 1$ ,  $\Theta(x < 0) = 0$ . The density is given by

$$\rho_i = \sum_{j(\neq i)} \frac{R_{ij}}{a} e^{-\frac{5R_{ij}}{a}}, \quad (\text{C.3})$$

and the embedding function correct to second order in  $\rho$  is given by

$$F(\rho) = F_0 + \frac{F_0''}{2} \rho^2 \quad (\text{C.4})$$

In the table C.1 the EAP parameters for Ti, Hf and Zr are tabulated.

The energy contribution from an atom  $i$  to the total energy for the EAP used for Zr [84] is given by (C.1), with the pair potential part given by (C.2). However the density for this potential is instead expressed as

$$\rho_i = \sum_j \phi_0 f(R_{ij}), \quad (\text{C.5})$$

where

$$f(r) = \begin{cases} \frac{e^{-5r}}{r}, & r \leq R_m \\ (r - R_c)^3 (a_1 r^2 + a_2 r + a_3), & R_m < r \leq R_c \\ 0, & R_c \leq r \end{cases} \quad (\text{C.6})$$

Furthermore the embedding function for the EAP of Zr is expressed as a 8:th order polynomial

$$F(\rho) = \sum_{k=0}^8 B_k \rho^k. \quad (\text{C.7})$$

In the tables C.1 ,C.2 and C.3 the EAP parameters for Zr are tabulated.

	<i>Ti</i>	<i>Hf</i>	<i>Zr</i>
$R_1$	2.1	2.1	1.0
$R_2$	1.8	1.8	1.05
$R_3$	1.7	1.7	1.55
$R_4$	1.65	1.65	1.60
$R_5$	1.4	1.4	1.65
$R_6$	1.05	1.02	1.70
$R_7$	1.0	1.0	1.75
$A_1$	0.42626708	0.54096253	-38.4084159
$A_2$	-2.46091326	-4.9347962	36.9240324
$A_3$	-7.16830310	-9.7598544	-6.0670690
$A_4$	10.6311786	18.3443963	8.4563250
$A_5$	-0.8071241	-3.728852	-4.6893208
$A_6$	50.2494690	197.9058192	7.9667179
$A_7$	-42.2605816	-199.888792	-5.644938
$F_0$	-3.316	-4.296	...
$F_0''$	52.286	20.430	...
$a$	2.951	3.194	3.232

Table C.1: EAP parameters taken from Ref. [83, 84]. The expansion coefficients  $A_k$ ,  $F_0$  and  $F_0''$  are given in units of eV. The parameters  $R_k$  are in units of the parameter  $a$ , and the parameter  $a$  is given in units of Å.

	$a_1$	$a_2$	$a_3$	$R_m$	$R_c$	$\phi_0$
$\rho$	-0.44417136	1.07926027	-0.67936231	1.3	1.65	11.28516908

Table C.2: EAP density parameters taken from Ref. [84]. The expansion coefficients  $a_k$ ,  $R_m$  and  $R_c$  are given in units of the parameter  $a$ . The parameter  $\phi_0$  is dimensionless.

	$F(\rho)$
$B_0$	-1.1363
$B_1$	-14.902
$B_2$	28.506
$B_3$	-30.806
$B_4$	20.216
$B_5$	-8.054100
$B_6$	1.9047000
$B_7$	-0.24573000
$B_8$	0.01331200

Table C.3: EAP embedding function parameters obtained from a fit of a plot of  $F(\rho)$  presented in Ref. [84]. The expansion coefficients  $B_k$  are given in units of eV.



# Bibliography

- [1] Nagamatsu, N. Nakagawa, T. Muranaka, and Y. Zenitani, *Nature* **410**, 63 (2001).
- [2] J. Osorio-Guillén, S. Simak, Y. Wang, B. Johansson, and R. Ahuja, *Solid State Commun* **123**, 257 (2002).
- [3] J. D. Jorgensen, D. G. Hinks, and S. Short, *Phys. Rev. B* **63**, 224522 (2001).
- [4] A. F. Goncharov, V. V. Struzhikin, E. Gregoryanz, J. Hu, R. J. Hemley, H.-K. Mao, G. Lapertot, S. L. Bud'ko, and P. C. Canfield, *Phys. Rev. B* **64**, 100509 (2001).
- [5] T. Saito, T. Furutta, J.-H. Hwang, S. Kuramoto, K. Nishino, N. Suzuki, R. Chen, A. Yamada, K. Ito, Y. Seno, *et al.*, *Science* **300**, 464 (2003).
- [6] C. Zener, *Phase stability in metals and alloys* (McGraw-Hill (New York), 1967), edited by P. S. Rudman, J. Stringer, and R. I. Jaffee.
- [7] R. G. Parr and W. Yang, *Density functional theory of atoms and molecules* (Oxford, 1989), 2nd ed.
- [8] R. M. Martin, *Electronic structure basic theory and practical methods* (Cambridge, 2004), 1st ed.
- [9] P. Hohenberg and W. Kohn, *Phys. Rev.* **136**, B864 (1964).
- [10] W. Kohn and L. J. Sham, *Phys. Rev.* **140**, B1133 (1965).
- [11] R. Weinstock, *Calculus of variations* (Dover, 1974).
- [12] M. Thijssen, *Computational physics* (Cambridge, 1999).
- [13] Aschcroft and Mermin, *Solid state physics* (Thomson Learning Inc., 1976).
- [14] H. L. Skriver, *The LMTO Method* (Springer, 1984).
- [15] J. M. Wills, O. Eriksson, and M. Alouani, *Full-potential LMTO total energy and force calculations in: Dreyse (Ed.), Electronic Structure and Physical Properties of Solids: The uses of the LMTO Method* (Springer, Berlin, 2000).
- [16] J. Trygg, *First principles studies of magnetic and structural properties of metallic systems* (Uppsala University, 1995), phd Thesis.

- [17] K. Andersen and O. Jepsen, *Physica* **91**, 317 (1977).
- [18] J. Singh, *Physics of semiconductors and their heterostructures* (McGraw-Hill, 1993).
- [19] M. C. Payne, M. P. Teter, D. C. Allan, T. A. Arias, and J. D. Joannopoulos., *Rev. Mod. Phys.* **64**, 1045 (1992).
- [20] D. Vanderbilt, *Phys. Rev. B* **41**, 7892 (1990).
- [21] P. E. Blöchl, *Phys. Rev. B* **50**, 17953 (1994).
- [22] A. Grechnev, R. Ahuja, and O. Eriksson, *J.Phys.:Condens.Matter* **15**, 7751 (2003).
- [23] A. Grechnev, *Hydrogen-hydrogen interaction and chemical bonding in solids* (Uppsala University, 2003), licentiate Thesis.
- [24] A. E. H. Love, *A treatise on the mathematical theory of elasticity* (Dover, 1944), p. 159.
- [25] P.Ravindran, P. Vajeeston, R. Vidya, A. Kjekshus, and H. F. g, *Phys. Rev. B* **64**, 07510 (2001).
- [26] S. F. Pugh, *Philos. Mag.* **45**, 833 (1954).
- [27] Cyrot-Lackmann, *Advances in Physics* **16**, 393 (1967).
- [28] Cyrot-Lackmann, *J. Phys. Chem. Solids* **29**, 1239 (1968).
- [29] D. Pettifor, *Bonding and structure of molecules and solids* (Oxford, 2002), p. 223.
- [30] H. L. Skriver, *Phys. Rev. B* **31**, 1909 (1985).
- [31] J. A. Moriarty, *Phys. Rev.* **B38**, 3199 (1988).
- [32] W. A. Harrison, *Electronic Structure and the properties of solids* (Dover, 1980).
- [33] O. K. Andersen and O. Jepsen, *Phys. Rev. Lett.* **48**, 809 (1982).
- [34] O. K. Andersen, *Phys. Rev.* **B12**, 3060 (1975).
- [35] A. R. Mackintosh and O. K. Andersen, *Electrons at the Fermi surface* (Cambridge, 1980), edited by M. Springford, Cambridge University press.
- [36] S. Iijima, *Nature* **354**, 56 (1991).
- [37] H.W.Hugosson, U.Jansson, B.Johansson, and O.Eriksson, *Science* **293**, 2434 (2001).

- [38] W. M. C. Yang, T. Tsakalakos, and J. E. Hilliard, *J. Appl. Phys.* **48**, 876 (1977).
- [39] L. S. Dubrovinsky, N. A. Dubrovinskaia, V. Swamy, J. Muscat, N. M. Harrison, R. Ahuja, B. Holm, and B. Johansson, *Nature* **410**, 653 (2001).
- [40] N. V. Skorodumova, S. I. Simak, B. I. Lundqvist, I. A. Abrikosov, and B. Johansson, *Phys. Rev. Lett.* **89**, 166601 (2002).
- [41] Y. Liu and M. L. Cohen, *Science* **245**, 84 (1989).
- [42] R. M. Dreizler and E. K. U. Gross, *Density Functional Theory, An Approach to the Quantum Many-Body Problem* (Springer-Verlag, 1990).
- [43] P. L. Taylor and O. Heinonen., *Condensed Matter Physics* (Cambridge University Press, 2002).
- [44] J. Lynn, H. Smith, and R. Nicklow, *Phys. Rev. B* **8**, 3493 (1973).
- [45] G. Kresse and D. Joubert, *Phys. Rev. B* **59**, 1758 (1999).
- [46] D. Alfé, *The Phon-software can together with a description of the program can be found at: <http://chianti.geol.ucl.ac.uk/dario/>.*
- [47] Y. Akahama, H. Kawamura, and A. K. Singh, *J. Appl. Phys.* **92**, 5892 (2002).
- [48] W. Holzappel, *J. Appl. Phys.* **93**, 1813 (2003).
- [49] K. Kunc, I. Loa, and K. Syassen, *Phys. Rev. B* **68**, 094107 (2003).
- [50] A. Dewaele, P. Loubeyre, and M. Mezouar, *Phys. Rev. B* **69**, 092106 (2004).
- [51] A. Dewaele, P. Loubeyre, and M. Mezouar, *Phys. Rev. B* **70**, 094112 (1999).
- [52] A. Sommerfeld and N. H. Frank, *Rev. Mod. Phys.* **3**, 1 (1931).
- [53] P. Bell, J. Xu, and H. Mao, *Shock Waves in Condensed Matter* (Plenum New, York, 1986), y.m. gupta ed.
- [54] D. L. Heinz and R. Jeanloz, *J. Appl. Phys.* **55**, 885 (1984).
- [55] C. W. Greeff and M. J. Graf, *Phys. Rev. B* **69**, 054107 (2004).
- [56] H.-K. Mao, J. Xu, and P. Bell, *J. Geophys. Res.* **91**, 4673 (1986).
- [57] J. C. Boettger, *Phys. Rev. B* **67**, 174107 (2003).
- [58] *LASL Shock Hugoniot Data* (Berkeley, 1980), s.p. marsh ed.
- [59] L. Al'tshuler, A. Bakanova, I. Dudoladov, E. Dynin, R. Trunin, and B. Chekin, *J. Appl. Mech. Tech. Phys.* **22**, 145 (1981).
- [60] A. Jones, W. Isbell, and C. Maiden, *J. Appl. Phys.* **37**, 3493 (1966).

- [61] M. van Thiel, A. Kusbov, and A. Mitchell (Lawrence Radiation Laboratory, Livermore, CA, 1967), technical Report UCRL-50108, 1967 (unpublished).
- [62] P. Vinet, J. R. Smith, J. Ferrante, and J. H. Rose, *Phys. Rev. B* **35**, 1945 (1987).
- [63] R. K. Kirby, T. A. Hahn, and B. D. Rothrock, *American Institute of Physics Handbook* (McGraw-Hill, New York, 1957), sec. 4f.
- [64] A. Eichler, K.-P. Bohnen, W. Reichardt, and J. Hafner, *Phys. Rev. B* **57**, 324 (1998).
- [65] B. L. Fielek, *J. Phys. F: Metal Phys* **10**, 2381 (1980).
- [66] G. Nilsson and S. Rolandson, *Phys. Rev. B* **7**, 2393 (1973).
- [67] W. A.D.B. and C. S.H., *Solid State Commun.* **2**, 233 (1964).
- [68] Y. Nakagawa and A. D. B. Woods, *Phys. Rev. Lett.* **11**, 271 (1963).
- [69] R. W. Meyerhoff and F. Smith, *J. Appl. Phys.* **33**, 219 (1962).
- [70] J. Goldak, L. T. Lloyd, and C. S. Barrett, *Phys. Rev.* **144**, 478 (1966).
- [71] Y. S. Touloukian, R. K. Kirby, R. E. Taylor, and P. D. Desai, *Thermal expansion, Metallic Elements and Alloys* (Plenum, New York, 1975).
- [72] S. K. Sinha, T. O. Brun, L. D. Muhlestrin, and J. Sakurai, *Phys. Rev. B* **1**, 2430 (1970).
- [73] C. Stassis, J. Zarestky, D. Arch, O. D. McMasters, and B. N. Harmon, *Phys. Rev. B* **18**, 2632 (1978).
- [74] N. Wakabayashi, R. H. Scherm, and H. G. Smith, *Phys. Rev. B* **25**, 5122 (1981).
- [75] R. Heid, L. Pintschovius, W. Reichardt, and K.-P. Bohnen, *Phys. Rev. B* **61**, 12059 (1999).
- [76] M. I. Katsnelson, I. I. Naumov, and A. V. Trefilov, *Phase transitions* **49**, 143 (1994).
- [77] V. I. Nizhankovskii, M. I. Katsnelson, G. V. Peschanskikh, and A. V. Trefilov, *Pis'ma ZhETF* **59**, 693 (1994).
- [78] P. Mal'ko, D. Arensburger, V. Pugin, V. Nemchenko, and S. L'Vov, *Powder Metallurgy and Metal Ceramics* **9**, 642 (1970).
- [79] R. Pawar and V. Deshpande, *Acta Cryst.* **A24**, 316 (1968).
- [80] A. Heimig, W. Petry, J. Tramenau, M. Alba, C. Herzig, H. R. Schober, and G. Vogl., *Phys. Rev. B* **43**, 10948 (1991).

- [81] W. Petry, A. Heiming, J. Tramenau, M. Alba, C. Herzig, H. R. Schober, and G. Vogl., Phys. Rev. B **43**, 10933 (1991).
- [82] J. Tramenau, A. Heiming, W. Petry, M. Alba, C. Herzig, W. Miekeley, and H. R. Schober, Phys. Rev. B **43**, 10963 (1991).
- [83] R. Pasianot and E. J. Savino, Phys. Rev. B **45**, 12704 (1992).
- [84] R. Pasianot and A. Monti, J. Nucl. Mat. **264**, 198 (1999).
- [85] C. Stassis, D. Arch, B. N. Harmon, and N. Wakabayashi, Phys. Rev. B **19**, 181 (1979).
- [86] C. Stassis, D. Arch, O. D. McMasters, and B. N. Harmon, Phys. Rev. B **24**, 730 (1981).
- [87] S. L. Bud'ko, G. Lapertot, C. Petrovic, C. E. Cunningham, N. Andersson, and P. C. Canfield, Phys. Rev. Lett. **86**, 1877 (2001).
- [88] E. J. Choi, D. Roundy, H. Sun, M. L. Cohen, and S. G. Loule, Phys. Rev. B **66**, 020513 (2002).
- [89] M. Monteverde, M. Nunez-Rgueiro, K. A. Regan, M. A. Hayward, T. He, S. M. Loureiro, and R. J. Cava, Science **292**, 75 (2001).
- [90] J. Y. Xiang, D. N. Zheng, J. Q. Li, S. L. Li, H. H. Wen, and Z. X. Zhao, Physica C-Superconductivity And its Applications **386**, 611 (2003).

# Acta Universitatis Upsaliensis

*Digital Comprehensive Summaries of Uppsala Dissertations  
from the Faculty of Science and Technology 338*

Editor: The Dean of the Faculty of Science and Technology

A doctoral dissertation from the Faculty of Science and Technology, Uppsala University, is usually a summary of a number of papers. A few copies of the complete dissertation are kept at major Swedish research libraries, while the summary alone is distributed internationally through the series Digital Comprehensive Summaries of Uppsala Dissertations from the Faculty of Science and Technology. (Prior to January, 2005, the series was published under the title “Comprehensive Summaries of Uppsala Dissertations from the Faculty of Science and Technology”.)

Distribution: [publications.uu.se](http://publications.uu.se)  
urn:nbn:se:uu:diva-8198



ACTA  
UNIVERSITATIS  
UPSALIENSIS  
UPPSALA  
2007